Politecnico di Torino

Politecnico di Torino

Department of Electronics and Telecommunications

Master's Degree Course in Mechatronic Engineering

Satellite Miniaturisation beyond PocketQube: Design and Integration of LEAn Femto (LEAF) Sat Prototype

Supervisors:
Prof. Marcello Romano
Prof.ssa Chantal Cappelletti

Candidate:
Luca Bigelli

Academic Year 2022-2023

It was kind of funny. I didn't think that people would criticise it as much as they did, but we got a lot of feedback, you know, "That's the dumbest idea I've ever heard. Nobody's going to use this toy." We said, "Who the heck cares. We'll go ahead and use it. We're using it for education."

Bob Twiggs, March 8, 2014, talking about CubeSats.

Summary

My name is Luca Bigelli, and under the supervision of Professor Marcello Romano, I conducted a thesis titled "Satellite Miniaturisation beyond PocketQube: Design and Integration of LEAn Femto (LEAF) Sat Prototype". The title accurately reflects the structure and content of this master's thesis.

The initial part of the thesis consists of a comprehensive survey of technologies that enable satellite miniaturisation. As the title suggests, the objective was to push beyond the boundaries of PocketQube satellites and explore the development of miniaturised satellites in the femto-class, weighing less than 100 grams.

This research aligns with the ongoing pursuit of satellite miniaturisation, which has been a thriving field of study in recent decades.

The study investigates the motivations behind adopting the miniaturised satellite approach, primarily driven by significant technological advancements and the global demand for smaller electrical components. These advancements have led to refined fabrication processes that enable the production of extremely compact electrical components. Additionally, satellite miniaturisation contributes to democratising space access by providing opportunities for smaller organisations, including universities.

Furthermore, the use of very small satellites enables Distributed Spacecraft Missions (DSMs) with diverse objectives, characterised by their inherent reliance on multiple spacecraft. The thesis explores various DSM characteristics and their potential applications.

Having established the context of satellite miniaturisation, the thesis examines past femtoSatellite prototypes to understand their distinct features, development challenges, and different design approaches employed by various designers.

The focus then shifts to the main satellite subsystems, exploring technologies that facilitate the miniaturisation of traditional components within each subsystem. The investigation encompasses existing market solutions as well as novel approaches documented in literature.

This groundwork laid the foundation for the second part of the thesis, conducted under the guidance of Professor Chantal Cappelletti at the University of Nottingham.

In this phase, the author designed, integrated, and tested a new femtoSatellite prototype named LEAF femtoSat, derived from the attributes of LEAn and Femto.

Given the central objective of miniaturising satellites to the femto-class, the author aimed to design a femtoSat prototype that demonstrates the feasibility of such small satellites, thus justifying the *"femto"* attribute.

The prototype is also referred to as *lean* due to its rapid design and integration process, completed within a few weeks. Additionally, the LEAF prototype was constructed solely using Commercial Off-the-Shelf (COTS) Components, reducing costs and facilitating fast prototyping. The *"lean"* attribute encapsulates the philosophy behind satellites developed within short timeframes, relying on readily available COTS components.

While the integrated LEAF prototype is fully functional, there is ample room for future improvements and enhancements.

Furthermore, a comprehensive testing phase of the COTS components is necessary to ensure their suitability for the demanding space environment.

However, femtoSatellites are designed as disposable spacecraft intended for deployment in Very Low Earth Orbits (VLEO), where space environmental conditions are more favourable.

Deploying very small satellites in VLEO mitigates concerns related to very small satellite deployment, as demonstrated by Zachary Manchester's Sprite Prototypes. These very small satellites are likely to harmlessly re-enter and burn up in the atmosphere within weeks or months, thus addressing space debris concerns. Consequently, missions employing such small spacecraft have limited durations, increasing the likelihood of survival of femtoSatellites within this timeframe.

Abstract

This master's thesis explores innovative solutions for satellite subsystems miniaturisation, with a specific focus on technologies that could enable the design and development of femtoSatellites, which are small satellites weighing less than 100 grams.

After a concise review of the main spacecraft subsystems, the possibility to miniaturise existing devices will be investigated and innovative solutions will be explored. The challenges associated with satellite miniaturisation will be examined, along with the advantages that have contributed to the growing popularity of small satellites.

Additionally, the thesis will outline the design and integration of the LEAn Femto (LEAF) Sat, a femtoSat prototype entirely constructed with Commercial Off-The-Shelf (COTS) components. The LEAF Sat prototype aims at demonstrating the feasibility of miniaturisation up to femto-class and the ability to develop a small satellite quickly and cost-effectively, which is why it is referred to as *lean*.

Contents

List of Figures

Chapter 1

Introduction

The objective of this master's thesis is to explore innovative solutions for miniaturising satellite subsystems, with a specific focus on those technologies that could enable the development of femtoSatellites, i.e. satellites weighing less than 100 grams.

Chapter 1 continues with the motives that brought the attention of the space community towards small satellites, accompanied by a brief historical context. CubeSat and PocketQube standards will also be briefly introduced as femtoSatellites aim at going beyond the dimensions defined by those standards. The Chapter then outlines the newer approach to space that such small satellites characterise and which missions can be accomplished with femtoSats.

Chapter 2 provides a comprehensive literature review, highlighting various femtoSat prototypes that have been developed and, in some cases, launched in the past.

Chapter 3 offers a concise introduction to the main satellite subsystems and investigates the possibility to miniaturise existing devices. Innovative solutions will be explored as well, in both literature and the market.

Chapter 4 outlines the design, development of the LEAn Femto (LEAF) Sat Prototype, a new femtoSat prototype entirely constructed with Commercial Off-the-Shelf (COTS) components at the University of Nottingham. The LEAF Sat prototype aims at demonstrating the feasibility of miniaturisation up to femto-class and the ability to develop a small satellite quickly and cost-effectively, which is why it is referred to as *lean*.

Chapter 5 concludes the thesis by presenting future possibilities and perspectives, also briefly addressing the issue of *space debris*.

1.1 History of Satellite Miniaturisation

In the past three decades we have witnessed a remarkable technological progress. Refined production technologies and huge investments in research and development were such that highly integrated electrical components as well as powerful and efficient integrated circuits are nowadays available at affordable prices. The global demand of these micro-electrical components has further contributed to economies of scale, resulting in even lower costs. We are talking about Commercial Off-the-Shelf (COTS) components, extremely miniaturised components that can be easily and cheaply found *off-the-shelf*.

Miniaturisation has become a defining characteristic of devices in our everyday lives, ranging from smartphones and Smart TVs to cars. It is intriguing to note that this technological progress has also influenced the space economy. In the late 1990s, space professionals began contemplating the possibility of miniaturising satellite subsystems, leading to the emergence of smaller satellites. Today, small satellites have become a reality in the space industry, leveraging the advancements in micro-electronics and offering new possibilities for space utilisation and exploration.

1.1.1 Satellites Classifications

At this point it is important to explain what is intended with *small satellite*. A first attempt [1] [2] to provide a proper classification of satellites based on their mass, was made by Martin Sweeting in 1991 [3], as shown in Table 1.1.

Satellite Class	Mass [kg]
Large	>1000
Small	500 - 1000
Mini	100 - 500
Micro	10 - 100
Nano	1 - 10

Table 1.1: Satellite Mass Classification by Martin Sweeting (1991) [3].

Sweeting's classification was later refined by Konecny in 2004 [4]. He replaced "small" with "medium" class and added two new categories:
"pico-" for satellites weighing between 0.1 and 1 kg, and "femto-" for satellites weighing less than 0.1 kg (Table 1.2).

Satellite Class	Mass [kg]
Large	>1000
Medium	500 - 1000
Mini	100 - 500
Micro	10 - 100
Nano	1 - 10
Pico	0.1 - 1
Femto	< 0.1

Table 1.2: Satellite Mass Classification by Gottfried Konecny (2004) [4].

The Federal Aviation Administration (FAA) also provides a more detailed classification [5][6], particularly for heavier spacecraft, with slight modifications to the mass ranges too (Table 1.3). According to [6], "smallsats" and "very small satellites" typically refer to satellites below 600 kg.

Satellite Class	Mass [kg]
Extra Heavy	>7000
Heavy	5400 - 7000
Large	4200 - 5400
Intermediate	2500 - 4200
Medium	1200 - 2500
Small	600 - 1200
Mini	200 - 600
Micro	10 - 200
Nano	1 - 10
Pico	0.1 - 1
Femto	0.01 - 0.1

Table 1.3: Satellite Mass Classification adopted by Federal Aviation Administration (FAA) [5].

It is noteworthy that literature provides further classifications based on mass or other relevant spacecraft parameters. A comprehensive review conducted by Botelho A. S. and Xavier Jr. (2019) [2] can serve as a valuable

reference for exploring other classifications. Nevertheless, mass classification proves to be the most widely adopted and practical approach, as mass directly influences launch costs.

1.1.2 CubeSat and PocketQube Standards

Delving into the classification it is worth to introduce the CubeSat and the PocketQube Standards.

CubeSat Standard

The CubeSat Project (Figure 1.1) originated in 1999 as a collaboration between Professor Jordi Puig-Suari from California Polytechnic State University (Cal Poly) and Professor Bob Twiggs from Stanford University's Space Systems Development Laboratory (SSDL) [7].

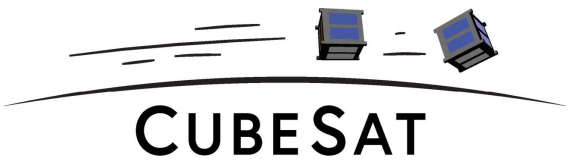

Figure 1.1: CubeSat Project Logo.

It is worth to highlight the intentions of the project founders. Rather than simply introducing a new satellite model, their aim was to find a revolutionary satellite design that would have provided students with a practical opportunity to develop satellites during their university studies [8]. Professor Twiggs' words clearly makes the concept:

> It all started as a university education program satellite. It was kind of funny. I didn't think that people would criticise it as much as they did, but we got a lot of feedback, you know, "That's the dumbest idea I've ever heard. Nobody's going to use this toy." We said, "Who the heck cares. We'll go ahead and use it. We're using it for education."
>
> *"A chat with Bob Twiggs, father of the CubeSat"*
> by Stephen Clark, March 8, 2014.

The new form factor was intended to reduce costs and development time, making space exploration accessible to small companies and universities as well. Despite initial skepticism from space professionals who viewed the small

form factor as nothing more than a toy in space, CubeSat proved to be a game-changer for space accessibility. CubeSats expanded space missions beyond the realm of military and government organisations, providing broader and easier access to space for universities and educational institutions as well as smaller companies, a possibility once deemed impossible.

Motivated by this vision, Twiggs and Puig-Suari established the CubeSat Standard specifications. The CubeSat was defined as a new class of satellites with a *standardised* size and form factor, defined as "U". A 1U CubeSat is, as the name suggests, a cube with 10 cm side that has a maximum mass of 2 kg. Multiples and fractions of the "U" unitary cube are also possible, up to 12U and further (Figure 1.2).

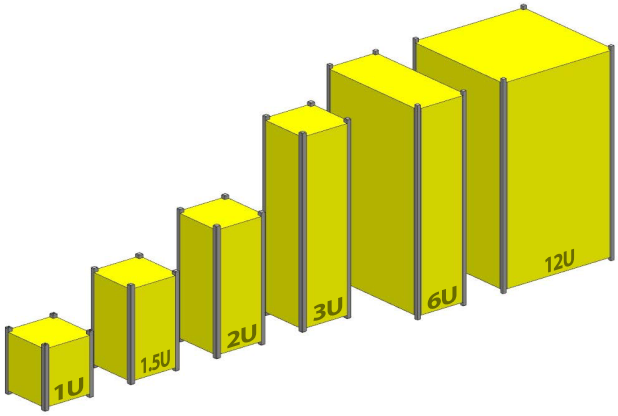

Figure 1.2: CubeSat Family [7].

The primary objective of the standard is to outline the specifications to design a CubeSat, as depicted in Figure 1.3 for the 1U CubeSat.

Figure 1.4 shows an extra volume that can be included in 3U, 6U, and 12U CubeSats, typically named Tuna Can for its shape. This extra volume is often used to integrate a propulsion system.

Additionally, the standard aims at providing information on CubeSat launchers (Figure 1.5) and their interfaces.

A significant demonstration of the possibilities that the CubeSat standard was introducing in the future of space missions eventually arrived in 2003: the Poly PicoSatellite Orbital Deployer, or P-POD (Figure 1.5), was developed by Puig-Suari and CalPoly and, in June 2023, the first six CubeSats, launched as secondary payloads, were deployed into orbit [9].

Since then, over 2000 CubeSats have been launched into space by various countries [10]. This remarkable success of CubeSats led to the spread of

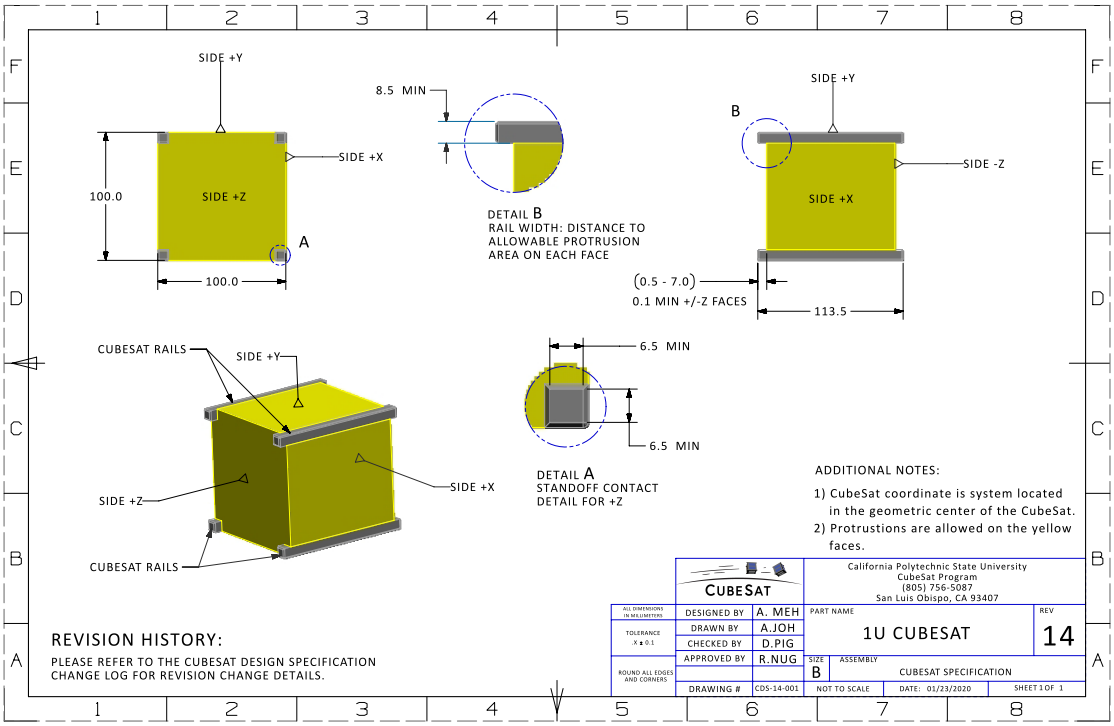

Figure 1.3: 1U CubeSat Specification Sheet [7].

Commercial Off-the-Shelf (COTS) components and parts for CubeSats, as well as conventional launch resources.

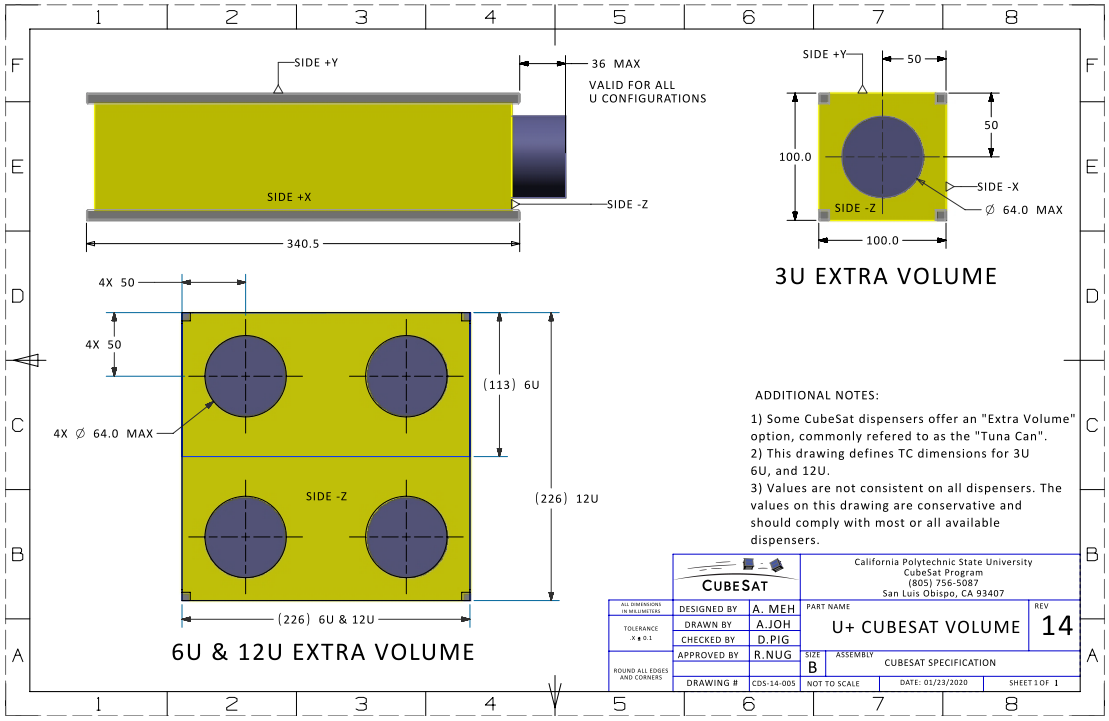

Figure 1.4: U+ CubeSat Volume Specifications for 3U, 6U and 12U [7].

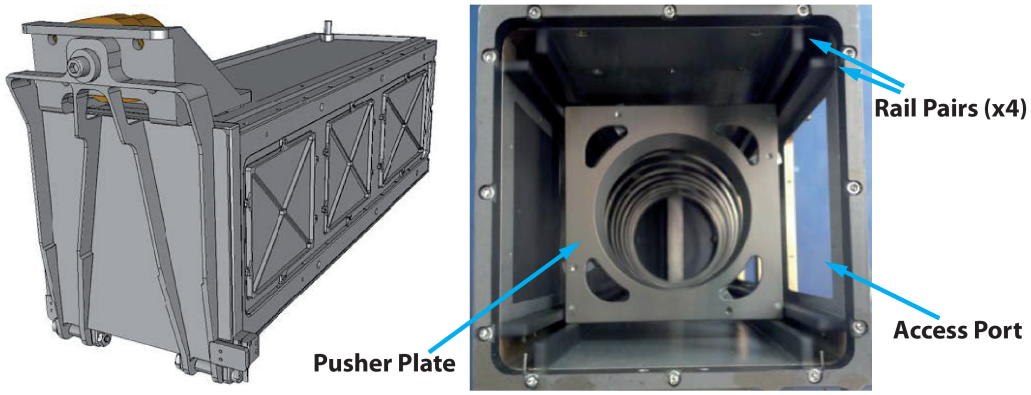

Figure 1.5: Poly Picosatellite Orbital Deployer (P-POD) [7].

PocketQube Standard

Electrical components have continued to evolve, becoming smaller, more efficient, and more powerful. Space researchers were able to miniaturise satellite subsystems and fit them inside the confines of a CubeSat form factor.

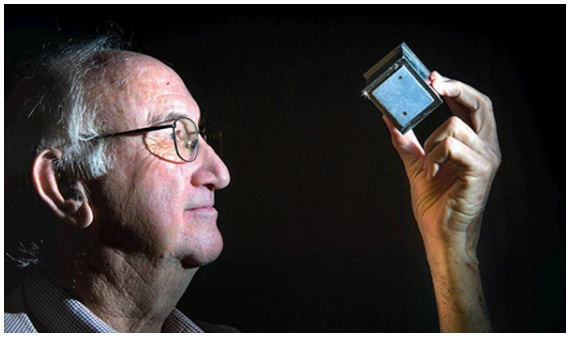

Figure 1.6: Bob Twiggs with a PocketQube.

Despite this progress, the weight of a CubeSat remained high, resulting in launch costs that were still unaffordable for the majority of small organisations. Eager to make space accessible to everyone, professor Bob Twiggs pushed the frontiers of small satellites beyond the CubeSat: in 2009 he proposed the PocketQube, the *peoples satellite, that could fit in your pocket*, an even smaller form factor was just born.

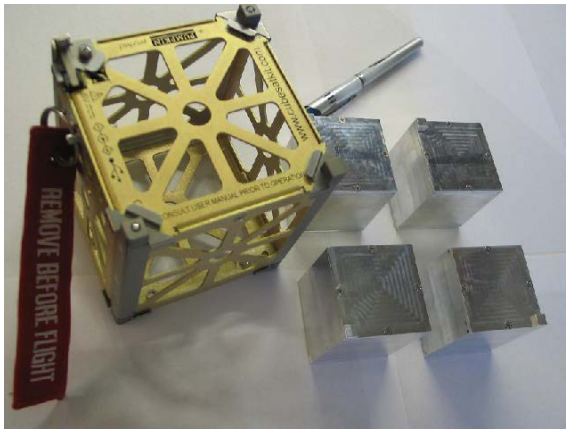

Figure 1.7: A CubeSat and some PocketQubes.

Subsequently, Morehead State University (MSU) and Kentucky Space defined the PocketQube specifications (Figure 1.8). The fundamental PocketQube unit, referred to as a "P", was still cubic-shaped with a side length

of 50 mm and a mass not exceeding 250 grams, classifying it as a pico-satellite. To simplify the design and integration process while making it more cost-effective, PocketQubes typically employ Commercial Off-the-Shelf (COTS) components. Differently from CubeSats, which are deployed along their long-side edges, the PocketQubes utilise a sliding backplate mechanism for ejection (Figure 1.9).

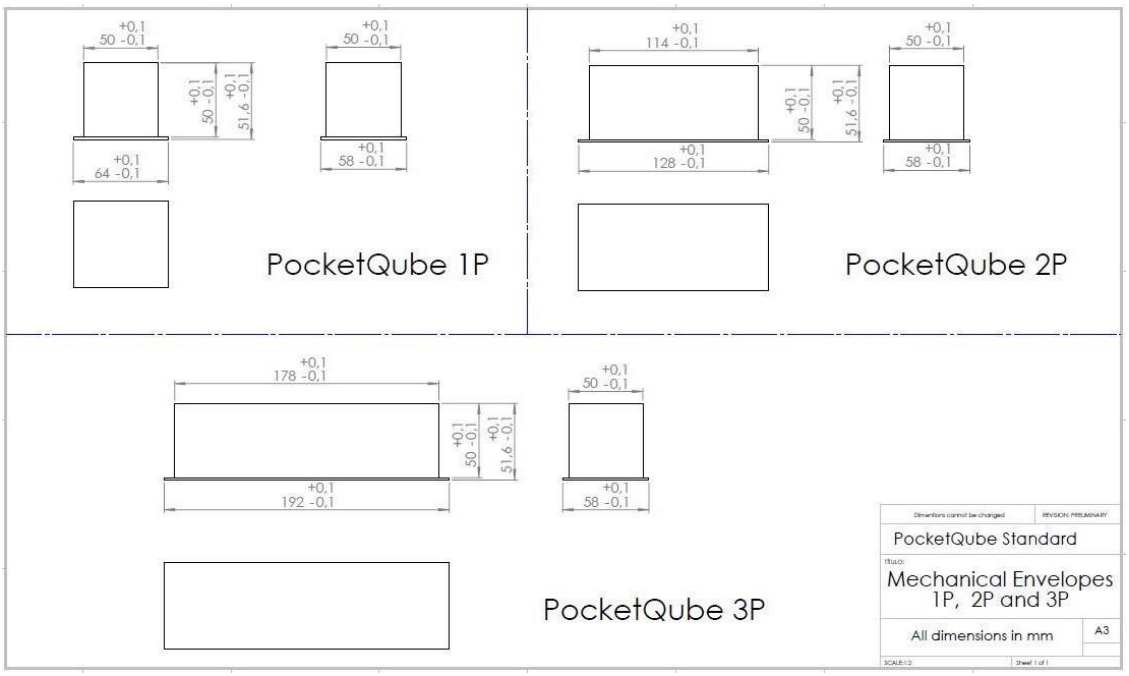

Figure 1.8: PocketQube Standard Dimensions [11].

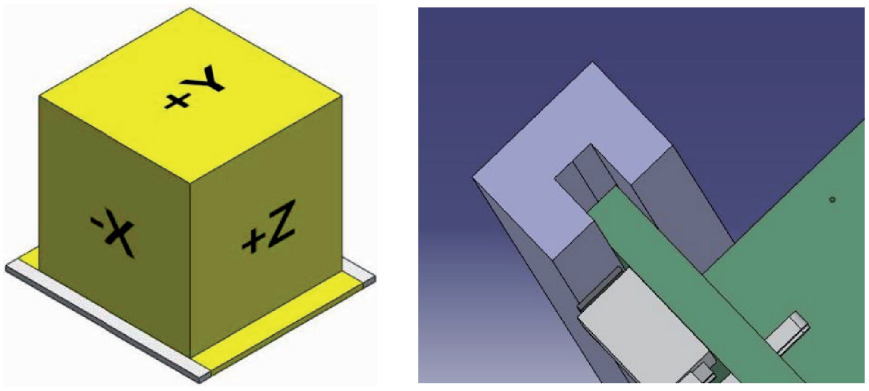

Figure 1.9: Focus on the Sliding Backplate for PocketQube Ejection [11].

As of now, the PocketQube standard primarily includes mechanical specifications, with the plan to include electrical, operational and testing requirements in the future revisions.

Twiggs' idea seems to be again a success. As Alba Orbital declares on its website [12], PocketQubes launch services significantly reduce the costs with respect to CubeSat launches: while a 1U CubeSat launch may cost approximately $100.000 and a 3U CubeSat launch around $ 300.000, a 1P PocketQube can be launched for just € 25.000 in Low-Earth Orbit (LEO).

As a demonstration of the feasibility of this new small form factor, on November 21, 2013, the first four PocketQube satellites were launched onboard of the UniSat-5 mothership, which was inserted into a near-Sun-Synchronous Orbit (SSO) at an altitude of 634 km [13]. Morehead State University, in collaboration with GAUSS Srl and Kentucky Space, developed a dedicated deployer called Morehead Rome Femto Orbital Deployer (MR-FOD) which was installed within the UniSat-5 and it successfully released all the four pico-satellites:

- **Eagle-1**, 2.5P, from Morehead State University and Sonoma State University (USA) [14];
- **Eagle-2** (aka $50SAT), 1.5P, from Morehead State University (USA), Figure 1.10 [15][16];
- **QBScout**, 2.5P, from University of Maryland, Baltimore County (UMBC) (USA) [17];
- **WREN**, 1P, from STADOKO UG (Germany), Figure 1.11 [18].

The successful deployment of these four PocketQubes during the UniSat-5 mission (Figure 1.12) reaffirmed their cost-effectiveness and highlighted their significance as a valuable platform for engineering and science students to gain practical skills. In particular, the $50SAT PocketQube showcased the viability of very low-cost satellites in Low Earth Orbit (LEO), further enhancing the affordability of space access for educational institutions.

Figure 1.10: Eagle-2 also know as $50SAT, 1.5P PocketQube from Morehead State University (USA) [15][16]. It can be noticed the Backplate used for deployment.

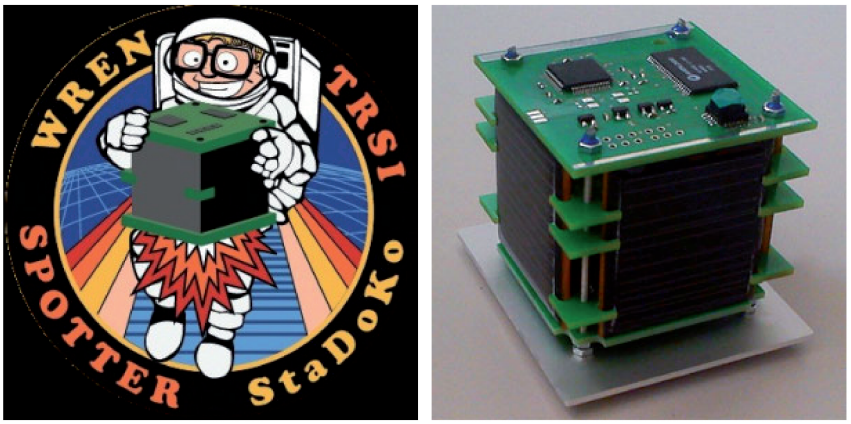

Figure 1.11: WREN, 1P PocketQube from STADOKO UG (Germany) [18].

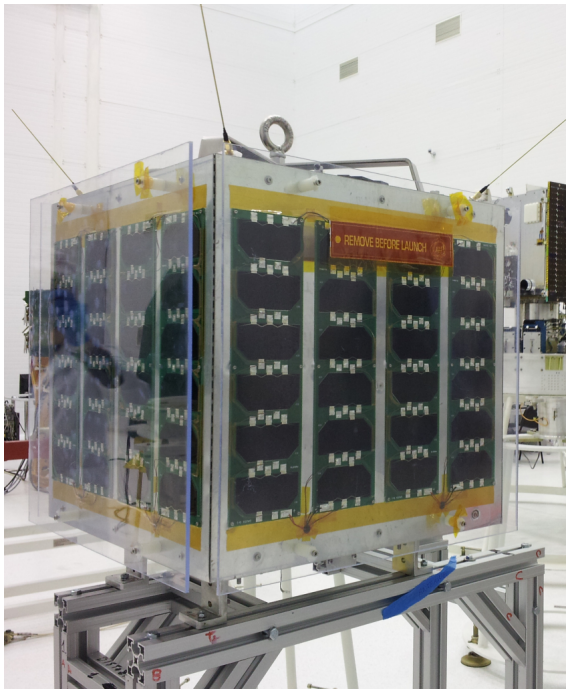

Figure 1.12: UniSat-5, an educational civilian microsatellite, features a cuboid aluminum structure measuring 50 x 50 x 50 cm, with a total mass of 35 kg. It is the first satellite designed, built and launched by GAUSS Srl, an Italian private company [19].

1.2 Newer Approach to Space Missions

Taking inspiration from nature, specifically animal reproductive strategies, Adams and Peck from Cornell University have made interesting considerations about the new paradigm introduced by femtoSatellites in space exploration and exploitation [20].

As previously stated, pico- and femto-satellites possess distinguishing characteristics compared to traditional satellites: they can be rapidly designed and integrated using cost-effective Commercial Off-the-Shelf components. The authors draw a parallel between this approach and certain animal species. For instance, sea turtles produce a large number of offspring with minimal investment in each individual. Although the survival probability for each offspring may be low, the overall population remains healthy due to the significant quantity produced.

In contrast, human or whale species produce a relatively small amount of prole, requiring a tremendous amount of time and energy. However, these offspring benefit from long lifespans and low mortality rates. The analogy with traditional satellites is evident: they require significant investments in terms of both time and money, but they have an high success probability in their missions.

Adams and Peck classify species like humans and whales as K-selected, while animals like sea turtles are considered R-selected species.

The parallelism becomes clear: K-selected spacecraft requires a huge investment of money and time, with only a few units produced. However, these units are perfect and can rely on long lifespans fundamental for their mission accomplishment (Figure 1.13).

Figure 1.13: K-Selected Species: Traditional Satellites and Humans.

On the other hand, R-selected spacecraft follow a faster development cycle, can be manufactured at a lower cost, and can be produced in large quantities.

If some of these satellites do not survive the harsh space environment, the mission may still be accomplished with the remaining swarm (Figure 1.14).

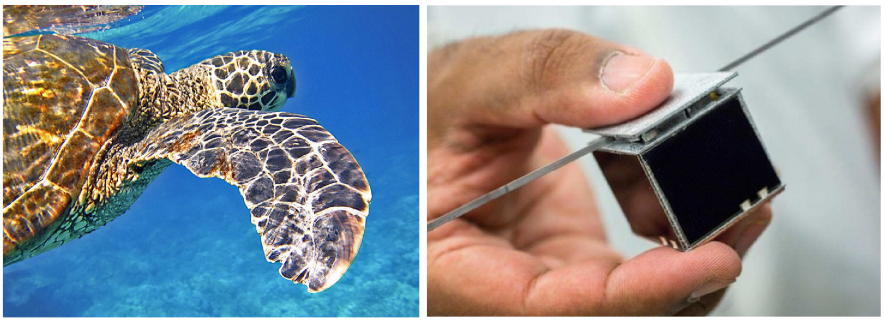

Figure 1.14: R-Selected Species: Sea Turtles and femtoSatellites.

This approach presents a different perspective on space access and exploration: numerous inexpensive units are deployed, trading high quantity for reduced risk. It does not replace traditional missions but rather introduces a complementary approach that enables new kind of missions, such as Distributed Spacecraft Missions (DSMs).

1.3 Distributed Spacecraft Missions (DSM)

Le Moigne *et al.* defined Distributed Spacecraft Missions (DSMs) and provided an accurate taxonomy that describes the characteristics of DSMs and related concepts such as their organisation, physical configuration, and functional configuration in [21]. A DSM is defined as *a mission that involves multiple spacecraft to achieve one or more common goals*. The term "multiple" refers to "two or more", including tethered or untethered satellites [21].

1.3.1 DSMs Driving Factors

Before discussing the various peculiarities of distributed missions, it is important to understand some of the key driving factors that have made DSMs a prominent field of research in recent years.

As mentioned in the previous sections, advancements in microelectronics have enabled the miniaturisation of electronic devices and instruments that can be installed in smaller satellites which can be mass produced in a

cost-effective manner. The availability of smaller yet more efficient microprocessors has also played a significant role in the design of DSMs [21].

The increased frequency and ease of satellite launches, particularly for smaller satellites that can be piggybacked as secondary payloads, have also contributed to the feasibility of DSM missions [21]. The promising growth of the small satellite economy and the abundance of very small satellites developed in recent years have also stimulated the development of dedicated launchers. One notable example is the EOS Vehicle, currently under development by Sidereus Space Dynamics, an Italian aerospace start-up (Figure 1.15). The EOS Vehicle is envisioned as a fully reusable Single Stage To Orbit (SSTO) launch vehicle specifically designed for small satellites and payloads weighing up to 10 kg. It will provide launch capabilities to and from a Sun-Synchronous Orbit (SSO) at an altitude of 550 km. Furthermore, the EOS Vehicle offers the flexibility of being launched from various locations with minimal to no additional infrastructure requirements [22].

Figure 1.15: EOS OC-2522 Ballon Tanks with Mattia Barbarossa alongside.

Other key driving factors are science related: multiple collaborative sensor nodes producing measurements from multiple vantage points and in multiple dimensions (spatial, spectral, temporal, radiometric[1]) can provide a dynamic and more complete picture of physical processes and natural phenomena [23].

[1]Radiometry is the science of measuring electromagnetic radiation emitted by a source, often defined in terms of power. Radiometric measurements extend past the visible region

Additionally, DSMs have significant implications for weather and climate prediction, as well as the prediction of natural hazards. Accurate predictions, in these areas, directly benefit the public, industries, federal state, and local governments. For example, farmers, food producers, and food processors can plan their operations more efficiently based on weather forecasts [24][25].

Moreover, DSMs can optimise the utilisation of renewable energy sources, such as wind and solar, by providing detailed local forecasting to manage these resources effectively. For instance, the Caribean Island of Guadeloupe is attempting to exploit its abundant wind, solar and water resources to generate most of its power. However, wind fluctuations and cloud cover reduces the contribution that wind and solar generation can make to the island's total needs therefore, a detailed local forecasting would assist the island in managing those resources more effectively, thus boosting the power generated [25].

Barrett [26] identified two other motivations for multiple spacecraft missions. Firstly, from a scientific standpoint, DSMs allow for better resolution, either enabling the isolation of the signal of a micro-phenomena or the coverage of the entire signal space for fast or macro-phenomena. Secondly, from an engineering perspective, DSMs offer extensibility to space missions, allowing for the addition, replacement, or redundancy of sensors in response to failures.

Another area of research that stands to benefit from DSMs is the Global Satellite Navigation System (GNSS), which requires accurate atmospheric models to enhance precision.

1.3.2 DSMs Origins

The concept of Distributed Spacecraft Missions builds upon earlier ideas and concepts.

In 2000, the National Aeronautics and Space Administration (NASA) proposed the Sensor Web as *the concept of integrating a constellation of Earth observing satellites into a cohesive network of measurement instruments* [27].

---

of the electromagnetic spectrum, into the infrared and ultraviolet. Radiometry is typically used to measure the total power output of an object in the infrared, visible, or ultraviolet spectrum, or to measure the spectral power distribution of a source. Of the many standard units and quantities used in radiometry, the principal concern is power per unit area which is defined as irradiance and is typically expressed in watts per square meter (W/m^2). Radiometry is important in astronomy, especially radio astronomy, and plays a significant role in Earth remote sensing.

Torres-Martinez *et al.* described the Sensor Web as *a virtual organisation of multiple numbers and types of sensors combined into an intelligent "macro-instrument" in which information collected by any one sensor could be used by any other sensor in the web, as necessary, to accomplish a coordinated observing mission* [24].

According to Lemmerman *et al.* the most unique feature of the Sensor Web is that information gathered by one sensor is shared and used by other sensors in the web, because each sensor is able to communicate within its local neighbourhood thus allowing distribution of information to the instrument as a whole [28].

The idea of the Sensor Web emerged from NASA's Earth Science Enterprise (ESE), which aimed at revolutionising the understanding of the Earth's environment and climate. Given the dynamic and interconnected nature of the Earth's environment, it became evident that confined measurements from a single sensor platform were inadequate. Thus, a flexible, reconfigurable, and cooperative observing system was necessary, leading to the development of the Sensor Web as a distributed, heterogeneous, adaptive, and cooperative observing system [28].

1.3.3 DSMs Characteristics

Distributed Space Missions encompass various types. A comprehensive taxonomy, including different definitions, is provided by Le Moigne *et al.* [21].

In terms of *Organisation*, two key characteristics define a DSM: appearance and inter-spacecraft relationship.

Regarding *appearance*, a DSM can be classified as:

- Homogeneous: in this case, DSM members consist of identical spacecraft, such as the Iridium Network (Figure 1.16);

- Heterogeneous: here, the spacecraft can be different from one another;
- Reconfigurable: this type of DSM has the ability to change one or more characteristics while on orbit. An example of reconfigurable homogeneous DSM is the Magnetospheric Multiscale (MMS) Mission (Figure 1.16) [29].

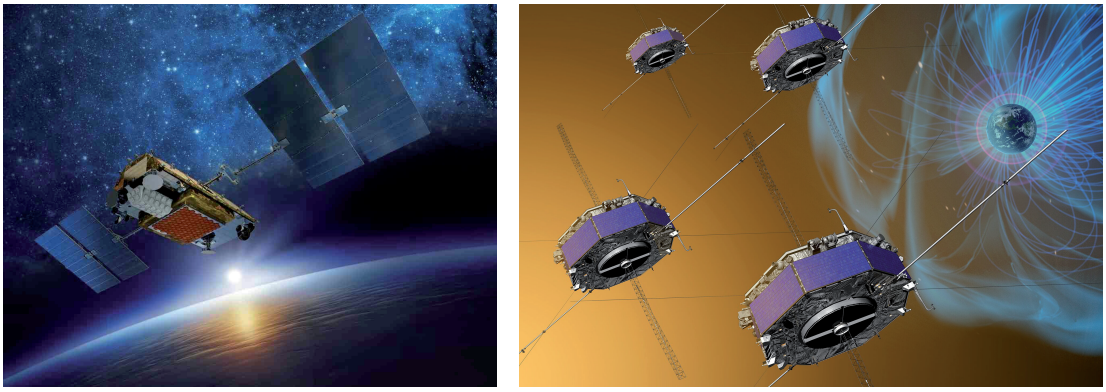

Figure 1.16: Iridium NEXT Satellite (left). Artistic Representation of Magnetospheric Multiscale (MMS) Mission (right).

Concerning *inter-spacecraft relationship*, a DSM can exhibit:

- No specific inter-spacecraft relationships;
- Hierarchical Relationship: this occurs when one spacecraft, called mothership, possesses higher capabilities and serves as a central focal point;
- Peer-to-Peer Relationship: in this scenario, all distributed spacecraft can interact with every other having equivalent control, capabilities, and responsibilities;
- Rendezvous Mission: this involves two spacecraft performing an orbital manoeuvre to closely approach each other and establish actual (docking) or visual contact. A Rendezvous Mission can be Cooperative, when both spacecraft collaborate to perform the manoeuvre, or Uncooperative, when a controlled spacecraft approaches an uncontrolled spacecraft or space object.

Another important DSMs aspect is their *Physical Configuration*, which can be further subdivided in Spatial Relationship, Spatial Control, Temporal Relationship, and Temporal Control [21].

Concerning the *Spatial Relationship*, DSMs can be classified as either Constellations or Virtual Missions.

A *Constellation* is a mission that is originally conceived as a DSM, therefore it consists of two or more spacecraft working towards a common objective. A General Constellation can have various attributes, such as being uniform when its members are evenly distributed.

A Constellation can be classified as *Formation* when the relative distances and three-dimensional spatial relationships between the members are tightly controlled. A special case of Formation is the String of Pearls Formation, when the spacecraft fly on the same orbit separated by fixed distances. The Gravity Recovery And Climate Experiment (GRACE) Mission is an example of Formation. GRACE was a gravity study mission that consisted of two identical satellites, GRACE-A and GRACE-B, that mapped Earth's gravity field by making accurate measurements of the distance between them (Figure 1.17) [30].

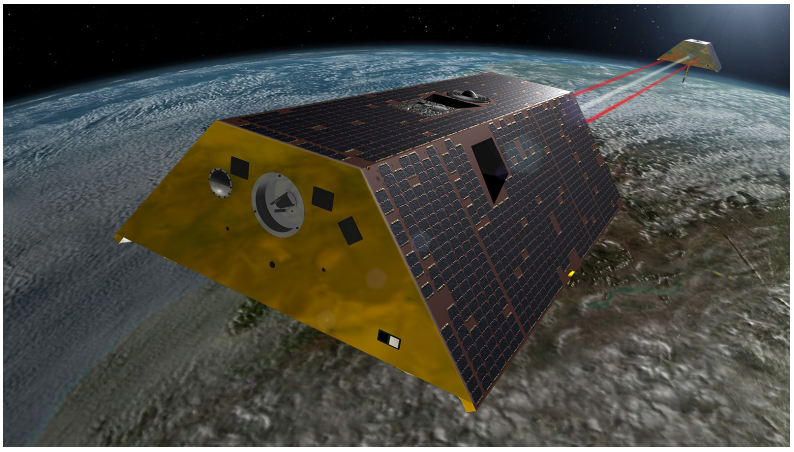

Figure 1.17: Gravity Recovery and Climate Experiment (GRACE) Mission [31].

Another type of Constellation is the *Fractioned Spacecraft* which, as the name suggests, is like a traditional monolithic spacecraft fragmented into multiple modules that are not structurally connected but share their different resources to function as a whole. In this case the modules are heterogeneous and perform distinct functions. An example of Fractioned Spacecraft is the DARPA F6 System whose intent was indeed to *demonstrate the feasibility and benefits of a satellite architecture wherein the functionality of a traditional "monolithic" spacecraft is delivered by a cluster of wirelessly interconnected modules capable of sharing their resources and utilising resources*

found elsewhere in the cluster (Figure 1.18) [32].

Figure 1.18: DARPA System F6 Program (F6 is short for Future, Fast, Flexible, Fractionated, Free-Flying Spacecraft united by Information eXchange) [33].

Finally, a Constellation is defined as a *Cluster* when the spacecraft are not uniformly distributed.

On the other hand, in contrast to a Constellation, that is conceived as a DSM from the beginning, there is the concept of a *Virtual Mission* (or Ad Hoc Mission). A Virtual Mission *exploits observations made from multiple missions that were designed independently, but the output can be considered in a coordinated fashion as if they were acquired from a single mission* [21].

The *Spatial Control* of a DSM can be categorised as follows:

- Pre-Determined: in this case, the mission does not have any spatial control except for the predetermined settings before launch;
- Ground Controlled: the mission is spatially controlled by ground operators;
- On-Orbit Controlled: the constellation is spatially controlled in orbit with some level of autonomy. A particular case is the *Swarm*, which consists of a high number of spacecraft working together to achieve the same objective, with little to no knowledge about the other uncontrolled or loosely coordinated satellites from the ground;
- Mix of Ground and On-Orbit Controlled: Formation Flyers (FFs) fall into this category. They can be either a *"Tight" Formation Flying*, when

the application has strict requirements regarding the spatial distribution of the spacecraft within the FF, or a *"Loose" Formation Flying*, where a smaller degree of precision and accuracy is required between the spacecraft in the FF.

The *Temporal Relationship* mainly concerns the deployment of the spacecraft in a DSM. An *All At Once Deployment* means that all the mission members are deployed simultaneously and become operational at the same time. On the other hand, a *Phased Deployment* is typically planned for very large constellations (megaconstellations), where groups of spacecraft are launched incrementally by design [21].

Temporal Control refers instead to the timing coordination required for acquiring measurements in a DSM. Measurement acquisitions can be *Pre-Determined*, where no specific temporal control is needed. *Precise Observation Timing* may be necessary for applications that require highly intercorrelated measurements. Another possibility is the *Flash Mob*, where satellites can agilely react to real-time events and phenomena [21].

Many other DSM characteristics have been defined by Le Moigne *et al.*. Interested readers can refer to [21] in order to delve deeper into the topic.

Figure 1.19 clearly concludes this introduction to Distributed Spacecraft Missions by graphically representing the characterisation of each mission typology in terms of spatial distribution of the spacecraft and the required coordination level.

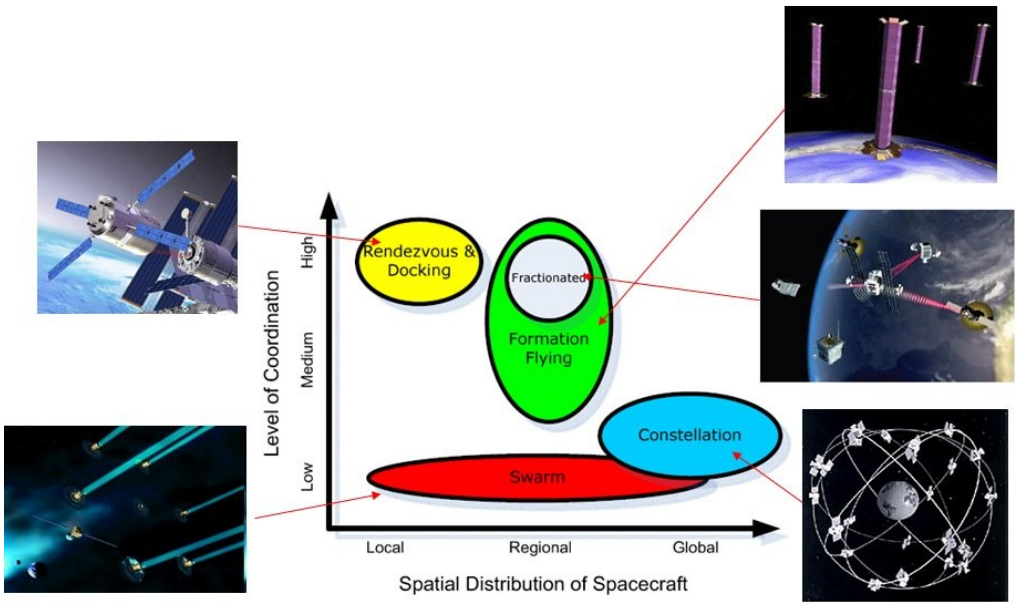

Figure 1.19: Distributed Space System concepts according to the Spatial Distribution and the Coordination Level of the Satellites [34].

Chapter 2

Literature Review

This Chapter provides a comprehensive literature review. Various femtoSat prototypes that have been developed and, in some cases, launched in the past will be presented.

2.1 femtoSat Prototypes

2.1.1 Sprites and KickSat by Zachary Manchester

The Sprites, designed and developed by Zachary Manchester at Cornell University, are probably the most successful femtoSat prototypes ever built. The prototypes have flown four times.

Figure 2.1: Materials International Space Station Experiment (MISSE) Logo.

In May 2011, as part of the 8th Materials International Space Station Experiment (MISSE-8), three Sprite prototypes were mounted outside of the International Space Station (ISS) on a Passive Experiment Container (a

briefcase-like container that is used to transport experiments to and from ISS) (Figure 2.3). Despite the prototypes were launched as functioning and likely remained operational during their time in orbit, they were mounted on a position that prevented the reception of any signal from Earth [35].

After spending three years in Low Earth Orbit (LEO), the MISSE-8 Experiment was returned to Earth on board of the SpaceX CRS-3 mission in May 2014. Tests performed on the flown prototypes revealed that two of the three prototypes were still working properly (Figure 2.2). This provided evidence that the Commercial Off-the-Shelf components utilised in the construction of the Sprite prototypes could endure the LEO space environment for extended periods of time [36].

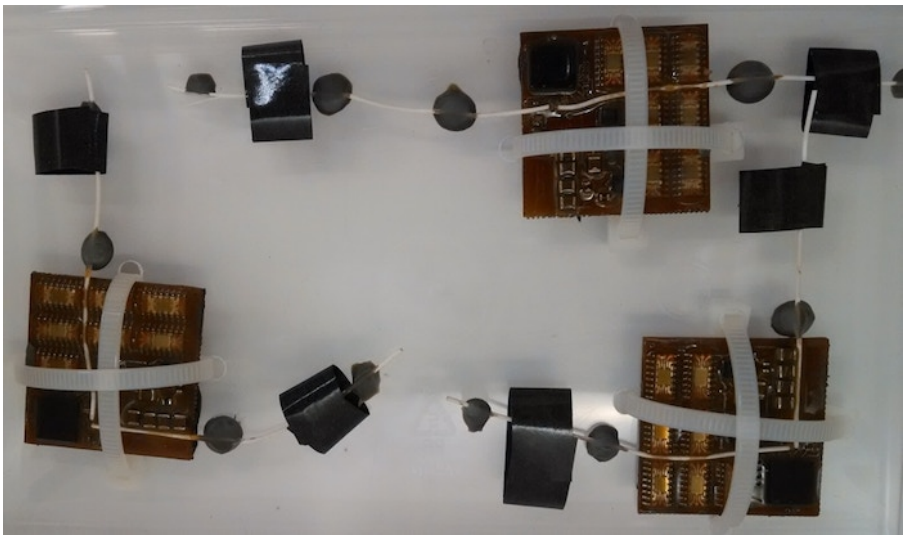

Figure 2.2: The three Sprite Prototypes clearly proved by the harsh space environment after three years outside of the ISS.

On April 18, 2014, the KickSat, a 3U CubeSat designed by Manchester in order to carry and deploy the Sprite prototypes, was launched on board of the SpaceX CRS-3 (Cargo Resupply Services-3, the same mission that brought back to Earth the Sprite Prototypes of MISSE-8 Experiment). The KickSat was released at an altitude of approximately 325 km[1] [38] and, after

[1]The KickSat was deployed at this altitude because, if released at higher altitudes, over 400 km, Sprites could have become uncontrollable pieces of space debris posing at grave risks the astronauts that were in a Soyuz Rocket en route to the ISS at the time. The U.S. Air Force uses powerful radars to catalog and track most of the space debris to provide early warnings for astronauts and satellites, but Sprites would have been so small

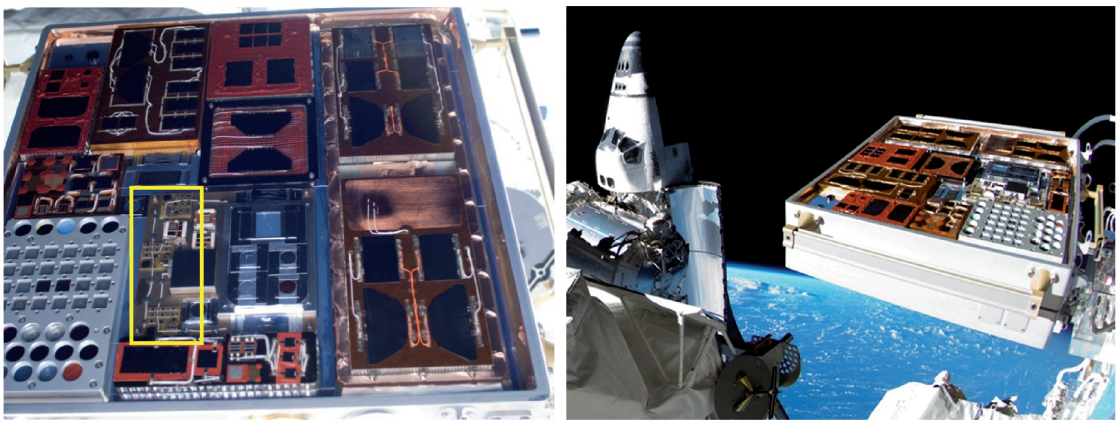

Figure 2.3: The three Sprite Prototypes mounted on the PEC of MISSE-8 Experiment placed outside of the ISS.

deployment, it powered up and started a countdown: at 30 minutes the UHF radio antenna was deployed and at 45 minutes the KickSat began transmitting a beacon signal. After 16 days from launch, the Sprites were supposed to be deployed. However, probably cause of a radiation event, an hard reset of the watchdog microcontroller responsible of keeping the KickSat master clock, occurred and thus the master clock reset too. The 16 days countdown for Sprites deployment started again from zero consequently delaying the deployment of 16 days. However, the KickSat, as planned, was likely reentering the atmosphere before the 16th day [39]. The KickSat's uplink radio was the last chance to command the deployment but it required a battery voltage of at least 8 volts. Unfortunately the batteries never reached the required state of charge, consequently the uplink radio was never operational and the KickSat never deployed the 104 Sprite prototypes that it was carrying.

While disappointed because things did not go as planned, Manchester promised that this was not the end of the KickSat Project.

that they were likely to slip that surveillance. Therefore, the U.S. federal officials have forbidden from releasing the KickSat, and consequently the Sprites, at an altitude higher than 400 km above Earth. Below that threshold, the KickSat and Sprites orbits would have decayed relatively quickly, allowing them to harmlessly re-enter and burn up in the atmosphere within weeks or months [37].

On June 23, 2017, six Sprite Prototypes flew again onboard of two motherships: the Venta-1[2] and the Max Valier[3] (Figure 2.4). One Sprite apiece was attached to the outside of each mothership and the remaining four units were carried by the Max Valier Satellite and they were supposed to be deployed once in orbit as independent spacecraft [37]. Unfortunately, the mission controllers were not able to establish a connection with the Max Valier Satellite therefore the Sprites could not be deployed. Nevertheless, for what concern the Sprites, the mission was still a success because signals from at least one of the exterior-mounted Sprites were received on Earth demonstrating the feasibility of a communication link with very low power (10 mW) from LEO Orbits (505 km).

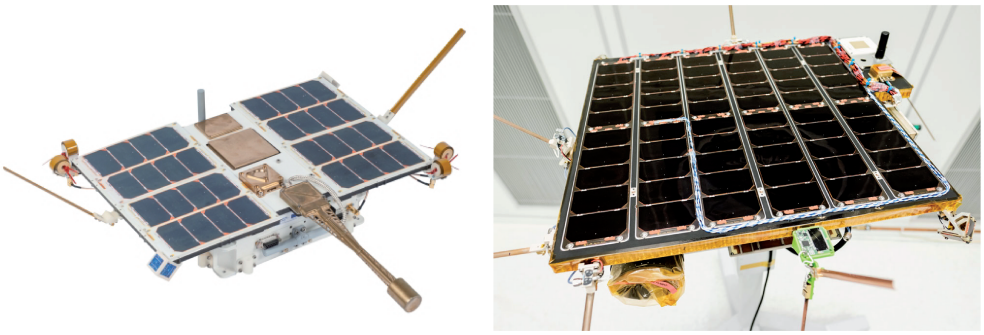

Figure 2.4: Venta-1 (left) and Max Valier (right).

On February 6, 2015 the KickSat-2 was selected for a launch by NASA's CubeSat Launch Initiative [44]. It was supposed to fly on the Cygnus CRS-6, but was delayed due to the lack of a suitable CubeSat co-passenger for the

[2]The Venta-1 nanosatellite, measuring 70 x 40 x 13 cm and weighing 5 kg, was developed by Ventspils University College in cooperation with Ventspils High Technology Park, Bremen University of Applied Sciences and OHB Systems. Its primary objective was to supervise the ship traffic in Europe by means of Automatic Identification System (AIS) receivers mounted onboard of the spacecraft. Venta-1 was launched aboard the Indian launch vehicle PSLV-C38 stacked with the Italian Max Valier satellite. Both the satellites were deployed in a Sun-synchronous near-circular orbit at an altitude of 505 km [40][41].

[3]The Max Valier nanosatellite, weighing 16 kg, was designed by the "Max Valier" school Bolzano and the "Oskar von Miller" school Merano, in South Tyrol, Italy. The satellite carried as primary instrument the small X-ray telescope μRosi provided by the Max Planck Institute for Extraterrestrial Physics (MPE), in Garching (Germany). The telescope enabled amateur astronomers to conduct the first-ever sky scan in the X-ray frequency range [42][43].

deployer. A launch on Cygnus CRS-5 was then planned, but issues with the experimental license from the Federal Communications Commission (FCC) delayed it to a later launch [45].

Figure 2.5: Cygnus NG-10 Commercial Resupply Services (CRS) Logo.

On November 17, 2018, as part of the 16th Educational Launch of Nanosatellites (ELaNa-16) Mission, the KickSat-2 was finally launched on board of the Cygnus NG-10 cargo vehicle. The Cygnus NG-10 spent 81 days attached to the International Space Station (Figure 2.6).

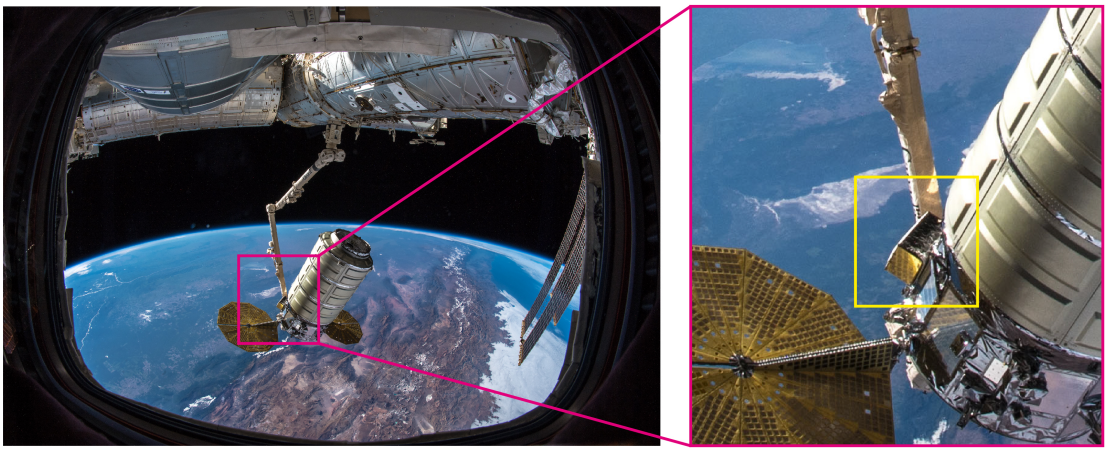

Figure 2.6: The Cygnus NG-10 docked with the International Space Station, prior to the deployment of KickSat-2. The CubeSat can be seen connected to the Cygnus spacecraft as the gold-tinted box near the docking arm of the ISS [46].

On February 8, 2019, the Cygnus departed from the ISS and raised its orbit of about 100 km above the ISS, where some of the piggybacked satellites had to be released.

After its orbit above ISS, on February 13, 2019, the Cygnus lowered its orbit to about 300 km where the KickSat-2 was deployed. A lower altitude

was chosen for the KickSat-2 in order to ensure that the Sprite satellites, once released, would not last long before being pulled back into atmosphere preventing them to become space debris [47].

On March 18, 2019 over 100 Sprite Prototypes were finally deployed by the KickSat-2 and the first signals were received the following day [46]. The prototypes remained in orbit for only a few days before re-entering the Earth's atmosphere. This latter is a key aspect of Sprites' design because it ensures that they do not pose a risk as space debris [48].

The Sprites

With the size of a couple of postage stamps, 3.5 x 3.5 cm, few millimetre thickness and a mass of just 4 grams, the Sprite Prototypes are probably the smallest satellites that have ever flown.

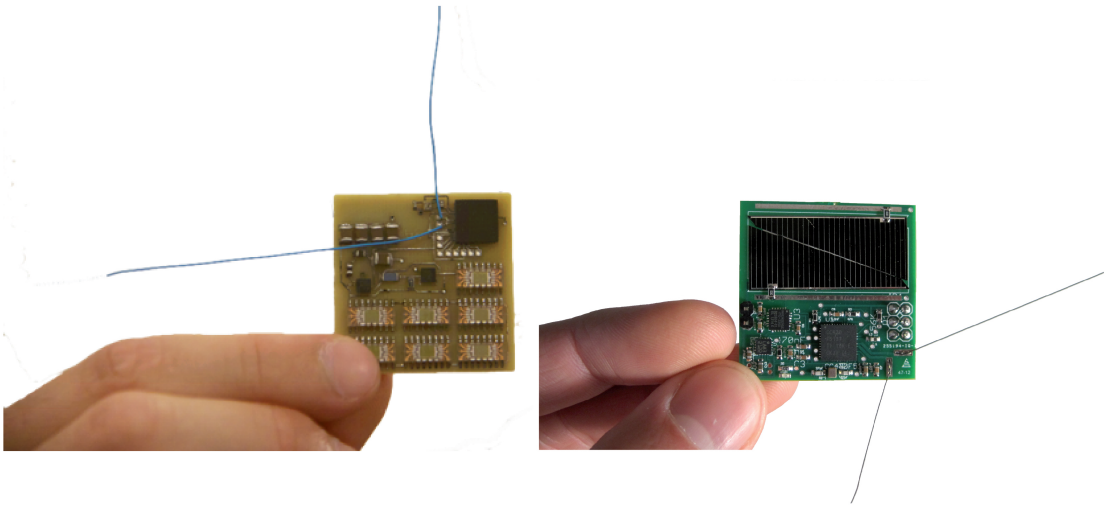

Figure 2.7: The Sprite Prototypes by Zachary Manchester, the first version (left) and the second one (right) [35].

One of the key features of the Sprite Prototypes is that they have been built with Commercial Off-the-Shelf Components making them really cost-effective as they cost under $ 100 apiece.

Each Sprite is equipped with a CC430 System-on-Chip (SoC) by Texas Instrument which includes a 16-bit MSP430 microcontroller, that provides computing capabilities, and the CC1101 UHF transceiver, that enables the Sprite's communication. The radio is capable of an output power of 10 mW (10 dBm) on the 437 MHz band and it requires approximately 35 mA while

transmitting. It is worth recalling that both the MSP430 and CC1101 had flight heritage on previous CubeSat missions [49][50].

The antenna is an half-wave V-dipole made of superelastic nitinol, a nickel-titanium alloy commonly referred to as "shape-memory alloy" since it can undergo very large strain and still return to its original shape. Nitinol was chosen so that the antenna could have been tightly coiled for launch and then it would have returned to its original shape after deployment [35].

Each Sprite also includes a Honeywell HMC5883L three-axis magnetometer and an InvenSense ITG-3200 three-axis MEMS gyroscope.

Concerning the power required on board, it is generated by two Spectrolab Triangular Advanced Solar Cells (TASC) each capable of generating 30 mA of current when directly aligned with the sun sensor with an open-circuit voltage of 2.2 V.

No batteries were included as Manchester declares that the cold temperatures encountered during eclipse would permanently damage Lithium-Ion or Lithium-Polymer chemistries.

As a ground station, a low-cost Software Defined Radio (SDR) architecture was chosen. It included a Yagi antenna, a low-noise amplifier (LNA), a low-cost USB software-defined radio receiver and a laptop computer running the GNU Radio software (Figure 2.8) [35].

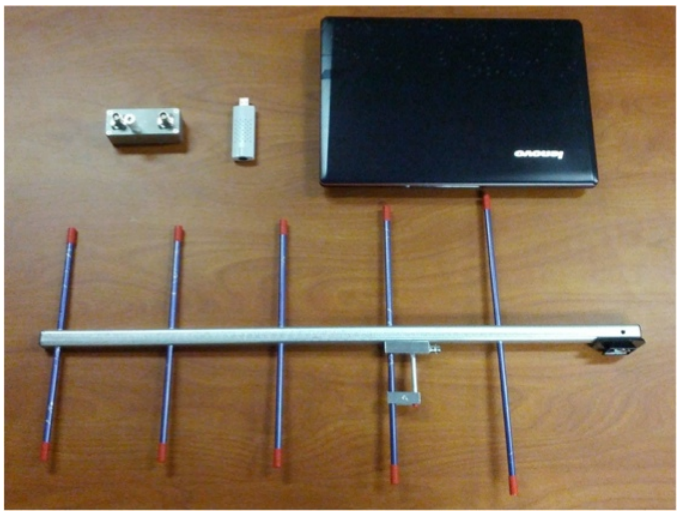

Figure 2.8: The Ground Station Hardware [35].

As mentioned above, another paramount aspect of Sprites design is that, due to their extremely low ballistic coefficient, they are expected to remain in orbit for only a few days before reentering and burning up in the atmosphere,

alleviating debris concerns [35].

The KickSat

The KickSat Spacecraft is a 3U CubeSat that Manchester purposely designed as Sprites' deployer (Figure 2.9).

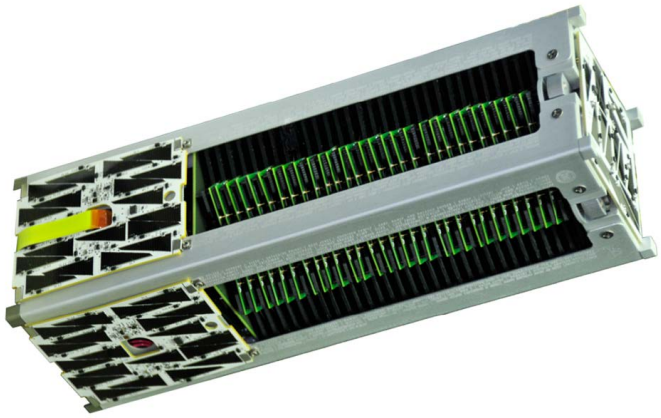

Figure 2.9: The KickSat Spacecraft [35].

It consists of two compartments: one unit run the spacecraft by providing power, communications and data-handling, the other two units contain the Sprites deployment mechanism that can hold up to 104 units. The coiled nitinol antennas on the Sprites double as deployment springs to push the Sprites out of their slots (Figure 2.10).

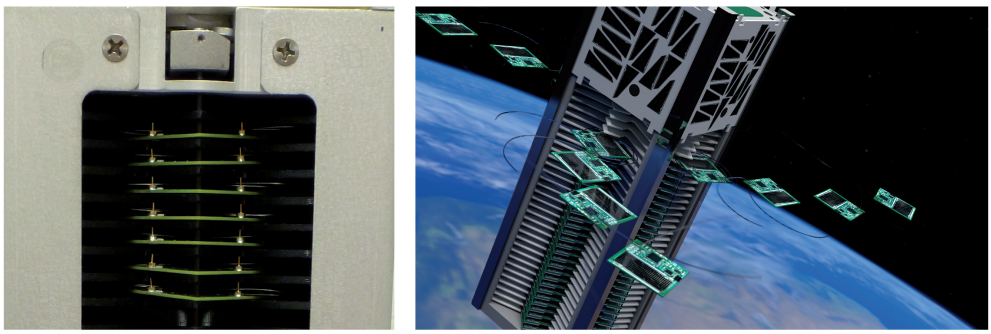

Figure 2.10: A photo of the Sprite Prototypes inside the KickSat deployer (left) and an artistic representation of the KickSat while deploying the Sprites (right).

An interesting aspect of the KickSat Project is that it aimed at demonstrating the deployment and operation of the Sprite ChipSats, which was a revolutionary idea at the time, and it was funded by over 300 individual backers on the crowd-funding website KickStarter.

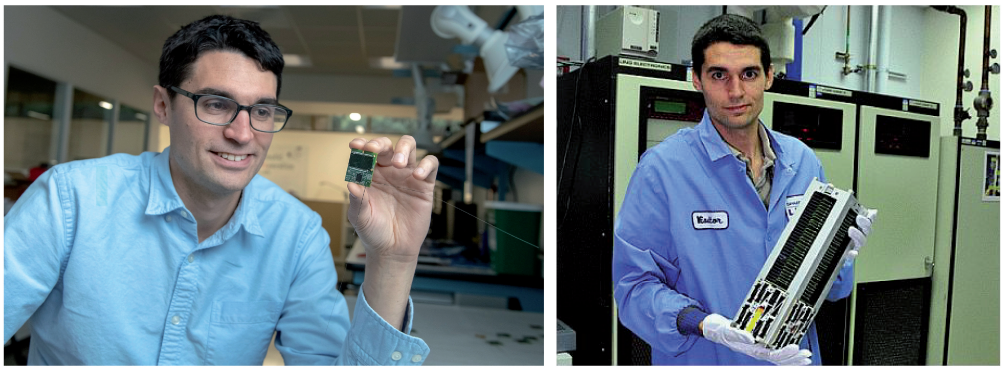

Figure 2.11: Zachary Manchester with a Sprite (left) and a KickSat (right).

2.1.2 Monarch by Adams and Peck

Adams and Peck, the authors from Cornell University that introduced the concept of R-Selected Spacecraft [20], designed the Monarch femto-Satellite to realise their idea of trading high quantity for low risk (instead of high cost for low risk).

As an R-Selected Spacecraft, the Monarch has an higher probability of failure compared to conventional K-Selected Spacecraft. However, the mission's success is not dependent on every single unit of the swarm but it depends on the statistical probability that enough units will survive and complete the mission.

Another interesting feature of these small satellites is that the small form-factor provides advantages in terms of impact and shock resistance. Drawing inspiration from nature, where insects can withstand shocks that larger animals cannot, the authors aptly describe the Monarchs as the "insects of spacecraft". This attribute makes femtoSats well-suited for descending to the surfaces of celestial bodies, as the Entry, Descent, and Landing (EDL) procedures significantly differ from those of conventional spacecraft. Also in this missions, the focus is not on ensuring the survival of every individual Monarch satellite, but rather on guaranteeing the survival of a sufficient number of units to accomplish the mission objectives (Figure 2.12).

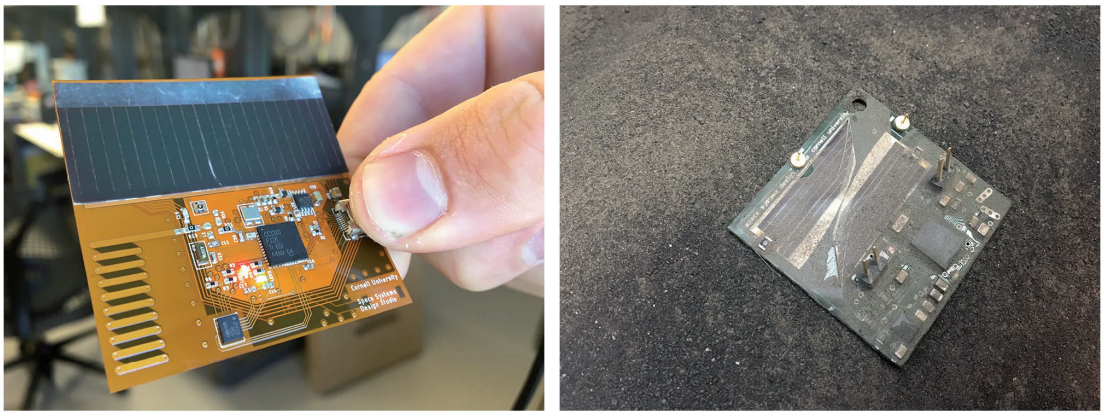

Figure 2.12: A Monarch Prototype (left) and a Monarch Precursor (right) after a simulated impact with the lunar surface. The precursor carries the same Inertial Measurement Unit (IMU) which results to be the most shock-sensitive component on the spacecraft due to its internal mechanics [20].

At the same time, the small form-factor raises concerns about populating the space environment with even more space debris. However, if these small satellites are deployed in Very Low Earth Orbits (V-LEO), their low ballistic coefficient causes atmospheric drag to quickly deorbit them in a matter of days [20].

Considering these factors, the design of the Monarch had to be cost-effective and suitable for large-scale production. Taking advantage of the consumer electronic commerce, which allowed for mass production at reduced costs, the Monarch prototypes were produced using automated processes similar to those used for smartphones and other electronic devices.

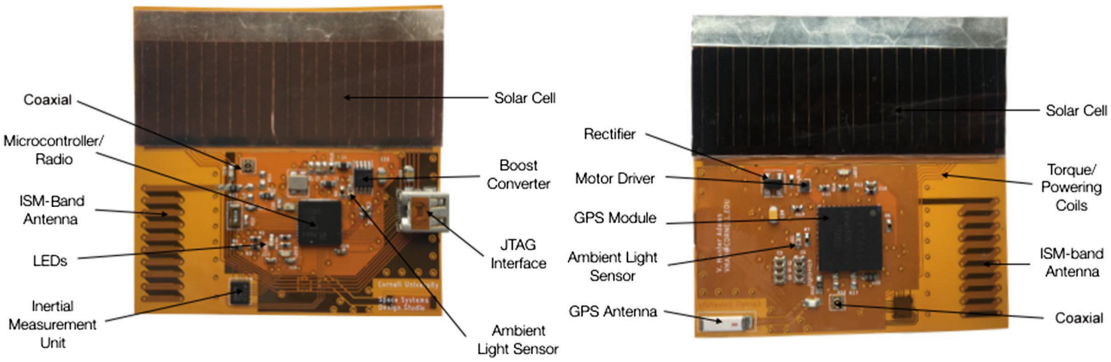

Figure 2.13: The Monarch Prototype by Adams and Peck [20].

Despite their small form factor, the Monarch Prototype include most of the typical subsystems found in spacecraft.

The Telemetry, Tracking and Command (TT&C) Subsystem is composed by a 25 mW Industrial, Scientific, Medical (ISM)-band (915 MHz) Radio with a Printed Circuit Board (PCB) antenna.

The Monarchs' Power Subsystem does not include a storage device (battery) therefore they enter sleep mode during eclipse and operate when illuminated by the sun. The authors decided to not include a battery because the energy required to keep it warm during eclipse would have outweighed the energy that could be stored in sunlight. They proposed as an alternative solution the use of a small capacitor which could enable the Monarch to operate in low-energy-consumption mode during eclipse.

For the Attitude Determination, each unit is equipped with a gyroscope, accelerometer, magnetometer, and light sensors that can serve as a coarse sun sensor. A GPS receiver and antenna are included to determine (possibly) the position of each unit. Attitude Control is achieved through a magnetorquer, which consists of a coil of wire lying on the PCB that generates a local magnetic field when current flows through it.

For what concern the Payload, Monarchs are supposed to carry sensors for in-situ measurement of the space environment.

As typical of small satellites, the authors remark that Monarch Prototypes could enable two main types of missions. First, they can facilitate spatially distributed measurements of various quantities in the space environment. Second, their small form factor makes them suitable for missions where individual satellites are subjected to extremely high levels of risk. However, given their disposable and cost-effective nature, the success of the mission depends on the statistical probability of a sufficient number of spacecraft surviving [20].

Differently from the Manchester's Sprites, the Monarchs have never flown.

2.1.3 SpaceChip by Barnhart *et al.*

In 2007, Barnhart *et al.* from the Surrey Space Centre at the University of Surrey, developed the first conceptual design of a Satellite-on-Chip called the SpaceChip [51]. This innovative design was proposed as a solution to the large number of satellite nodes that a distributed space mission requires.

As the SpaceChip name suggests, the idea was to embed all the necessary spacecraft functionalities in a monolithic System-on-Chip (SoC), with

Figure 2.14: Artistic representation of a swarm of networked Monarchs performing a Distributed in-situ Sensing Mission in Low Earth Orbit [20].

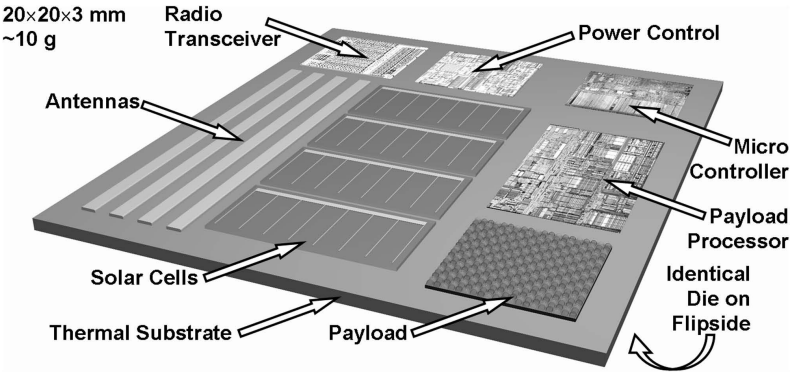

Figure 2.15: Notional SpaceChip Configuration [51].

a target cost of less than $ 500 [51]. However, the commercial Complementary Metal-On-Silicon (CMOS) Technology, on which the SoC approach relies, imposes limitations on the maximum available area of the SpaceChip, restricting it to 20 x 20 mm^2, and a total mass of less than 10 grams [52].

As for the Payload, the SpaceChip was designed to incorporate a CMOS imager that could be easily integrated on the CMOS die with its micro-lenses. Additionally, a variety of sensors (infrared, magnetic, pressure, chemical, etc.) could be integrated into each unit.

Integrating the solar cells in the CMOS substrate posed a significant challenge for the authors, as solar cells are typically fabricated using different processes than standard CMOS technology, such as Silicon (Si) or Gallium Arsenide (GaAs). Nonetheless, the authors calculated that an area of 12 x

12 mm^2 (35% of the maximum reticle area) would be sufficient to achieve an average solar array output power of 1.34 mW (the SpaceChip Power Budget), which was a promising result.

Regarding Power Storage, incorporating a capacitor as part of the monolithic CMOS design was the only viable option. However, even with an high-capacitance option (4.8 $fF \cdot \mu m^2$ in SiGe-BiCMOS), the capacitor would require an area much larger than the die area, making it impractical [51]. The authors suggested the use of an external thin-film battery as a possible solution if power storage was necessary.

Another problem was the integration of panels on one side (active side) of the substrate, which meant that the SpaceChip would only function when the active side was illuminated. To overcome this limitation, the final configuration consisted in two identical dies attached together on a thermal substrate without any interconnection between them. In this way, one side at a time would function when illuminated by the Sun [51].

The Communication Subsystem posed another challenge for such small form-factor. A conventional radio transceiver for effective downlink communication would require an area of at least 50 cm^2, far exceeding the available space on the SpaceChip die. Additionally, tracking the individual SpaceChip units, which is important to avoid pointing losses, would be difficult due to their small size, making it unlikely that space surveillance networks could detect them. To address these challenges, an architecture was proposed that included a Mothership responsible for relaying data collected from each SpaceChip to ground stations. Both the SpaceChips and the Mothership were designed to operate in the unlicensed 2.4 GHz ISM band.

Another consideration made by Barnhart *et al.* was the temperature range the SpaceChip should withstand, which was calculated to be -72°C to +96°C. This range was deemed reasonable since commercial electronic components can operate in temperatures ranging from -50°C to +85°C [53].

With the proposed design choices, a SpaceChip mission would have a limited duration after separation from the Mothership. Due to the difference in drag between the SpaceChips and the Host Satellite, the units would eventually drift apart, thus rendering communication and consequently data download to ground stations impossible.

The SpaceChip, being a conceptual design, was never fabricated and thus it has never flown.

2.1.4 PCBSat by Barnhart *et al.*

The PCBSat is another attempt from Barnhart *et al.* to design a cost-effective small-satellite as a response to the necessity of disposable, low-cost femtoSatellites to enable Distributed Space Missions (DSM) [54].

Traditional spacecraft were not suitable for DSMs due to their custom manufacturing processes, which resulted in high unit costs. In response, Barnhart developed a satellite-on-a-PCB concept with the goal of determining which capabilities can be included in a femto-class spacecraft with the constraint of utilising just Commercial Off-the-Shelf (COTS) components, in order to reduce the cost of each prototype produced.

The PCBSat was assembled by hand, with all the components soldered onto a PC104 PCB which determines the 10 x 10 x 2 cm size of the spacecraft. This form-factor is also compatible with P-POD Deployers, commonly used for CubeSats, where 15 PCBSats can be stored for launch and then released on orbit.

Concerning the Subsystems, the Payload of the PCBSat consists of a 640 x 480 CMOS Imager from ST Microelectronics.

The Electrical Power System (EPS) relies on seven solar cells attached to the back side of the PCB as the main power source. Each solar cell is a hobby-grade 2 x 4 cm unit with a peak power output of 0.484 V at 250-275 mA. A 3.6 V Li-Ion battery is included too, which can be charged with the solar array. The EPS subsystem also includes a DC-DC converter that generates a 3.3 V regulated voltage. Another interesting feature is that telemetry is provided, in particular the current and voltage of solar cells, battery and 3.3 V regulated voltage are monitored.

The PCBSat is controlled by an 8-bit Atmel Mega128 AVR microcontroller, powered by the 3.3 V regulated line.

As Communication Subsystem, the PCBSat initially used the Atmel ATR2406 ISM Transceiver but its range was found to be less than 100 m and it required too many external components, leading to its replacement with the MaxStream XBee Pro module in the second revision [54]. The Pro version of the MaxStream XBee module provided improved efficiency and a declared range of approximately 1335 m. The authors also suggested the more expensive MaxStream XTend transceiver as an alternative, offering a range of 65 km and high RF efficiency.

Attitude Determination is achieved using two Cadmium Sulfide (CdS) sensors, one on top and one on the back of the PCB, that can detect which

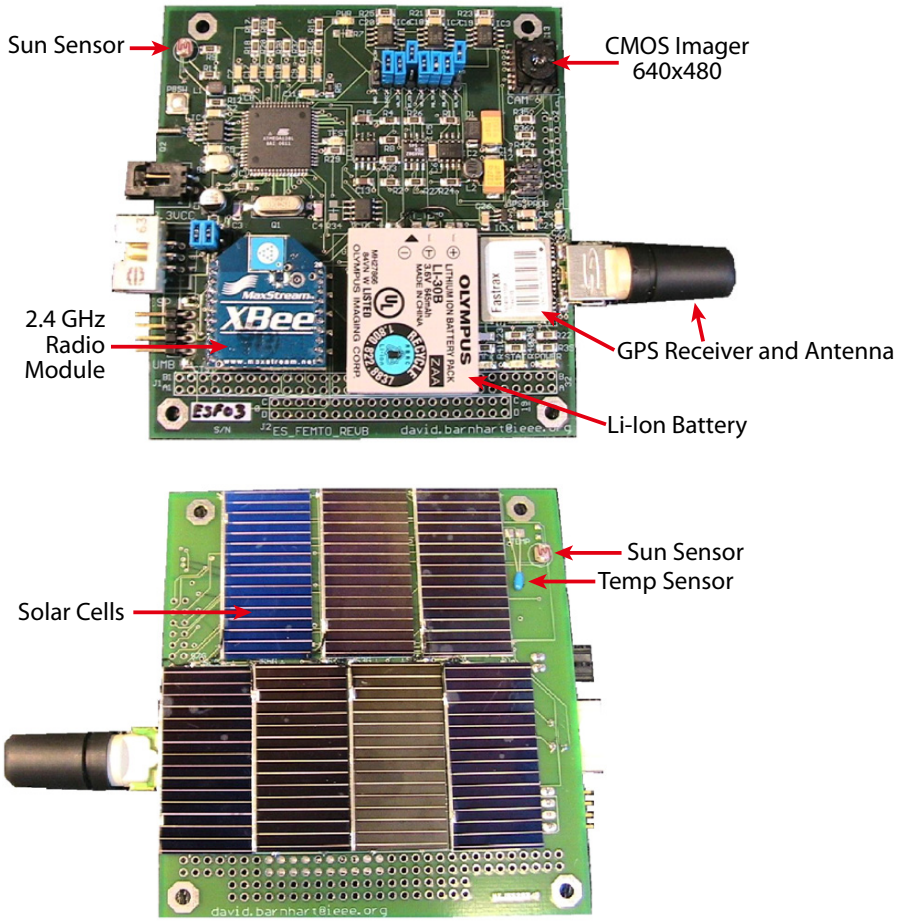

Figure 2.16: PCB Sat designed by Barnhart *et al.* [54].

surface is illuminated by the Sun. Attitude Control is achieved with a magnetorquer coil, driven by one of the microcontroller's PWM channels.

To determine the satellite's position, a Fastrax iTrax-03S GPS receiver (with antenna) was included. Accurate position information is crucial for data-collection missions, as it enables the correlation of data with specific locations [54]. The authors recall that terrestrial GPS receiver firmware are not suitable for space applications due to the high orbit velocity of about 7.5 km/s and require appropriate modifications.

The final PCBSat prototype depicted in Figure 2.16 weighed 70 grams, but the authors highlight the need to consider a proper space-qualified structure.

A notable aspect of the second spacecraft revision is that it was designed in order to allow independent testing of each subsystem while mounted on the PCB. Indeed, thorough testing was conducted after the integration phase

[54].

To the best knowledge of the author, despite its successful integration, this prototype has never flown.

2.2 Different Miniaturisation Approaches

The prototypes discussed in the previous section highlight the different approaches to miniaturization, each with its own advantages and disadvantages in terms of design and development cost, production cost, modularity, and integration density.

Barnhart *et al.* explored two distinct approaches in their designs: the SpaceChip, a Satellite-on-a-Chip utilising System-on-Chip (SoC) technology [51], and the PCBSat, a satellite-on-a-PCB integrated by soldering Surface Mounted Devices (SMD) onto a PC104 Printed Circuit Board (PCB) [54].

The PCBSat, as the name suggests, follows a PCB approach, where individual Integrated Circuits (ICs) and discrete electrical components are soldered onto a PCB board (Figure 2.17).

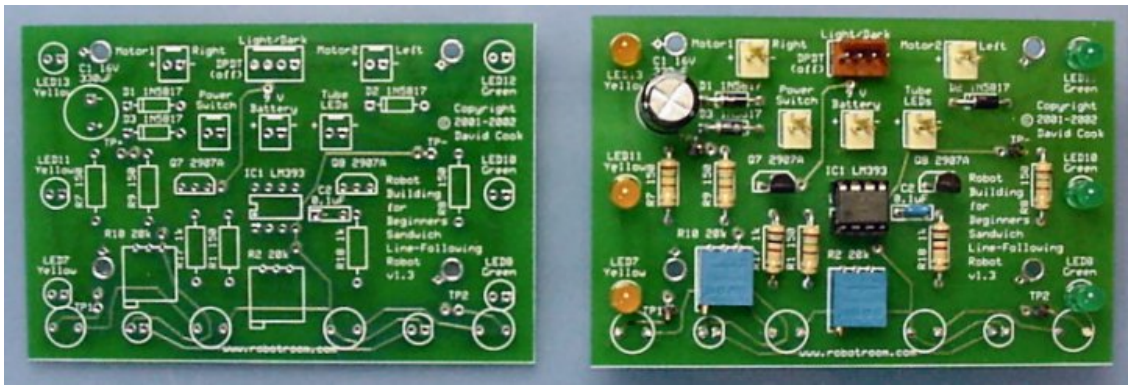

Figure 2.17: A Printed Circuit Board (PCB), unstuffed (left) and stuffed (right) [55].

This approach, also known as Breadboard Approach [56], allows for modularity, as components can be easily interchanged, especially during prototyping, and it is cost-effective since Commercial Off-the-Shelf (COTS) components can be readily purchased *off-the-shelf*. Moreover, this approach does not typically require an industrial production process, as components can be manually mounted and soldered. However, the PCB approach does not achieve high component density, the miniaturisation level is limited by the

components size resulting in bulkier prototypes with higher power consumption compared to other approaches.

It's worth noting that the PCB approach itself can vary in terms of integration density, ranging from the lower integration level of a breadboard (Figure 2.18) to the higher integration of a computer-designed PCB that is manufactured with industrial processes and later populated with components. The Sprite femtoSat [35] is an example of this latter PCB approach, where the spacecraft consists of a small PCB with SMD components soldered onto it. In the case of the Sprite Mission, which aims to launch a swarm of satellites, they were produced in large quantities to reduce unit cost.

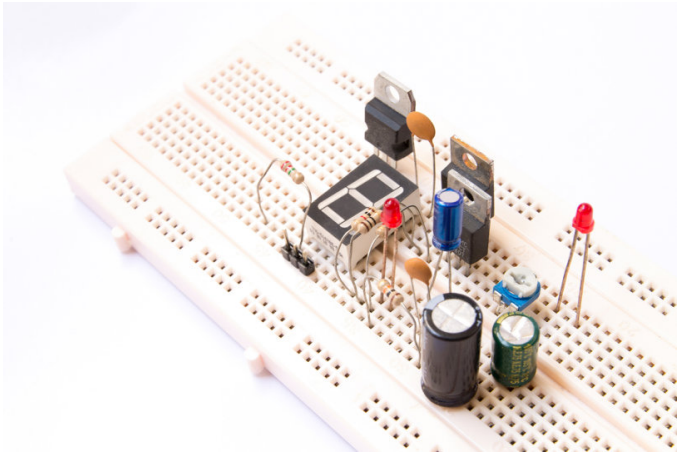

Figure 2.18: An example of breadboard with some discrete components.

Before discussing the SoC approach, which is the opposite of the PCB one, it is worth introducing the Multi-Chip-Module (MCM) technique [57].

MCM falls between PCB and SoC approaches, allowing for the integration of different ICs, Micro Electro-Mechanical Systems (MEMS), and other components on the same substrate. The key characteristic is that each integrated component is independently designed, manufactured, and tested, with all components eventually integrated to form the MCM module.

One MCM technique is 2D Integration, where ICs and MEMS are integrated side-by-side on the same package and connected by wiring techniques such as wire bonding or flip-chip bonding (Figure 2.19). The former consists in a chip-to-chip or chip-to-package interconnection by means of metal wires, the latter employs solder balls which double as electrical connection and physical chip attachment on the substrate.

The MCM approach offers some modularity and flexibility, as the individual MEMS and IC components are discrete and can be fabricated using

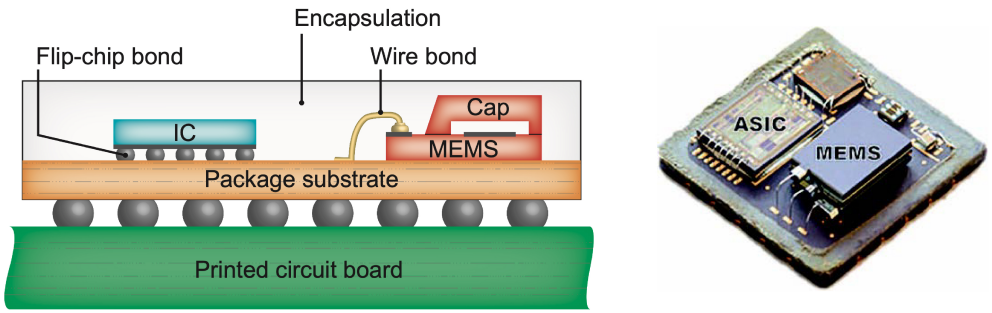

Figure 2.19: Multi Chip Module (MCM) 2D Integration. On the right a photograph of a decapsulated Colyibrys MS9000-series accelerometer where ASIC, passive chips and MEMS are placed side-by-side and wire bonded [57].

various techniques. However, it requires (low complexity) industrial fabrication processes for integration, increasing the final product cost compared to the PCB approach while ensuring an higher integration level and typically exhibit lower power consumption.

In addition to 2D Integration, there are 3D Integration processes, also known as System-in-Package (SiP) or Vertical MCM, which involve stacking and connecting ICs and/or MEMS components on top of each other (Figure 2.20). This approach reduces the package footprint compared to 2D side-by-side integration and enables shorter signal paths [57].

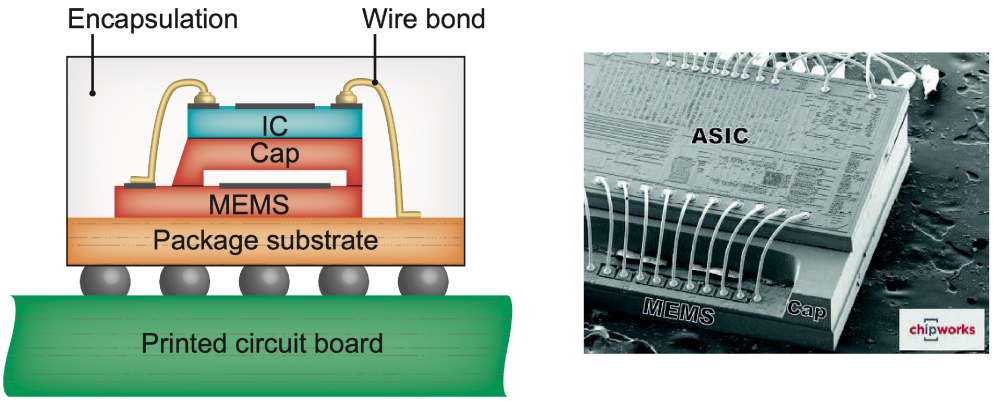

Figure 2.20: Multi Chip Module (MCM) System-in-Package (SiP) 3D Integration with Wire Bonding. On the right a Scanning Electron Microscope (SEM) image of a decapsulated ST Microelectronics 3-axis Accelerometer: the Application Specific Integrated Circuit (ASIC) is stacked over a MEMS Chip and interconnection is performed with Wire Bonding [57].

Another level of MCM integration is the Chip-Scale Package (CSP), typically used for face-to-face connection between a MEMS device and its driving IC through flip-chip bonding (Figure 2.21).

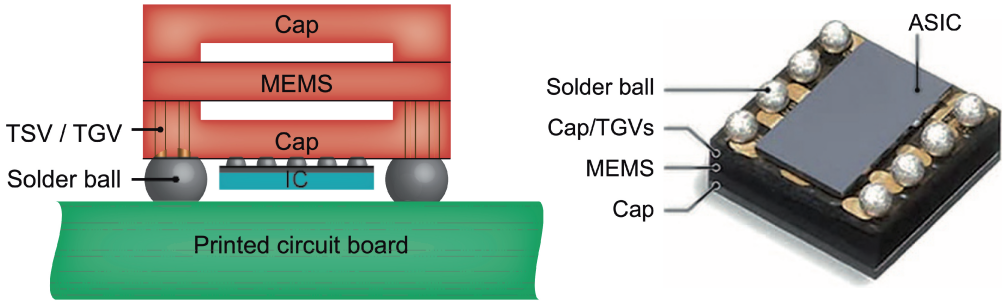

Figure 2.21: Multi chip Module (MCM) Chip-Scale Package (CSP). On the right a photograph of an accelerometer fabricated with Chip-on-MEMS technology [57].

Finally, the SoC approach integrates MEMS and ICs on the same substrate [57]. Fabrication processes are more complex compared to those required for an MCM module, and the design and development phase necessitates extensive expertise in the field.

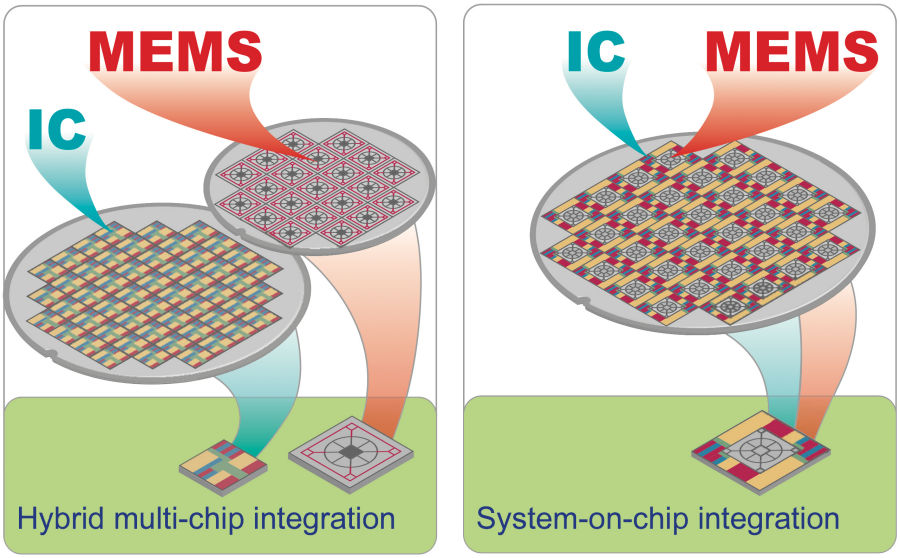

Figure 2.22: Multi Chip Module (left) and System-on-Chip (right) Integration Processes [57].

Modularity and flexibility are reduced in the SoC approach, as changing a

component may require significant design modifications. However, the final SoC component offers high integration density, a very small footprint, and reduced thickness.

Moreover, unlike the multiple tests performed on each component of an MCM or PCB prototype, testing an SoC product requires only one test at the end of production.

Numerous ways exist to integrate MEMS and IC components but, overall, two distinct approaches can be considered: monolithic and heterogeneous.

In monolithic SoC production, MEMS and ICs are directly integrated on the same substrate. Different integration processes are possible, differing in the order with which MEMS and IC components are integrated: MEMS-first processing, interleaved MEMS and IC processing, MEMS-last processing via bulk micromachining of the IC substrate (sometimes referred to as CMOS-MEMS), and MEMS-last processing via layer deposition and surface micromachining [57].

For heterogeneous SoC production, MEMS and ICs are initially fabricated on separate substrates and subsequently merged onto a single substrate using techniques like wafer bonding or similar transfer methods [57].

Table 2.1 shows concisely the miniaturisation approach adopted by each of the femtoSatellite prototypes discussed in Chapter 2.1.

Prototype	Miniaturisation Approach
Sprite by Zachary Manchester [35]	Printed Circuit Board (PCB)
Monarch by Adams and Peck [20]	Printed Circuit Board (PCB)
SpaceChip by Barnhart *et al.* [51]	System-on-Chip (SoC)
PCB Sat by Barnhart *et al.* [54]	Printed Circuit Board (PCB)

Table 2.1: Miniaturisation Approach adopted by each femtoSatellite Prototype discussed in Chapter 2.1.

Chapter 3

Satellite Subsystems

This chapter presents a coincise introduction to the main satellite subsystems. Innovative solutions will be explored, both in literature and the market, with particular focus on technologies for small satellites.

3.1 Electric Power System (EPS)

The Electric Power System is typically subdivided in the Power Generation Subsystem, responsible of generating power on board of the spacecraft, and the Power Storage Subsystem, which is responsible of storing the produced energy.

3.1.1 Power Generation

Power on board spacecraft is mostly generated with solar panels, with approximately 90% of nanosatellites equipped with solar cells for power generation as of 2021 [58]

It is not rare that small satellites include a deployable set of solar panels in order to generate more power. Such a deployable mechanism must be properly designed and it typically increases the design complexity as well as the overall system risk.

Solar cells are typically made of Group III-V semiconductor materials that convert sunlight into electricity through the photovoltaic effect. Common semiconductor materials used include Gallium Arsenide (GaAs) and Silicon (Si). Another important characteristic of solar cells is the number of junctions, i.e. the number of semiconductor layers that constitute the solar cell. Single-junction cells are the simplest, being constituted by just one

layer of material; multi-junction cells exist and include multiple layers, typically 3 to 5, triple-junction cells are the most common. Different materials absorb different wavelengths, this is the reason why multiple-junctions are more efficient with respect to single-junctions, because each layer is made of a different material allowing for the absorption and conversion of different portions of the light spectrum. This results in a larger portion of sunlight being converted into electricity. The theoretical maximum efficiency for a single-junction solar cell is 33.16% (known as the Shockley-Queisser limit) [59], while an infinite-junction solar cell would theoretically have a maximum efficiency of 86.6% [60]. Terrestrial silicon-based solar cells typically have an efficiency around 20%, while satellites often incorporate multiple-junction solar cells with higher costs but efficiencies that can reach up to 32% [58].

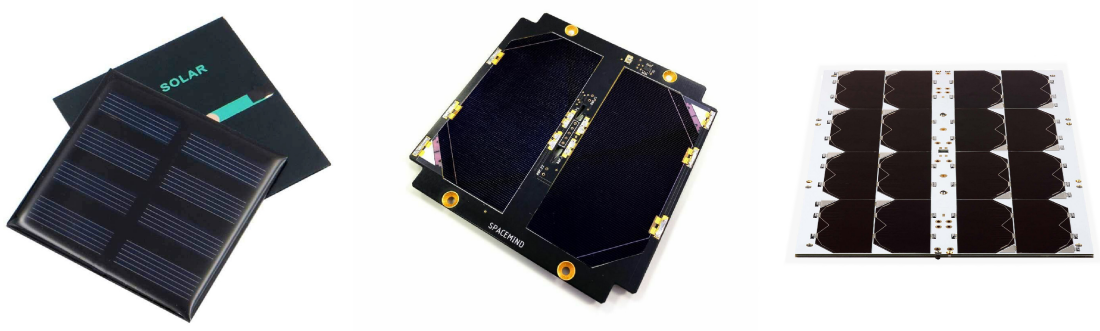

Figure 3.1: An hobbyist Polycrystalline Silicon Solar Panel Encapsulated in Waterproof Resin with 18% efficiency (left). A SP1Z solar panel by NPC Spacemind constituted by two series connected triple junction (InGaP/InGaAs/Ge) solar cells with 28% efficiency (center). A NanoAvionics GaAs solar array made of high-performance triple junction (GaInP/GaInAs/Ge) space grade solar cells with up to 29.5% efficiency (right).

Solar Cells also come with some limitations: being based on the photovoltaic effect, they require sunlight, therefore they cannot generate power while on eclipse and, less efficiency is typically observed in deep-space. Solar cells are also subject to performance degradation cause of different factors such as aging, radiation exposure and coverglass darkening. Indeed, one of the most important parameters that a designer should take into account while choosing a solar panel is their Beginning-of-Life (BOL) and End-of-Life (EOL) performances.

Innovative solutions for solar cells include multiple-junctions, up to 6, in

order to increase efficiency: Fraunhofer Institute for Solar Energy Systems has developed four-junction solar cells with an efficiency up to 38% (laboratory tested), while SpectroLab is experimenting 5- and 6-junction cells with a theoretical efficiency of 70% [58][61].

3.1.2 Power Storage

One limitation of solar cells is their dependence on sunlight for power generation, which means that a satellite relying solely on solar panels would not work in eclipse. To address this, energy storage devices are typically included in spacecraft.

Batteries are the most common method of energy storage and can be categorised as primary- or secondary-type. Primary batteries are non-rechargeable and are typically used for short-duration missions, while secondary batteries are rechargeable and the most employed for energy storage [58].

Batteries vary in chemistry, which influences their specific power density and specific energy density. High Power cells are designed in such a way to have low resistance thus allowing an higher discharge rate while high-energy cells optimise energy density to store as much energy as possible. However, high energy density batteries trades high capacity for a reduced cyclability, which is the number of recharge cycles a battery can undergo before degradation.

In space applications, batteries often underperform in terms of energy density because they need to function reliably for long-duration missions (5-15 years), prioritising cyclability over energy density.

Common secondary batteries used in space applications include Nickel-Cadmium (NiCd), Nickel-Hydrogen (NiH_2), Lithium Polymer (LiPo), and Lithium-Ion (Li-Ion). To date, Li-Ion cells can achieve specific energy densities of 270 Wh/kg [58] with an average voltage of 3.6 V and specific power densities of 250-340 W/kg. They also offer high rechargeability and, being lightweight, they are prevalent in portable electronic devices.

In terms of form factor, the cylindrical 18650 (18 x 65 mm) cells are commonly used for small satellites (Figure 3.2) [58].

An advantage of batteries is that, differently from electronics, they are not affected by radiation. However, aging due to charge and discharge cycles is a significant limitation. Factors such as temperature, charge/discharge rate, depth of discharge, and storage conditions can impact battery aging [58].

Regarding future energy storage developments, research is focused on finding new chemical compositions and materials to improve battery capacity,

Figure 3.2: A 18650 Li-Ion Battery Cell from Samsung (left) and the NanoPower BP4 Battery Module from GomSpace (Denmark) which includes four 18650 Battery Cells.

energy density, and power density.

Supercapacitors, also known as Electric Double-Layer Capacitors (EDLCs) or Ultracapacitors (Figure 3.3), are intriguing devices for energy storage subsystems. Unlike batteries that store energy chemically, EDLCs store charges electrostatically. This is the key difference that distinguish batteries from supercapacitors and that define the unique electrical characteristics of a supercap.

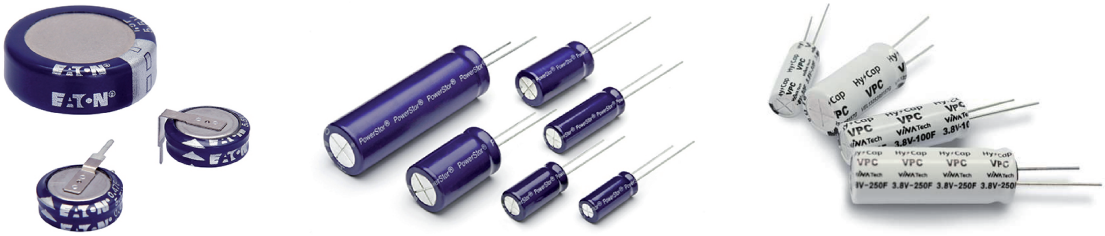

Figure 3.3: Eaton KR and KVR Families of Supercapacitors, thought to replace button cell batteries (left). Eaton HB family of Supercapacitors used as standalone energy storage or in combination with batteries (center). VINATech VPC Series 3.8 Volt Hybrid Capacitor (right).

Supercapacitors exhibit very high power densities, up to 100 kW/kg, but low energy densities, up to 7 Wh/kg [58]. The high power density makes them suitable for applications requiring power transients. EDLCs also offer better thermal management due to their lower internal resistance (an order of magnitude lower compared to batteries) which results in less wasted energy

in the form of heat. This mitigates concerns about thermal runaways that require batteries to incorporate temperature monitoring mechanisms to avoid explosions. Supercapacitors, instead, maintain stable performance over a wide range of operating temperatures (-40°C to +70°C). Moreover, they can withstand millions of charge/discharge cycles, making them more durable and efficient than batteries.

Batteries and supercapacitors possess complementary characteristics, leading to their combination in Hybrid Energy Storage Systems (HESS) to harness the advantages of both technologies [62].

Hybrid Supercapacitors (Figure 3.3), instead, integrate battery and supercapacitor technologies in a single device. They are built by replacing one of the carbon-based electrodes with a lithium-doped carbon electrode (similar to the one of Lithium-Ion Batteries), increasing the operating voltage to 3.8 V (compared to the maximum 3.0 V rating for EDLCs), along with an increase in capacitance. Hybrid Supercapacitors also offer lower self-discharge and leakage current, high power densities, and long life cycles [62].

Regarding miniaturization, Li-Ion batteries are available in various form factors and capacities from different manufacturers (Figure 3.4). Other solutions are lithium coin-type 3.3 V batteries which can be combined with solar panels to create a hybrid power supply (Figure 3.4).

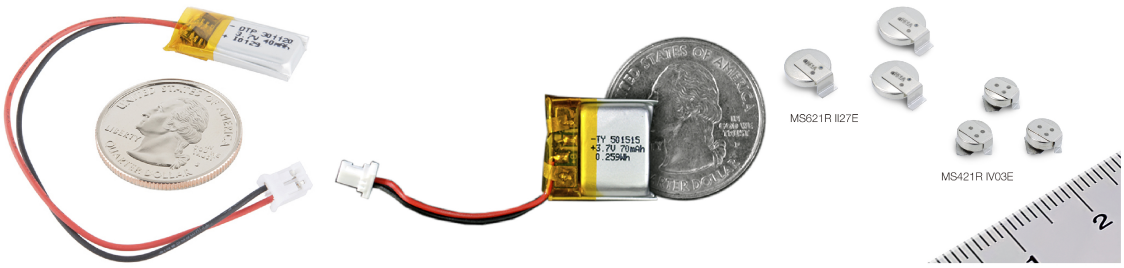

Figure 3.4: COTS Li-Ion Batteries: 20 x 11 x 3 mm, 40 mAh by Datapower (left), 15 x 15 x 5 mm, 70 mAh by TinyCircuits (center), MS621R coin-type batteries, 3.3 V, 3.0 mAh, 6.8 x 2.1 mm by Seiko Instruments (right).

It is important to note that none of these technologies have been flown in space, to the author's knowledge. Therefore, thorough testing is necessary before considering them as viable options for space applications. However, the small form factors of these energy storage solutions hold promise for miniaturization and for providing power storage in very small satellites.

3.2 On Board Data Handling (OBDH)

The On-Board Data Handling (OBDH) Subsystem, also known as the On-Board Computer (OBC), serves as the central processing unit and control center of a spacecraft. It manages the computing and processing tasks and takes charge of controlling and commanding all the other subsystems while handling the telemetry and data they provide [58].

Safety is a critical aspect of spacecraft operations, and the OBC plays a crucial role in ensuring the spacecraft's well-being. As a result, autonomous failure management functionalities are typically incorporated into the OBC to enable autonomous recovery from anomalies and enter into a safe state without interaction from the ground operators [63].

The heart of an OBC is a microprocessor, which, being an electronic component is susceptible to the radiations typical of space environments. To mitigate this, being microcontrollers essential to the spacecraft's core functionality, they must be designed inherently immune or tolerant to radiation or must be hardened against it.

Furthermore, as the primary control unit of a spacecraft, traditional, costly spacecraft often incorporate redundancy to prevent mission failures. However, smaller spacecraft face limitations in terms of size, volume, and weight, making it challenging to include redundant components.

In terms of performance, most of the current microprocessors can easily handle the processing requirements of most OBDH subsystems [58]. However, space-qualified microcontrollers, designed to meet stringent radiation hardening requirements, generally lag in terms of performance behind their Commercial Off-the-Shelf (COTS) counterparts which, unfortunately, need to be adequately hardened against radiation before being included in a spacecraft design.

Another essential component of the OBDH subsystem is mass memory. Since it is not always possible to download data to the ground station, the spacecraft may need to temporarily store payload and telemetry data. Solid-state mass memories such as flash memories or Dynamic RAMs are commonly used solutions for this purpose [63].

Regarding miniaturisation, various commercial vendors offer highly integrated solutions that include the On-Board Computer, mass memory, electric power systems, and input/output (I/O) interfaces. As discussed in Chapter 2.2 about Miniaturization Approaches, integration can occur at the module level on the same Printed Circuit Board (PCB) or through small, highly integrated Commercial Off-the-Shelf (COTS) Systems-on-Chip (SoC). These

SoCs, packaged in small sizes, incorporate a microprocessor, memory, and I/O interfaces on the same package. An example of such integration is seen in the Sprites developed by Zachary Manchester, as mentioned in Chapter 2. The Sprites employ a CC430 System-on-Chip (SoC) by Texas Instruments, which includes an MSP430 microcontroller for computing capabilities and the CC1101 UHF transceiver for communication [3].

Modern microcontrollers also enable software-defined architectures, for example software-defined radios (SDR). These architectures offer flexible solutions that allow for software updates and modifications to be performed while the satellite is on orbit. This adaptability enables missions to be adjusted to changing conditions or changed requirements.

3.3 Attitude and Orbit Determination and Control (AODC)

The Attitude and Orbit Determination and Control (AODC) subsystem is responsible for managing the attitude and orbit of a spacecraft.

Attitude control plays a crucial role in spacecraft operations by ensuring the stabilisation of the satellite and its orientation in a desired direction. This capability is essential for various reasons, including the precise pointing of the payload, alignment of solar arrays for efficient power generation, and the optimal positioning of the RF antenna to facilitate communication with ground stations on Earth or other spacecraft in space.

Various sensors are typically used to determine the absolute attitude of the spacecraft by utilising external references. These sensors are star trackers, solar sensors, or magnetometers which enable the spacecraft to determine its orientation based on the stars, the sun, or the Earth's magnetic field, respectively.

Inertial sensors are also employed, providing a short-term attitude reference between updates of non-inertial sensors. They are used to propagate the vehicle attitude between measurements from non-inertial sensors [58][64].

Actuators, such as magnetorquers, reaction wheels, control moment gyroscopes or thrusters are capable of exerting forces or torques on the spacecraft and permit the AODC subsystem to point the satellite in a desired orientation and maintain it despite any external disturbance.

3.3.1 Attitude Control

Attitude control is achieved through the use of different actuators which basically exploit the conservation of angular momentum. The most common types of attitude control actuators include reaction wheels, momentum wheels, control moment gyroscopes, and magnetorquers. Thrusters can be used for attitude control too but, differently from the previous electric actuators, they require propellant.

Reaction wheels and momentum wheels are essentially the same kind of actuator, they are known as momentum exchange devices and consist in a electric motor coupled with a flywheel.

Reaction wheels are also known as zero-momentum systems [64] because they respond to external disturbances by adjusting their rotational speed, which can initially be zero. When an external disturbance acts on the spacecraft, the speed is increased or decreased depending on the direction of the disturbance. Indeed, according to the 3rd Newton Law, if the wheel is accelerated (or decelerated) a torque is applied on the spacecraft and, due to the conservation of angular momentum, the spacecraft will accelerate on the opposite direction. However, there is a limit to how fast a reaction wheel can rotate, and it saturates when the maximum speed is reached. A saturated wheel cannot further compensate for disturbances that act in the same direction of rotation. Therefore, in such cases, other actuators such as thrusters or magnetorquers must be employed to desaturate the reaction wheel and return its speed to zero.

Momentum wheels, also known as momentum-bias systems, are similar to reaction wheels. However, momentum wheels operate at a constant angular velocity different from zero thus providing gyroscopic stiffness to the spacecraft, which means they inherently resist external disturbances and offer stability about their spin axis. In order to control the spacecraft's attitude about the momentum wheel rotation axis, the speed of the wheel can be slightly increased or decreased.

A full three-axis control system requires three wheels mounted orthogonally. In some cases, a four-wheel configuration is used to provide fault tolerance (Figure 3.5). In this configuration, the wheels are mounted in a skewed or angled manner, leading to cross-coupling of torques between two or more wheels [58]. Although this reduces the torque capability along each individual axis, it provides redundancy in case of failure of one of the wheels.

Another actuator used for attitude control is the Control Moment Gyroscope (CMG). It consists of a reaction/momentum wheel mounted on a

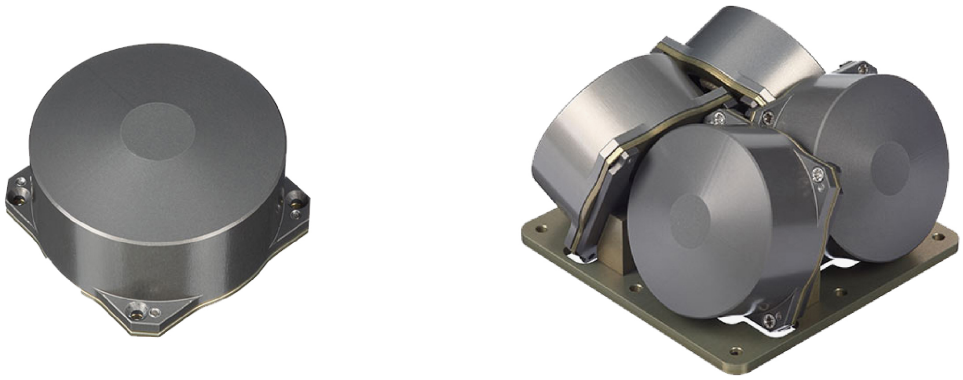

Figure 3.5: SatBus 4RW0 Reaction Wheels Control System for CubeSats by NanoAvionics, which incorporates four reaction wheels arranged in a skewed configuration to provide redundancy.

gimbal, making it a more complex system but capable of generating more torque for a given weight and power compared to other actuators.

Magnetic torquers, also known as magnetorquers, are another type of actuator employed for attitude control. These devices create a local magnetic field that interacts with an external magnetic field, typically the Earth's magnetic field. This interaction generates a torque that can be used to control the spacecraft's attitude. As previously mentioned, magnetorquers are also commonly used for desaturating reaction wheels (Figure 3.6).

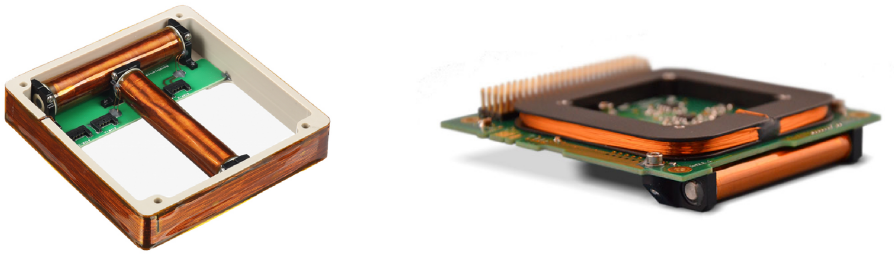

Figure 3.6: Two magnetorquers suitable for detumbling and attitude control, composed of two torque rods (X and Y-axis) and one air core (Z-axis): SatBus MTQ Magnetorquer by NanoAvionics (left) and iMTQ Magnetorquer by ISISPACE (right).

When it comes to miniaturization of these devices, being them basically electric motors with a flywheel, there are many different miniature motors

available on the market that could be suitable for integration into a femtoSatellite. Figure 3.7 shows two small brushless motors from Faulhaber. The 0206 B, although no longer available, had dimensions of 1.9 x 5.5 mm and weighed just 0.09 grams. It had a maximum speed of 100.000 rpm, a rotor inertia of 0.00007 gcm^2, and can be operated over a wide temperature range of -30°C to +125°C. The 0308 B, which is currently available for purchase, has dimensions of 3 x 8.3 mm, weighs only 0.35 grams, has a maximum speed of 96.000 rpm, and a rotor inertia of 0.0002 gcm^2.

Another solution is offered by Maxon, the ECX SPEED 4 M Brushless Ironless Winding MicroMotor (Figure 3.7). This micro motor weighs just 1 gram and has a diameter of 4 mm and a length of 20 mm. It offers a maximum speed of 35.000 rpm and a rotor inertia of 0.00111 gcm^2.

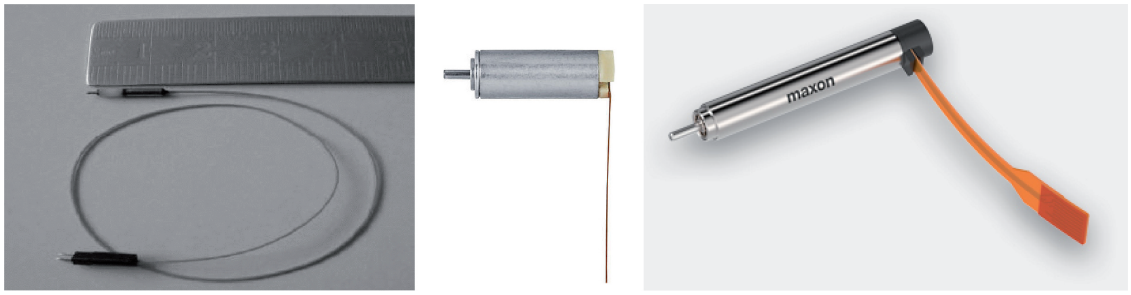

Figure 3.7: Faulhaber Brushless DC Micromotors: Series 0206 B, 1.9 x 5.5 mm, 0.09 grams (left) and Series 0308 B, 3 x 8.3 mm, 0.35 grams (center). Maxon ECX SPEED 4 M Brushless, Ironless Winding MicroMotor, 4 x 19 mm, 1 gram (right).

While the Faulhaber and Maxon motors cost hundreds of euros, there are cheaper alternatives available on the market. For example, the 3.2 x 8 mm DC Coreless Motor from NFP Electronics, priced just $ 5, is one of the smallest available on the market (Figure 3.8).

These motors are not space-qualified, and modifications would likely be required to include a flywheel in order to increase their inertia. However, the high speed that they can reach may be sufficient for attitude control in a very small spacecraft even without a flywheel.

Other interesting solutions for miniaturization are flat motors, as shown in Figure 3.10. The Faulhaber 1202 BH, which is no longer available, was a flat motor produced using photolithography. It weighed 1.1 grams, had a diameter of 12 mm, and a height of just 2 mm. It had a maximum speed of 40.000 rpm and a rotor inertia of 0.125 gcm^2. Faulhaber currently offers two alternatives, although they are bulkier: the 1506 SR brushed flat micromotor

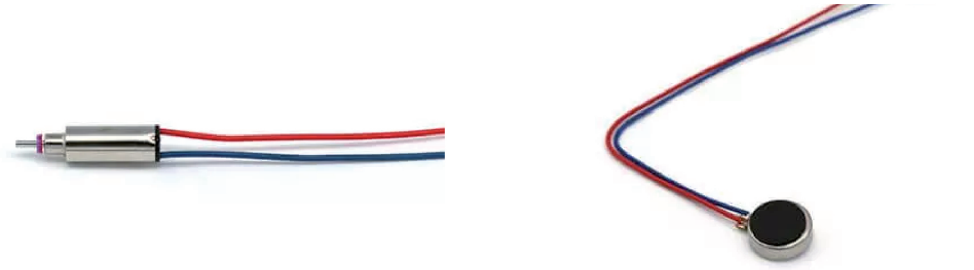

Figure 3.8: 3.2 x 8.1 mm Coreless DC Motor (left) and 7 x 2 mm Coin Vibration Motor offered by NFP Electronics.

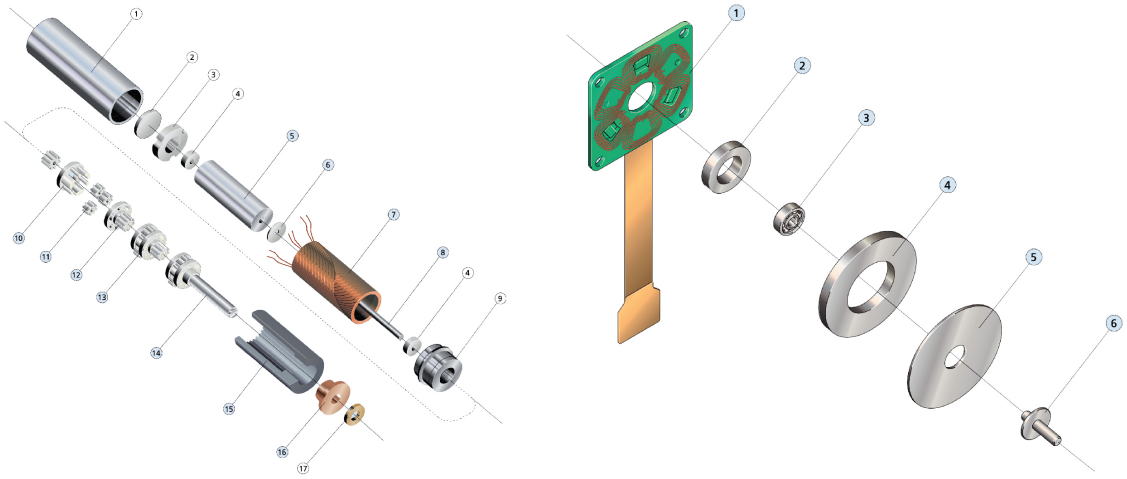

Figure 3.9: Exploded-view Drawing of Faulhaber Series 0206 B (left) and Series 1202 BH (right).

that weighs 4.3 grams and has a diameter of 15 mm and a height of 5.5 mm. It has a maximum speed of 16.000 rpm and a rotor inertia of 0.08 gcm^2. The 1509 B brushless flat micromotor weighs 6.9 grams, has a diameter of 15 mm, a height of 8.8 mm, a maximum speed of 40.000 rpm, and a rotor inertia of 0.69 gcm^2.

In terms of flat motors, another possibility proposed in [56] is COTS phone vibration motors, also known as button-type motors, which can provide a torque of approximately $2 \cdot 10^{-5}$ Nm (Figure 3.8).

Lastly, Astrofein High-Precision Aerospace Technology offers the RW1 Reaction Wheel, which is a ready-to-fly reaction wheel available in two versions with different inner rotating mass weights, leading to different angular momentum capabilities. Both versions have the same dimensions of 21 x 12 x

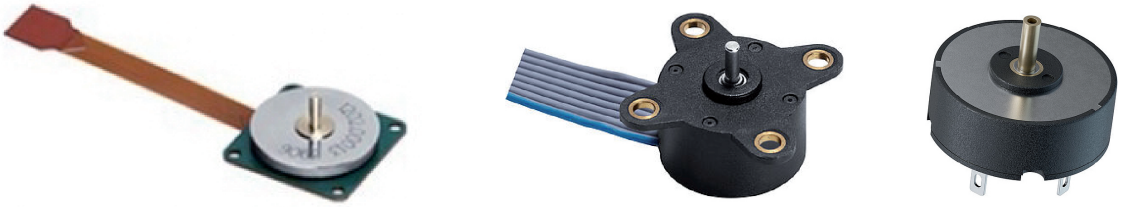

Figure 3.10: Faulhaber Brushless DC Flat Micromotor, Series 1202 BH (left), Faulhaber Brushless Flat DC Micromotor, Series 1509 B (center), Faulhaber Brushed Flat Micromotor, Series 1506 SR (right).

21 mm and are designed for a one-year lifetime in Low Earth Orbit (Figure 3.11).

Figure 3.11: Astrofein RW1 Reaction Wheel. Size: 21 x 12 x 21 mm. Weight: 24 g (or 15 g).

MEMS reaction wheels are also an attractive option, however custom-fabricated monolithic wheels provide very little torque in the order of 10^{-9} - 10^{-10} Nm [56].

Micro Electro-Mechanical Control Moment Gyroscopes

Miniaturization efforts in the field of attitude control have led to the development of innovative solutions using Micro Electro-Mechanical Systems (MEMS) technology. These MEMS-based actuators offer compact size, low power consumption, and potential cost-effectiveness, making them suitable for small satellite applications.

One notable MEMS-based solution is the MEMS Control Moment Gyroscope (CMG) proposed by Chang *et al.* [65]. This CMG consists of two orthogonal angular vibration systems, namely the rotor and the gimbal, which

generate an output torque perpendicular to their vibration axes through the Coriolis effect.

The final design, which incorporates four MEMS CMGs controlled with a phase shift of $\pi/2$ between every two units, has a size of 1.1 x 1.1 x 0.04 cm and weighs only 0.1 grams (Figure 3.12). The maximum output torque achievable with this configuration is estimated to be $5 \cdot 10^{-8}$ Nm.

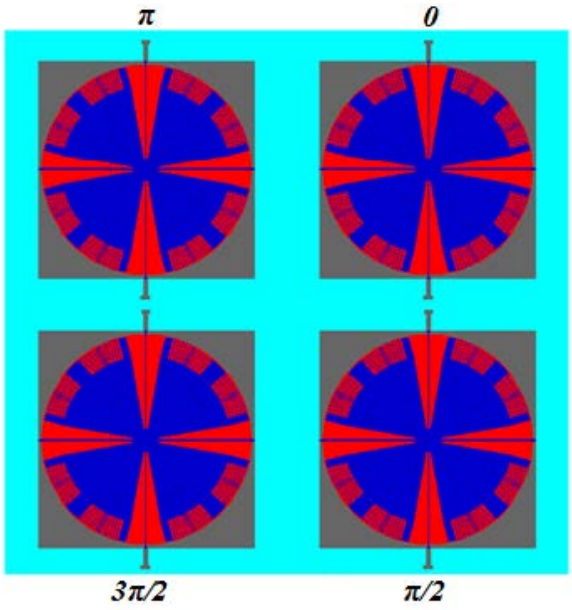

Figure 3.12: The Array Configuration with four MCMGs as an element [65].

The four MCMGs configuration helps cancelling out parasitic torques and ensures a stable and constant output torque. Indeed, when a single MCMG operates, it generates a parasitic torque due to the change in gimbal momentum. However, this parasitic torque can be effectively canceled out by considering two MCMGs with opposite phases [65]. Moreover, being the MCMG based on vibrations, the total torque, despite being positive, fluctuates and follows a sine wave. In order to have a constant output torque, two MCMGs $\pi/2$ out of phase are needed, as we can see with the following computation [65].

The output torque of a single MCMG is:

$$T_1 = A\cos^2 \omega t \qquad \text{and} \qquad T_2 = A\cos^2(\omega t + \pi/2). \tag{3.1}$$

By summing the torques of two MCMGs $\pi/2$ out of phase, we obtain:

$$T_1 + T_2 = A\cos^2 \omega t + A\cos^2(\omega t + \pi/2) = A, \tag{3.2}$$

where $A = I(2\pi f)^2 A_r A_g$. A_r and A_g are the angular vibration amplitudes of the rotor and the gimbal, respectively, and f is the resonant frequency of the rotor and the gimbal.

The maximum output torque produced by a single MCMG with a gimbal and rotor angular displacements of $A_g = 0.87°$ and $A_r = 0.06°$, a resonant frequency of $f = 1$ kHz was computed to be $2.5 \cdot 10^{-8}$ Nm [65].

To further increase the torque, the resonant frequency f can be increased to 10 kHz. Being the torque proportional to the square of the frequency, this results in a significant boost in the torque magnitude. With a resonant frequency of 10 kHz, the final maximum output torque achievable for a single MCMG is estimated to be on the order of 10^{-6} Nm. Considering the four MCMG configuration, the maximum output torque that can be obtained is on the order of $5 \cdot 10^{-8}$ Nm [65].

This MEMS CMG offers several advantages over traditional actuators. By utilising angular sinusoidal vibrations instead of rotational movements, it eliminates issues related to bearing friction and breakdown that are common in wheel-based actuators. The rotor consists of in-plane rotary electrostatic comb drives and it is suspended by four clamped straight beams. The gimbal is supported by two beams anchored on the substrate and it is driven by electrostatic parallel plate actuators (Figure 3.13).

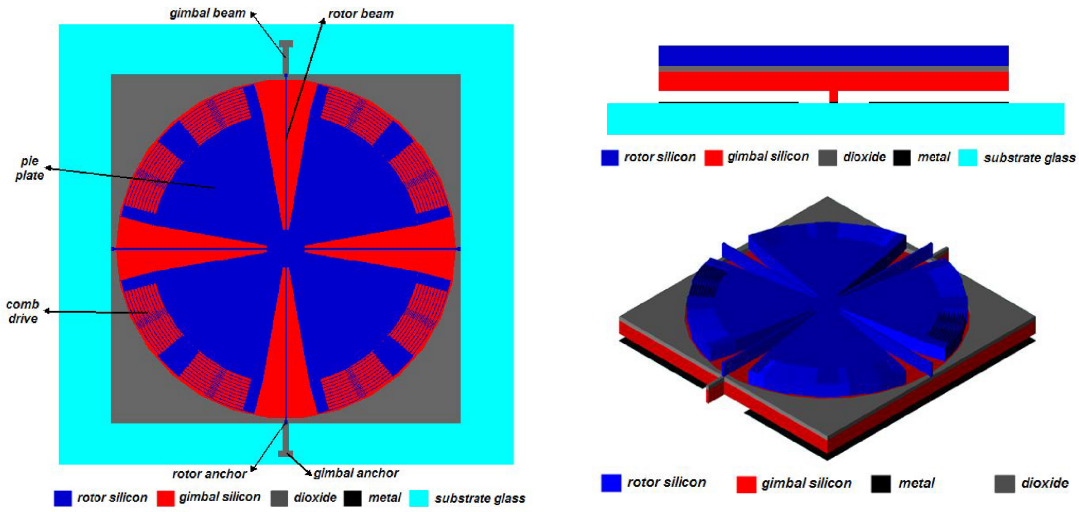

Figure 3.13: MCMG Structure. Top view on the left, where the comb drives, responsible of the rotational movement, and the suspension beams can be seen. On the top right the parallel plate actuators, responsible of the gimbal movement. On the bottom right a 3D model of the MCMG [65].

Another version of MEMS CMG was proposed by Post *et al.* [66]. This design features a single device layer and is based on rotational oscillation of a disk which is coupled to a frame that provide the tilt oscillation about its main axis (Figure 3.14).

The combined movements of rotation and tilt, achieved through capacitive electrostatic comb-drive actuation, generate a resulting torque in a single direction. Comb-drives actuation offers a lower power consumption compared to other MEMS actuation mechanisms and a reduced risk of pull-in phenomena [66].

An electro-mechanical simulation using the Finite Element Modelling (FEM) COMSOL Multiphysics software estimated that a single CMG-MEMS device could produce a maximum torque of approximately $1.5{\cdot}10^{-6}$ Nm which is almost 2 orders of magnitude higher than the value estimated for the previous design [65]. This result has been obtained for an assumed rotation amplitude of 9° and a tilt amplitude of 10°. The difference in torque magnitude can be mainly attributed to the increase in the oscillation frequency. Indeed, the newer MEMS CMG design operates at a resonant frequency of 55 kHz which was obtained thanks to the FEM simulation. The mass moment of inertia J of the rotating part was calculated to be $4.7 \cdot 10^{-16}$ m^2·kg and the obtained resonant frequency f of both the rotation and tilt movements was indeed 55 kHz.

To fabricate the MCMG, a cost-effective and reliable multi-user single crystal silicon-on-insulator (SOI) process called SOIMUMPs, offered by Memscap Inc., would be employed. This process enables the production of a 9 x 9 mm chip capable of accommodating an array of 9-12 synchronised MEMS CMGs [66].

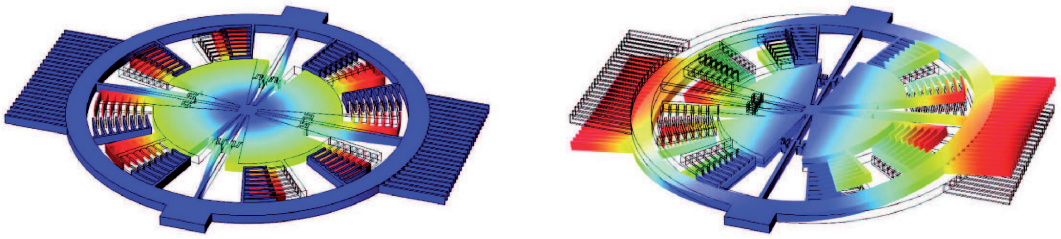

Figure 3.14: Electro-mechanical simulation of MCMG Tilt Movement (left) and Rotational Movement (right) [65].

These MEMS-based CMGs offer promising potential for attitude control in very small satellite missions. Their compact size and low power consumption

make them well-suited for applications where space and weight constraints are critical. Furthermore, the possibility to integrate these MEMS CMGs into a System-on-Chip (SoC), as discussed in Chapter 2.2, offers the possibility to create highly integrated devices that would thus combine communication and computation capabilities as well as attitude control. This advancement brings the concept of a Satellite-on-Chip closer to reality. However, further development, simulations, and testing of prototypes are necessary to validate their performance and reliability.

MEMS Rotary Actuators

Another interesting MEMS device is presented in [67] by Krygowski *et al.*. The authors propose a low voltage stepper motor which can be operated with less than 6 Volts. This MEMS motor poses as an evolution of an earlier prototype presented some years before.

The former prototype consisted of a stator made by stationary electrodes patterned around a conductive polysilicon rotor (Figure 3.15). The main drawback of this design was the low capacitance between rotor and stator electrodes which caused the final output torque to be low unless high voltages (tens to hundreds) were applied. Moreover high operating voltages were required cause of the large friction on the hub where the rotor is constrained to rotate.

The advancements in surface micromachining processes permitted to place several layers of mechanical polysilicon. In particular the Five Level Sandia Ultraplanar Multi-level MEMS Technology (SUMMiT-V) fabrication process was employed by Krygowski *et al.* in [67] in order to produce a newer MEMS micromotor which overcomes the drawbacks of the earlier design.

The five polysilicon layers allowed the fabrication of an ideal electrodes configuration which allows an higher capacitance between the rotor and stator electrodes as well as a low-play and low-friction hub.

In particular, two rotor electrodes were coupled to a stator element, opposed to the single rotor-stator pair of the earlier design. Moreover, several concentric rings of rotors and stators were used so that the capacitance was dramatically increased (Figure 3.16).

With these measures, the authors were able to demonstrate a fully functioning MEMS micromotor which could work with less than 6 Volts.

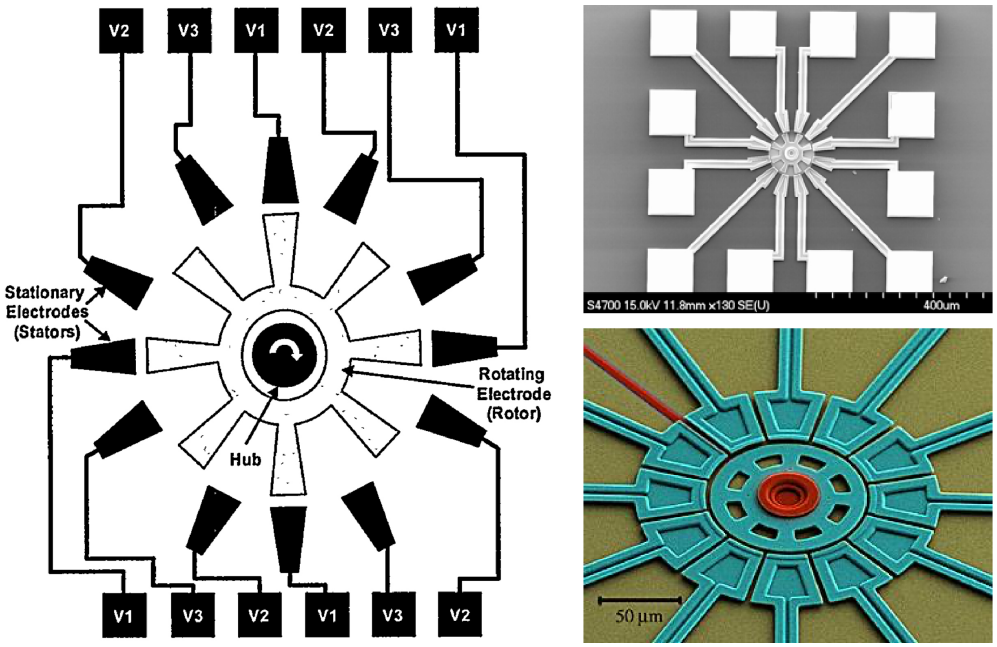

Figure 3.15: Schematic representation of the early side-drive electrostatic micromotor (left) [67]. Two Scanning Electron Micrograph (SEM) Photos of fabricated prototypes by MEMS and Nanotechnology Exchange (MNX): a surface micromachined electro-statically-actuated micromotor (top right) and a salient-pole electrostatically actuated micromotor made from polycrystalline silicon using surface micromachining techniques (bottom right) [68].

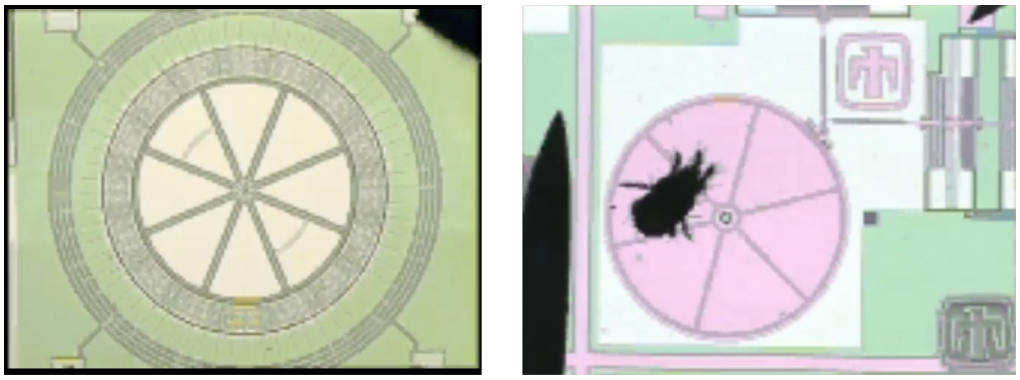

Figure 3.16: SEM Photos of the micromotor (left) and of the microengine that is moving a bigger gear with a bug on it (right) [69].

MEMS Microengine

Another MEMS rotary solution was proposed by Garcia and Sniegowski in [70].

The authors proposed a batch fabricated polysilicon microengine which exploits electrostatic comb-drives as linear actuators that are directly linked to an output gear allowing the conversion of linear motion into rotational motion.

In terms of size, the output is a 50 μm continuously rotating gear that can be in turn connected to another micro-mechanism.

The first arrangement included just one single batch of comb-drive actuators but it was not capable of delivering torque at 0° and 180°. As a solution the authors decided to introduce another array of comb-drives orthogonally placed with respect to the initial set and pilotated 90° out of phase so that a torque could be provided at any angle (Figure 3.17) [70].

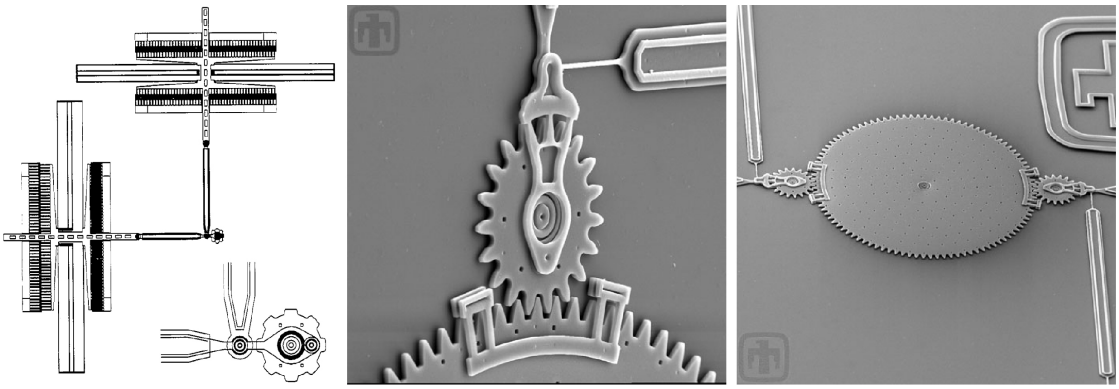

Figure 3.17: A schematic drawing of the microengine (left). SEM Photos of a gear (center) and of two small gears that rotate the large gear in the middle (right), provided by Sandia National Laboratories [69].

One challenge associated with MEMS electrostatic actuators is the need for a High-Voltage (HV) drive circuit. Each MEMS actuator has specific power supply requirements, ranging from just a few volts to up to 300 volts, while requiring a small activation current ranging from 1 μA to 5 mA. Currently, in order to simplify the manufacturing process of MCMGs, a separate semiconductor circuit is utilised to house the control electronics responsible for generating the control signals for the HV drive electronics. These HV drive electronics then provide power to the connected MEMS electrostatic load [66].

3.3.2 Attitude Determination

As mentioned earlier, there are various types of attitude sensors that rely on external references to determine the spacecraft's absolute attitude. These

sensors include star trackers, sun sensors, magnetometers, and inertial sensors.

Star trackers provide the absolute three-axis attitude of the spacecraft by comparing digital images captured by the sensor to an onboard star catalogue. Star trackers typically update the absolute attitude at a frequency of a few hertz.

Magnetometers determine the spacecraft's attitude by measuring the local magnetic field. They are usually packaged to provide three-axis attitude determination.

Sun sensors exploit the brightness of the sun to estimate its direction, which in turn provides information about the spacecraft's attitude.

Inertial sensors consist of gyroscopes, which measure angular changes, and accelerometers, which measure velocity changes. These sensors are often packaged together in an Inertial Measurement Unit (IMU), which typically includes three orthogonal gyroscopes, three orthogonal accelerometers, and sometimes a three-axis magnetometer. While IMUs do not provide absolute attitude measurements, they play a crucial role in estimating and propagating the spacecraft's attitude between absolute measurements. This is particularly valuable in scenarios where a precise knowledge of the attitude is required, as it helps bridge the gap between infrequent updates from non-inertial absolute attitude sensors [58].

3.3.3 Orbit Determination and Control

Being deployed in Low-Earth Orbits (LEO), most small satellites utilise onboard GPS receivers as a mature technology for orbit determination, replacing ground-based tracking methods [58].

Regarding Orbit Control, as of October 2020, O'Reilly *et al.* declare that traditional small satellites do not have enough Δv capabilities to transfer orbits or design safe de-orbit strategies [71]. Therefore, to date, small satellites are typically constrained to remain in their pre-selected LEO orbit.

Despite these limitations, there are interesting miniaturised propulsion systems in literature that can be employed for attitude control, as well as orbit keeping, collision avoidance and formation flight.

Propulsion systems can be classified into three main categories: Chemical, Electric, and Propellant-less.

Chemical propulsion systems are highly capable, reliable and characterised by high-thrust, allowing impulsive manoeuvres (Figure 3.18). However, they offer lower specific impulses, which translates in poor fuel efficiency, compared

to their electric propulsion counterparts.

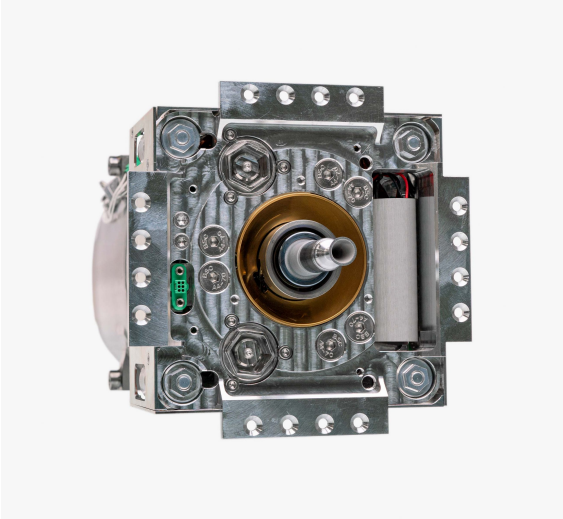

Figure 3.18: The Enabling Propulsion System for Small Satellites (EPSS) by NanoAvionics that uses the green ADN-based monopropellant.

The commonly used hydrazine monopropellant thrusters, known for their low mass and volume, have been extensively utilized for small corrective manoeuvres and attitude control on larger spacecraft. Therefore, they can be employed as the main propulsion system for small satellites [58].

However, concerns regarding the handling and toxicity of hydrazine have led to the exploration of alternative "green propellants" technologies.

"Green" ionic liquid propellants have reduced toxicity and significantly lower vapour pressures, compared to hydrazine. These propellants provide higher specific impulse performances and have an higher density-specific impulse achieving improved mass fractions [58].

Electric Propulsion (EP) is another class of propulsion systems that accelerate the propellant through the conversion of electrical energy into kinetic energy. The energy conversion occurs by one of three mechanisms: electrothermal, electrostatic, or electromagnetic acceleration.

EP systems offer higher impulse capabilities compared to chemical propulsion, making them more suitable for small satellites due to their higher specific impulse which implies higher fuel efficiency thus less fuel and propellant storage required.

However, having low thrust capabilities, the major challenge for electric propulsion approaches is the time required to reach high trust levels, often spanning hundreds or thousands of hours compared to the seconds or minutes

needed for chemical systems to achieve similar impulses [58][71].

A noteworthy example of Miniaturised Electric Propulsion System is the Scalable ion Electrospray Propulsion System (S-iEPS), which is fabricated using Micro Electro-Mechanical Systems (MEMS) processes [72].

Each S-iEPS unit consists of a 1 cm^3 propellant tank with passive propellant supply and 480 emitter tips on top (Figure 3.19). Ionic liquids used in the S-iEPS have negligible vapour pressure, eliminating the need for propellant pressurisation thus making capillarity passive feed system well suited for miniaturisation because it does not require hard-to-miniaturize components such as pressure valves [72].

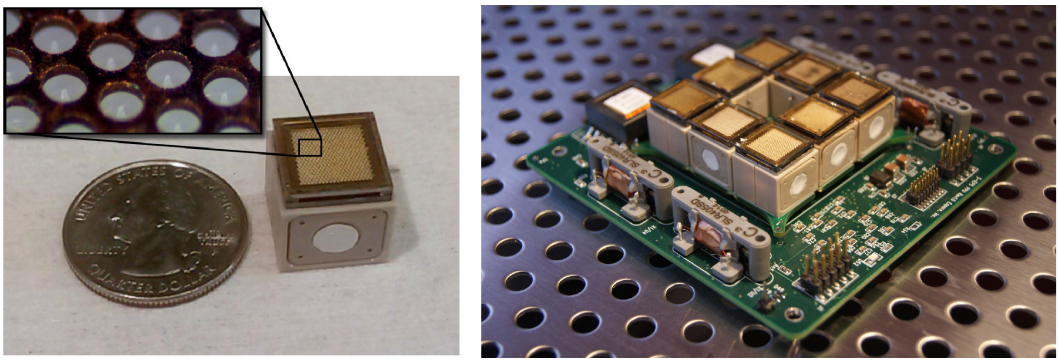

Figure 3.19: A S-iEPS thruster unit (left) and an integrated S-iEPS thruster including 8 units (right) [72].

Electrospray thrusters as the S-iEPS produce thrust by accelerating ions or droplets extracted from an electrically conductive liquid surface under an applied electrostatic field [72].

In order to minimise the electric field strength required for ion extractions, the ionic liquid propellant is typically sprayed onto a field enhancing structure, such as a needle or a sharp tip. In the process of extraction, the liquid deforms into a sharp, cone-shaped meniscus, known as a Taylor cone, in order to equilibrate the electrical pull and the surface tension and upstream pressure.

The increased electric field strength at the cone tip leads to the extraction of charged particles, which are then passed through a static electric field that accelerate them generating thrust (Figure 3.20). The field is created by the potential difference between the emitter and the extractor grid (Figure 3.19).

Electrospray thrusters can operate in droplet emission mode or ion emission mode. The S-iEPS is a colloid based thruster that typically emit larger charged droplets (droplet mode) using a charge-neutral propellant.

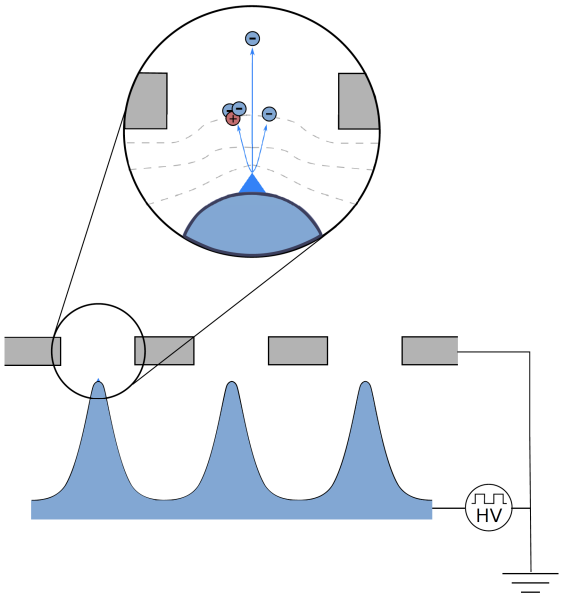

Figure 3.20: Schematic representation of the electrospray principle: charged particles extracted from menisci on top of a porous emitter structure [72].

Another notable electric propulsion system is the Field Emission Electric Propulsion (FEEP) system. FEEP systems typically emit individual ions (ion emission mode) and requires a neutraliser that emits electrons into the exhaust in order to neutralise the particles.

A highly miniaturised Field Emission Electric Propulsion (FEEP) system called NanoFEEP, developed at Technische Universität Dresden, consists of compact thruster heads (depicted in Figure 3.21) with a volume of less than 3 cm^3 and a weight of less than 6 grams each [73].

These thrusters utilise Gallium as metal propellant, which has a low melting point of approximately 30°C, enabling a very compact design and low power consumption (heating power demand between 50 and 150 mW) [73].

One thruster is able to generate a continuous thrust of up to 8 μN with short term peaks of up to 22 μN.

The NanoFEEP Thruster were integrated into the rails of the 1U UWE-4 CubeSat (University Würzburg Experimental satellite-4), which was launched into a sun-synchronous orbit at an altitude of 585 km on December 27, 2018, on board of a Soyuz-2.1a/Fregat-M Vehicle from the Vostochny Cosmodrome [74]. On February 26, 2019, one of the UWE-4 NanoFEEP thrusters was successfully ignited, marking the first activation of an electric propulsion system on a 1U CubeSat in space [75].

Figure 3.21: NanoFEEP Thruster head: a detailed schematic (left) and a photo of a manufactured prototype [73].

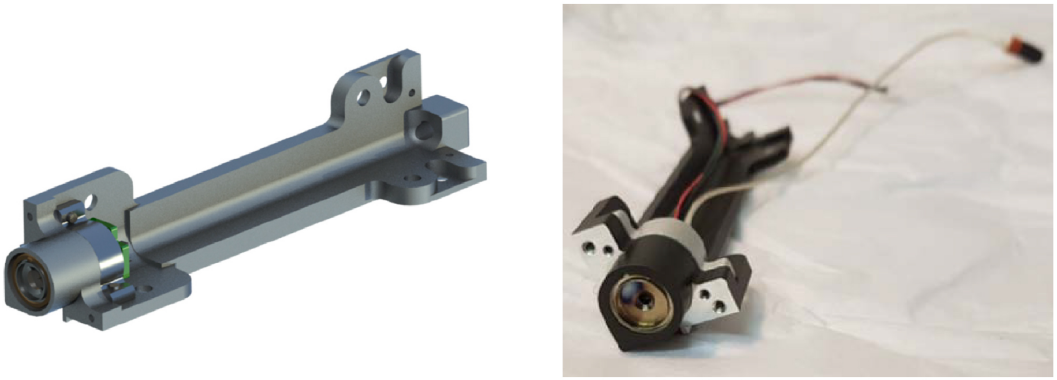

Figure 3.22: The NanoFEEP Thruster integrated in the Rail of the UWE-4 CubeSat [73].

3.4 Telemetry, Tracking and Command (TT&C)

The Telemetry, Tracking, and Command (TT&C) or Communications Subsystem serves as the interface between the spacecraft and the ground systems or other satellites in space [64].

This subsystem performs three primary functions: enabling the spacecraft to transmit payload data and spacecraft telemetry to Earth (downlink), relaying information between spacecraft (crosslink or inter-satellite link), and receiving commands from on-Earth-operators (uplink) which may need to command the spacecraft or operate the payload.

Currently, two main types of communication systems are used: Radio

Frequency (RF) and Free Space Optical (FSO), also known as laser communication (lasercom) [58]. Table 3.1 provides a list of the Radio Frequencies commonly used for communication.

Band	Frequency
VHF	30 to 300 MHz
UHF	300 to 1000 MHz
L	1 to 2 GHz
S	2 to 4 GHz
C	4 to 8 GHz
X	8 to 12 GHz
Ku	12 to 18 GHz
K	18 to 27 GHz
Ka	27 to 40 GHz
V	40 to 75 GHz

Table 3.1: Radio Frequency Bands.

For small satellites, lower frequencies like UHF and VHF have been widely adopted and are considered more mature. Higher frequency bands such as S and Ka have been employed to achieve higher data rates. However, as the frequency increases, so does the attenuation caused by rain, atmosphere, and path loss. To compensate the larger attenuations, higher transmission powers and/or higher gain antennas are required, which result in narrower beam widths and the need for precise pointing capabilities.

Ku-, K-, and Ka-band frequencies are considered state-of-the-art for large spacecraft but are becoming more attractive for smaller satellites as well. This is because lower frequency bands are becoming more congested and future missions are likely to have higher data rate requirements.

Lasercom technology holds great promise in terms of data rates due to its operation at higher frequencies, which offer wider bandwidths. However, it requires extremely precise and accurate pointing due to narrower beam widths therefore small satellites may face challenges in meeting these pointing requirements. Additionally, optical communications is particularly affected by cloud cover, which causes significant attenuation due to moisture in clouds [58].

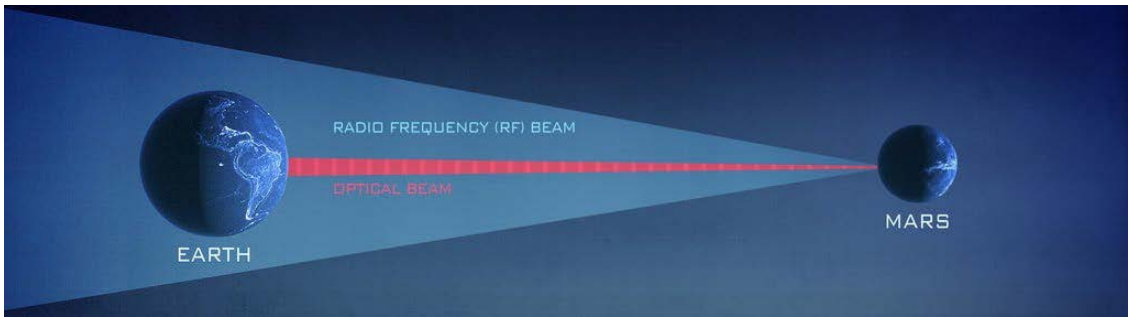

Figure 3.23: Laser vs RF Beam Width [58].

3.4.1 Radio Frequency Communication

A typical RF communication system on a small satellite consists of a transceiver, which doubles as both a transmitter and a receiver, and includes a radio, amplifiers, and an antenna.

During transmission, the radio receives the message from the onboard computer and modulates an electromagnetic wave to generate a signal for transmission. A power amplifier is often included to amplify the signal produced by the radio before it is transmitted through the antenna.

The antenna plays a crucial role in focusing and strengthening the signal in a specific direction. However, small satellites typically trades high-gain directional antennas for low-gain, omnidirectional ones, such as patch or monopole antennas. These antennas have a wider beam width, allowing the spacecraft to maintain the communication link regardless of the spacecraft's orientation. On the contrary, an high-gain directional antenna would require a precise pointing.

During reception, the antenna picks up a weak signal, which is then amplified and filtered by a low noise amplifier (LNA) to remove any noise or unwanted frequencies. The radio then demodulates the signal, extracting the message that will be processed by the on board computer.

In terms of miniaturization, as electronic components continue to shrink and become more efficient, Software Defined Radios (SDRs) have emerged as an attractive solution for small satellites. SDRs implement all radio functions in a digital signal processing (DSP) software, which can be reconfigured even while in orbit. These SDRs are typically implemented using Field Programmable Gate Arrays (FPGAs), which offer a small form factor and low power requirements.

Chapter 4

LEAn Femto (LEAF) Sat Prototype Design and Integration

This chapter presents the design and development of the LEAn Femto (LEAF) Sat Prototype. Before delving into the details, it is important to explain the rationale behind the attributes *lean* and *femto* that form the LEAF acronym.

As discussed in Chapter 1, this thesis aimed at investigating technologies for satellite miniaturisation with particular focus on those technologies that would enable the development of femtoSatellites, namely spacecraft that weigh less than 100 grams. Being femto-Satellites the main topic of this thesis, we aimed at proving the feasibility of such small form factor by integrating a new functional femto-satellite prototype, from this the attribute *femto*.

Furthermore, when comparing the weight of a femto-satellite, which is limited to 100 grams, with that of traditional satellites, the LEAF acronym vividly conveys the concept of a final prototype that weighs as light as a leaf in comparison to traditional satellites.

For what concern the *lean* attribute, the concept of "lean satellites" emerged during the International Workshop on Small-Scale Satellite Standardisation (IWS4) in Kitakyushu, Japan, in November 2014. During this workshop, the definition of small satellites was extensively debated. The term *lean* was introduced to describe the philosophy of design, manufacturing, and mission programming that underlies small satellites, rather than focusing solely on their mass or size, which were deemed inadequate for defining small satellites. The concept of *lean* thus refers to spacecraft that *utilises untraditional*

risk-taking development approaches to achieve low-cost and fast-delivery with a small number of team [76].

Our objective was therefore to develop a femto-class satellite weighing less than 100 grams, while minimising costs and facing a significantly tight schedule, striving to integrate a fully functional prototype in the shortest possible time. To achieve this, we opted to use non-space-qualified Commercial Off-the-Shelf (COTS) components, which helped reducing both costs and development time. Therefore, the LEAF Prototype was developed using an unorthodox, risk-taking approach that contrasts with traditional satellite development, where reliability often takes precedence over cost considerations. While this approach involves a certain level of risk associated with the use of COTS components, it enables faster delivery, lower costs, and a smaller development team.

In the following sections the LEAF Prototype design and development will be outlined providing details on each component used and the reason behind those choices.

4.1 Structure

ThinSat Standard

The CubeSat Standard was introduced by Bob Twiggs with the aim of reducing spacecraft costs and development time, thereby increasing accessibility to space, particularly for smaller companies and universities.

Between 2017 and 2019, Bob Twiggs recognised the shortage of scientists and engineers, which posed a significant challenge to the aerospace and defence industry. To address this issue, he believed that providing students in middle school, high school, and undergraduate programs with authentic, hands-on experiences in space applications would enhance their engagement in Science, Technology, Engineering and Mathematics (STEM) disciplines [77].

To achieve this goal, the ThinSat Program was established through a collaboration between the Virginia Commercial Space Flight Authority (Virginia Space), Twiggs Space Lab, LLC (TSL), Orbital ATK, NearSpace Launch, Inc. (NSL), and the National Aeronautics and Space Administration (NASA). The program offered students the opportunity to develop valuable STEM skills through hands-on experience in space-based research [77].

The ThinSat is conceived as a slice of the CubeSat. Each ThinSat unit, referred to as a “T”, weighs approximately 280 grams and has dimensions of

111.1 x 114.2 x 12.5 mm (Figure 4.1). This dimensions enable ThinSats to fit within a standard 3U Canisterized Satellite Dispenser (CSD) where up to 21 ThinSats can be accommodated for launch.

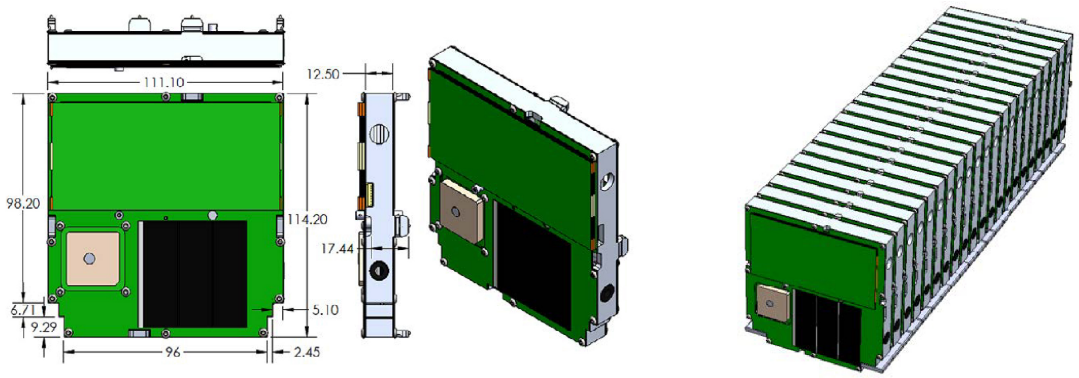

Figure 4.1: ThinSat Dimensions in Millimetres and 21 ThinSats Stacked in a 3U Volume [77].

Multiple ThinSat Units can be grouped together to form "Strings" in multiples of 3, as depicted in Figure 4.2.

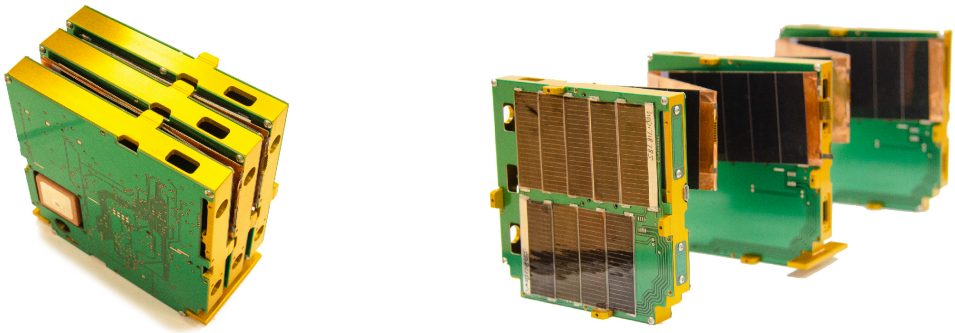

Figure 4.2: Pictures of a 3T ThinSat String [78].

LEAF Prototype Structure

Our objective was to push the boundaries set by the PocketQube standard and explore further miniaturization possibilities. Inspired by the ThinSat, which was essentially a fraction of the CubeSat, we decided to develop a newer femtoSat prototype that was a slice of the PocketQube. The resulting LEAF

Prototype measures 50 x 50 x 12 mm (Figure 4.3), which is approximately a quarter of the size of a typical 1P PocketQube.

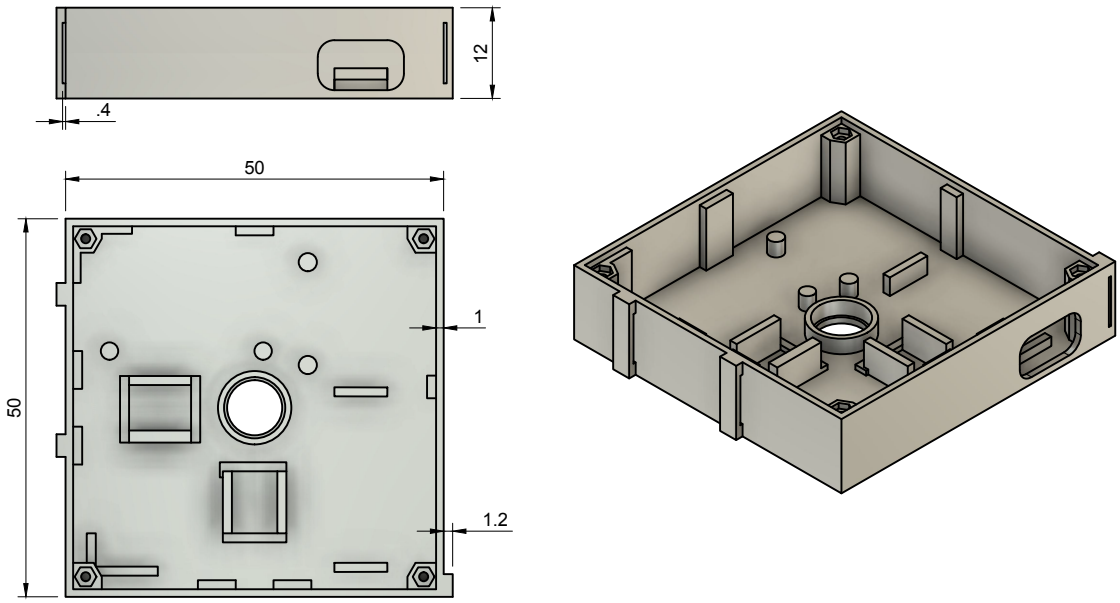

Figure 4.3: LEAF Prototype Dimensions in Millimetres.

To design the satellite's structure, we utilised the computer-aided design (CAD) software Fusion 360 developed by Autodesk. Starting from a simple square box baseplate, we made several modifications to ensure that all the components could fit inside it and could be properly housed.

One challenge we faced was finding a way to fix the top plate to the baseplate. Traditional standoffs were not suitable for our design, as the available M2 standoffs were too large. We could not find M1 standoffs, but M1 hex nuts and screws were readily available. As a solution, we incorporated standoffs-like structure into the baseplate design inside of which M1 nuts would have been embedded. In order to do this, we paused the 3D printing process at the 76th level in order to insert the nuts into their designated slots. Afterward, we resumed printing to complete the remaining layers, effectively embedding the nuts into the baseplate itself (Figure 4.4).

The satellite also includes two DC Coreless Motors that function as reaction wheels. Integrating the motors into the baseplate was a challenge because the camera hole in the middle of the baseplate obstructed their placement. Additionally, the printer cannot easily create cylindrical holes. To overcome these limitations, we decided to print the motor boxes separately

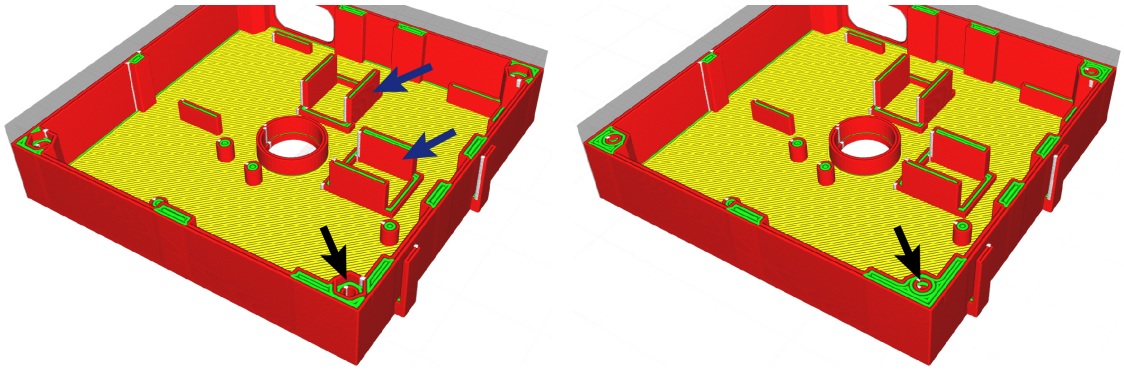

Figure 4.4: On the left the 76th Layer where the 3D printer is stopped to insert the M1 hex nuts, on the right the 77th layer that is printed above the nuts embedding them in the baseplate.

and then integrate them into the baseplate, where we created dedicated slots (Figure 4.4, blue arrow). Printing the motor boxes separately allowed us to print them vertically without the need for supports, simplifying the process.

The "pins" and "walls" visible in Figure 4.3 are supports included to maintain the proper positioning of each module. Additional supports were included for the external walls too, in order to enhance the overall structural stability. We also added small supports on the external surface to secure the measuring tape antenna.

Figure 4.5 provides another detail of the design: one of the standoffs in the baseplate has a cut to accommodate the motor driver which, otherwise, would not have fit properly inside the baseplate. To ensure proper printing of the upper part of the standoff, supports[1] were included with the UltiMaker Cura Slicing Software.

To access the microcontroller USB-C port, we made a hole in the external surface. Again, supports were necessary during the printing process to ensure a successful print (Figure 4.6). Supports are then removed once the print is completed.

The top plate remains in position thanks to a hex nut printed on it, which fits inside the standoff of the baseplate. A slot was purposely made on top of the standoff to accommodate this arrangement (Figure 4.5).

Regarding thickness, both the baseplate and the top plate of the LEAF Prototype are roughly 1 mm thick. The baseplate has an overall thickness of

[1]When there is no underlying layer for the 3D printer to build upon, supports are included in the design. Once the printing is complete, the supports can be removed.

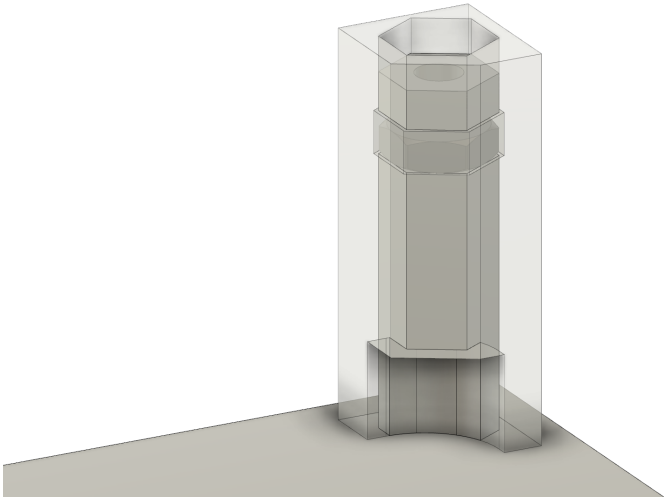

Figure 4.5: Focus on the standoff cut and on the nut that is embedded in the standoff.

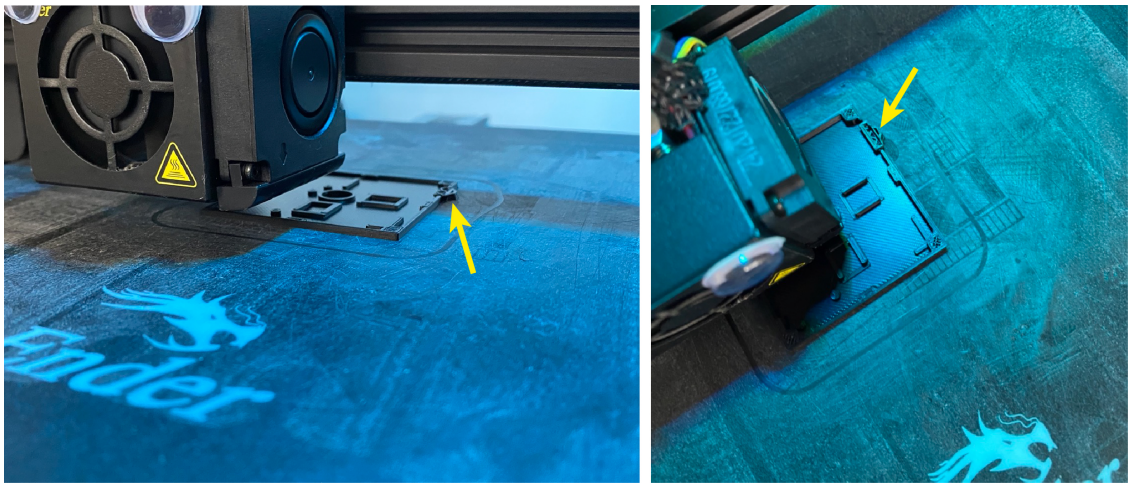

Figure 4.6: In the photos the supports necessary to correctly print the hole for the usb port.

12 mm. It has been printed with the Super Quality 3D print setting which makes each layer 0.12 mm thick so that a total of 100 layers compose the baseplate.

The baseplate made with PLA+ weighs around 7 grams, while the top plate weighs 3 grams, resulting in a total structure weight of around 10 grams. This weight includes the M1 Hex Nuts and M1 5 mm Flat Head Screws, which we were unable to weigh (Figure 4.7).

Figure 4.7: The M1 5 mm Screws and M1 Nuts compared to a 5 Pence Coin.

D diameter	pitch	m ≈	s ≈
M1 (1mm)	0.25mm	0.7mm	2.4mm
M1.2 (1.2mm)	0.25mm	0.9mm	2.9mm
M1.4 (1.4mm)	0.3mm	1.1mm	2.9mm
M1.6 (1.6mm)	0.35mm	1.2mm	3.1mm
M2 (2mm)	0.4mm	1.3mm	3.9mm
M2.5 (2.5mm)	0.45mm	1.8mm	4.9mm
M3 (3mm)	0.5mm	2.5mm	5.4mm

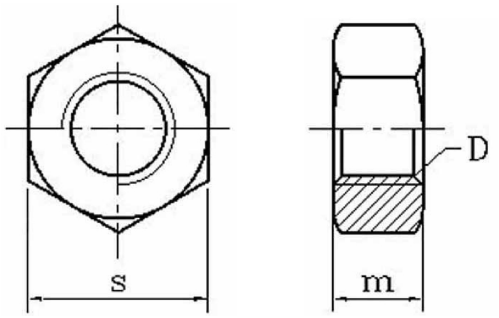

Figure 4.8: ISO Metric Hex Nut Dimensions.

Further Information

Diameter (d)	Pitch	dk	k	n	p
M1.0	0.25	1.9	0.7	0.25	0.30
M1.2	0.25	2.3	0.8	0.30	0.35
M1.4	0.30	2.6	0.9	0.30	0.40
M1.6	0.35	3.0	1.0	0.40	0.45
M2	0.4	3.8	1.3	0.50	0.60
M2.5	0.45	4.7	1.5	0.60	0.70
M3	0.5	5.6	1.9	0.80	0.85
M3.5	0.6	6.5	1.90	0.8	1.0
M4	0.7	7.5	2.2	1.0	1.1
M5	0.8	9.2	2.5	1.2	1.3
M6	1.0	11	3.0	1.6	1.6
M8	1.25	14.5	4.0	2.0	2.1
M10	1.5	18	5.0	2.5	2.6

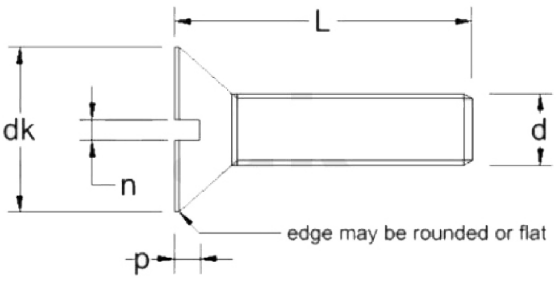

Figure 4.9: ISO Metric Flat Head Screw Dimensions.

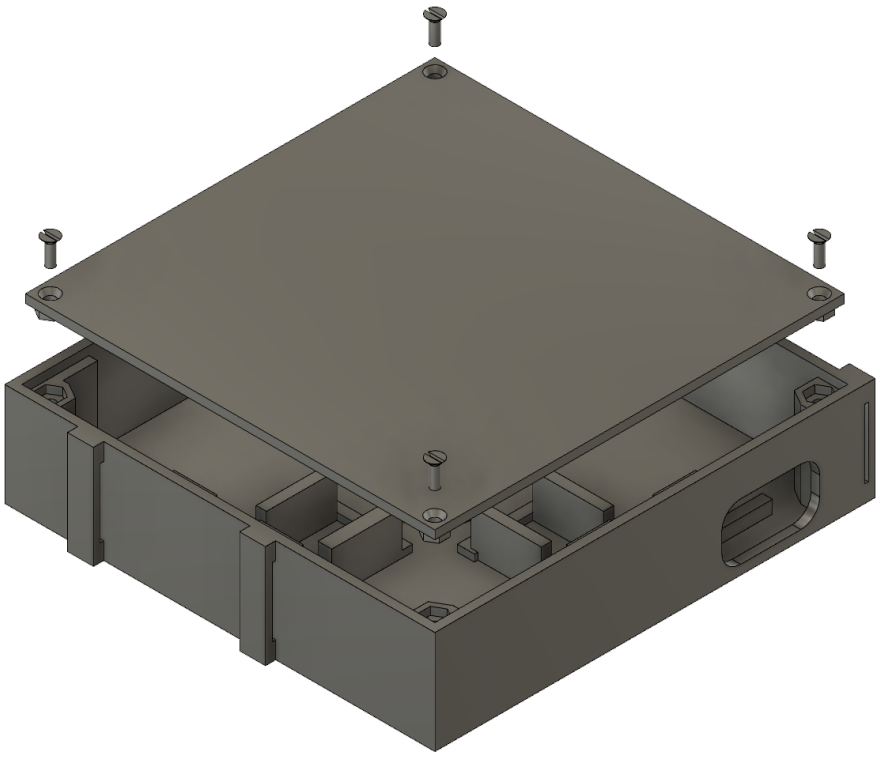

Figure 4.10: The Final LEAF Prototype Structure.

4.2 Electric Power System (EPS) and On Board Computer (OBC)

The selection of the onboard computer for the LEAF Prototype was driven by several factors, including small form factor, low power consumption, and the availability of a sufficient number of General Purpose Input Output (GPIO) pins to control the other subsystems.

ESP microcontrollers were an intriguing solution because, other than a microprocessor, they comes with a 2.4 GHz, 802.11 b/g/n Wi-Fi and Bluetooth 5 (LE) connectivity that provides long-range support. These microcontrollers are low-cost and commonly used in Internet of Things (IoT) applications, offering low-power consumption modes that are highly desirable for a small form factors spacecraft where limited power is available on board.

Given the limited time available, designing and manufacturing a customised Printed Circuit Board (PCB) was not a feasible option. Additionally, specialised tools to solder components and integrated circuits, such as the microcontroller, were not at our disposal. For this reason, we explored solutions such as pre-designed boards with integrated microcontrollers and also USB ports for convenient power supply and script downloading.

Several options from different vendors were considered, each offering different microcontrollers on board. Ultimately, we chose the XIAO ESP32S3 Sense by Seeed Studio due to its impressive features (Figure 4.11).

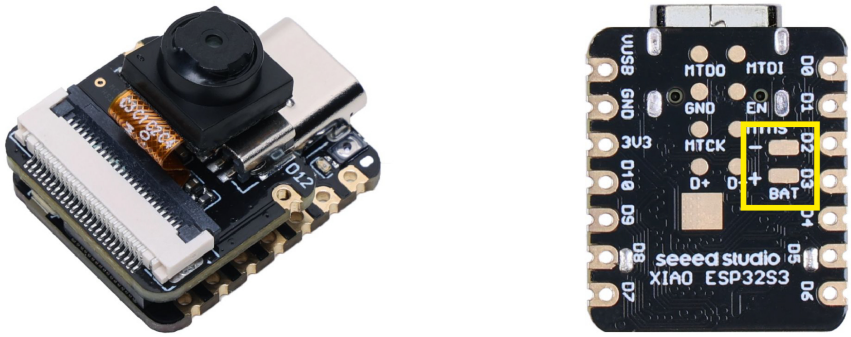

Figure 4.11: Seeed Studio XIAO ESP32S3 Sense. The complete system (left) and its Bottom Side where the Battery Connection Pads can be seen (right).

The ESP32S3 Sense includes an expansion board (the Sense Board) that allows for the connection of an OV2640 camera sensor and a MicroSD card. It also integrates a microphone, which in useless in space thus it was excluded in order to free up two additional GPIO pins on the Sense Board. In order

to do this, it was necessary to cut the J1 and J2 connections on the bottom side of the Sense Board (Figure 4.12, green arrows).

This choice was particularly advantageous being our plan to integrate a small camera as a payload. Cameras typically require a significant number of GPIOs, which can be challenging to accommodate on a small form factor board without occupying excessive space. However, the Sense Board utilises a compact Board-to-Board (B2B) connector, enabling the connection of multiple pins with just a small connector (see Figure 4.12, red arrows).

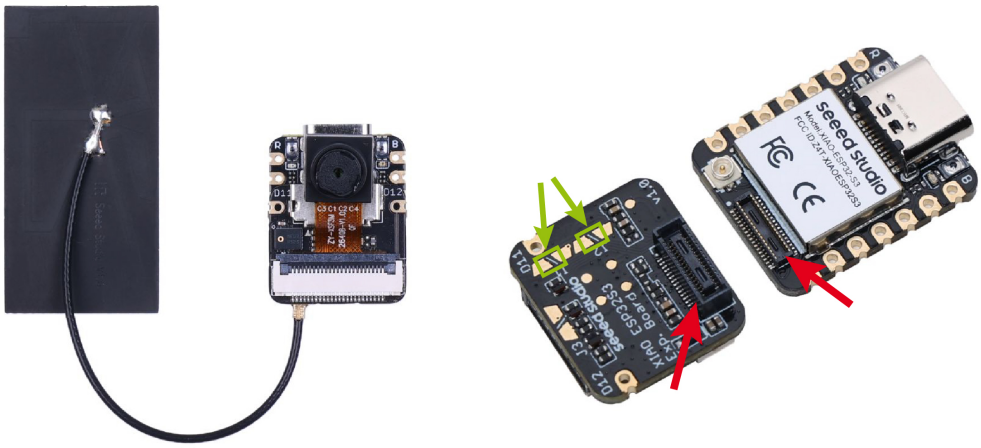

Figure 4.12: Seeed Studio XIAO ESP32S3 Sense. The complete system also including the U.FL Antenna (left) and the Sense Board separated from the Main Board to show the B2B Connector (right).

In terms of processing capabilities, the XIAO ESP32S3 Sense is equipped with an Espressif ESP32-S3 which is a dual-core XTensa LX7 32-bit processor that can operate at speeds of up to 240 MHz. This is essential for managing all the external modules and potential high-computation requirements of an attitude control algorithm.

Furthermore, the ESP32-S3 MicroController Unit (MCU) features 512 KB of internal SRAM and an external 8MB PSRAM (Pseudo Static Random Access Memory). The PSRAM provides additional memory space to extend the limited ESP32 RAM which can be useful in those applications with high memory demands such as image processing.

As previously mentioned, the ESP32-S3 MCU supports 2.4 GHz Wi-Fi and Bluetooth 5 (LE) with a declared range of more than 100 meters. The range performance requires testing, however this capability is really promising because it offers the possibility to create an high data-rate inter-satellite

communication link with a mother spacecraft when a direct link to Earth is not feasible.

The board also includes lithium battery charge management capabilities, with two pads on the bottom for connecting a battery (Figure 4.11, yellow box). The battery powers the entire system and it is charged when the board is connected via the USB-C cable.

Furthermore, the board features a 5V pin that outputs the 5V from the USB connection. However it can also be an input thus it can serve for integrating solar panels that would recharge the battery while exposed to sunlight. A proper connection using a Schottky diode should be considered.

To maximise versatility, we sought a board with as many GPIOs as possible. The XIAO ESP32S3 Sense provides a rich interface with 11 GPIO pins, each capable of outputting a Pulse-Width Modulation (PWM) signal. Additionally, the board offers various interfaces, including UART (Universal Asynchronous Receiver-Transmitter), I2C (Inter Integrated Circuit), and SPI (Serial Peripheral Interface). Nine Analog to Digital Converters (ADC) are also available.

All these functions are packed into a compact form factor of just 21 x 17.5 x 15 mm (including the expansion board) and a weight of just 4 grams.

The XIAO ESP32S3 can be easily programmed with the Arduino IDE, while also providing support for MicroPython.

In terms of power consumption, the vendor specifies that the board requires 43.2 mA at 3.8 V when powered by the battery. During the capture of a photo, the module requires a peak current of 304 mA. In Deep Sleep Mode, the module can consume as little as 3 mA. When WiFi communication is enabled, the consumption increases to 110 mA.

Lastly, the board offers an impressive operating temperature range of -40°C to +65°C, making it not far from being compatible with the demanding conditions of the Low Earth Orbit (LEO) environment.

In terms of power storage, the 402535 EEMB Rechargeable Lithium Polymer (LiPo) battery offers a viable solution with its compact dimensions of just 25.5 x 37 x 4.3 mm (Figure 4.13). With a capacity of 320 mAh, it provides a peak load current of 500 mA and a constant current of 200 mA, which should be sufficient to support the power requirements of the LEAF satellite.

It's worth noting that there are many other options available from various vendors, offering different form factors and capacities, which can also be considered. However, it's important to be aware of the working temperature limitation of LiPo batteries, which typically ranges from 0°C to 45°C.

Figure 4.13: 402535 EEMB Lithium Polymer (LiPo) Rechargeable Battery.

4.3 Telemetry, Tracking and Command (TT&C)

The design of the LEAF Prototype communication subsystem was given significant attention. Through the use of a Decision Matrix[2], it was determined that the communication subsystem holds the highest importance in a femtoSatellite, considering the potential missions that can be accomplished with these small spacecraft (Figure 4.14).

While the ESP32S3 already includes a 2.4 GHz Wi-Fi connectivity, it is essential to consider the limitations of this frequency band. Despite its higher data rate compared to lower radio frequencies, the 2.4 GHz band is susceptible to significant path loss, necessitating increased transmission power to cover large distances.

The XIAO ESP32S3 Sense, provided by Seeed Studio, claims a range of 100 meters or more. Although further testing is required to validate this range, it could already be sufficient to consider the LEAF Prototype as a viable solution for a distributed spacecraft mission architecture that provides the presence of a mothership. In such an architecture, the mothership could serve as a relay with the ground station, facilitating the data download from all the LEAF Prototypes in the swarm. Additionally, the mothership can also be conceived as the deployer of the satellite units.

[2]The Weighted Decision Matrix is a powerful quantitative technique that can be used to evaluate a set of choices against a set of criteria. It's an exceptionally useful tool that can come into play when you have to choose the best option and need to carefully consider a wide range of criteria.

WEIGHTED DECISION MATRIX

MISSIONS		Suitability of femtoSats	TT&C telemetry, tracking and control		Structure		EPS Power Generation		EPS Energy Storage		AODC *attitude and orbit determination and control*		OBDH *on board data handling*	
			RATING	TOTAL	RATING	TOTAL	RATING	TOTAL	RATING	TOTAL	RATING	TOTAL	RATING	TOTAL
Distributed Space System	Earth Observation	20%	8	0,40	4	0,20	6	0,30	6	0,30	8	0,40	5	0,25
	Telecommunication	25%	7	0,44	3	0,19	7	0,44	7	0,44	7	0,44	4	0,25
	Remote Sensing	35%	5	0,44	2	0,18	3	0,26	4	0,35	4	0,35	4	0,35
Scientific		10%	6	0,15	7	0,18	5	0,13	6	0,15	2	0,05	7	0,18
In Orbit Demonstration (IOD)		10%	5	0,13	6	0,15	5	0,125	6	0,15	2	0,05	4	0,1
TOTAL		100%		155		89		125		139		129		113

Figure 4.14: Decision Matrix that Highlights the Importance of the Communication Subsystem.

The inclusion of Bluetooth 5 (LE) connectivity in the ESP32S3 may not be necessary for typical spacecraft operations. However, it proves to be a valuable feature during the testing phase of the attitude control subsystem. This feature allows for communication with the spacecraft, enabling data reception and the issuance of commands to the attitude actuators without interfering with the attitude dynamics using cables connected to the spacecraft.

Considering the limited range of the integrated 2.4 GHz Wi-Fi connectivity (100 meters), an additional radio transceiver was incorporated into the LEAF Prototype to enable longer distance communication with other spacecraft or, optimistically, Earth stations. For this purpose, the RFM98W-433S2 Low Power Long Range Transceiver Module by HopeRF was selected (Figure 4.15). Despite its compact dimensions of 16 x 16 mm and a weight of less than 1 gram, it offers a +20 dBm (100 mW) constant RF output power and high sensitivity down to -144 dBm in the 433 MHz band.

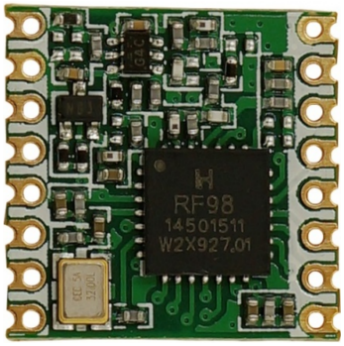

Figure 4.15: HopeRF RFM98W-433S2 Low Power, Long Range (LoRa) Transceiver Module.

The radio operates at 3.3V and requires a maximum of 120 mA while transmitting at the maximum power of 20 dBm, and just 12 mA while receiving.

A link budget attempt is presented in Table 4.1.

P_r [dBm]	=	P_t [dBm]	G_t [dBi]	G_r [dBi]	P_{pl} [dBm]	$-P_{\text{pol}}$ [dBm]
-122		20	0	0	-139	-3

Table 4.1: Link Budget for RFM98W Radio.

The link budget parameters are defined as follows: P_r represents the Received Power, P_t denotes the Transmitted Power, G_t and G_r are the Transmitter and Receiver Antenna Gain, respectively. $P_{\text{pl}} = 20 \log\left(\frac{\lambda}{4\pi R}\right)$ is the Path Loss, where R is the communication range, and P_{pol} accounts for polarisation mismatch losses, typically assumed to be 3 dBm [35][79].

For our analysis, the Transmitted Power P_t is considered to be 20 dBm, which is the maximum transmitting power of the RFM98W radio. This assumption is like considering a LEAF Prototype as the transmitting source. Both the Receiver Antenna Gain G_r and Transmitter Antenna Gain G_t are assumed to be zero. The communication range R is considered to be 400 km, representing the maximum distance of a Very Low Earth Orbit (VLEO), where a femtoSatellite would be likely deployed to mitigate space debris concerns.

Considering the -140 dBm sensitivity of a receiving LEAF Prototype, we obtain a link margin of 18 dBm. This margin accounts for any unmodeled attenuation and should be sufficient to ensure proper signal reception.

The RFM98W radio does not have an integrated antenna; instead, it provides a pin for soldering an external antenna. Figure 4.23 shows the two different antennas that have been utilised: the LEAF Prototype on the left utilises a measuring tape antenna (a piece of an actual measuring tape), while the one on the right uses a simple wire antenna. Both antennas are quarter-wave length antennas, measuring 16.5 cm[3]. This antenna length is confirmed by the datasheet of the Adafruit RFM9X LoRa Packet Radio Breakouts Module that includes the same RFM98W radio. The measuring tape antenna is also 16.5 cm long, but it should be shortened to account for the 4 cm cable that connects it to the radio pin.

Currently, the radio transmits the 9DoF Motion Sensor data. We are exploring possible ways to send the photos taken by the on-board camera. However, the LoRa (Long Range) protocol is typically used for small amounts of data with low data rates but extended range capabilities, and may not be

[3]The wavelength for a given operating frequency can be calculated using the formula $\lambda = c/f$, where c is the speed of light and f is the operating frequency. In our case, with an approximate value of $c = 300$ m/s and $f = 433$ MHz, we find $\lambda = 0.6928$ m thus $\lambda/4 = 0.1732$ m. To retrieve the 16.5 cm length, we need to introduce the 0.95 velocity factor, which accounts for the fact that the speed of the current in the wire antenna is not as fast as the speed of the light, because *nothing goes as fast as light but light!*. We need to know "how big" a quarter wave is in the wire and to do this we need to consider the speed at which the charge propagates along the wire, which is typically around 95% of the speed of light for most wires. Thus $\lambda/4 * 0.95 = 0.1645$ m which is our antenna length.

suitable for sending images. If it is not feasible to transmit pictures via the LoRa protocol, the LEAF Satellite still has the 2.4 GHz Wi-Fi radio that can be utilised to download the photos through a mothercraft relay. Considering that femtoSatellites are often used for in-situ space measurements, where a small amount of data is generated, sending the data with the LoRa protocol should be sufficient.

While the radio was successfully tested at a line of sight distance of 550 m, receiving a Received Signal Strength Indicator (RSSI) value of -80 dBm (Figure 4.16), further testing is required to determine the maximum achievable distance. Values down to -124 dBm have also been received, very likely at a distance of more than 1 km but with significant obstacles, such as houses and trees, along the propagation path. The achieved -80 dBm RSSI at 550 m is a promising result, and it can be expected to successfully receive signals at distances of several kilometres in a line-of-sight scenario.

Figure 4.16: Communication Test over 550 m in line-of-sight.

It is important to address several issues in future development. First, in order to ensure optimal performance of the radio, impedance matching for the antenna (both the measuring tape and wire antenna) needs to be considered, as an impedance mismatch could degrade radio performance or even damage the radio chip. Second, determining the best antenna length which is also crucial for achieving optimal radio performance.

Other radios were also considered for the LEAF Prototype. The EBYTE E22-400M33S, which incorporates the Semtech SX1268 Long Range (LoRa) Low Power radio transceiver, was a viable alternative. Operating in the 433 MHz band, it offers a maximum output power of 33 dBm (equivalent to 2 W) and a sensitivity of -125 dBm. However, its larger dimension (24 x 38.5 mm)

posed challenges for integration into our design. Moreover, the requirement for a peak power of 2 W is quite demanding, and it would be a challenge to meet this power requirement on board the LEAF femtoSat. On a positive note, the EBYTE radio costs approximately 10 euros, which is a great value considering its features and capabilities.

The RF Solutions LAMBDA62C-9S, featuring the Semtech SX1262 LoRa Modem operating in the 868/918 MHz band, was another interesting option. It offered a maximum transmission power of +22 dBm and a sensitivity of -148 dBm. The presence of a U.FL connector for the antenna would have facilitated the connection of a suitable antenna, reducing the risk of performance degradation due to impedance mismatch. However, its size (27 x 20 mm) proved to be larger than the RFM98W radio and posed difficulties in fitting it within our design.

4.4 Attitude Determination and Control (ADC)

An attitude control subsystem was also integrated into the LEAF Prototype.

It comprises two 4 x 12 mm DC Coreless MicroMotors, one positioned along the x-axis and one along the y-axis, enabling a two-axis attitude control system to stabilise the satellite's normal axis (z-axis).

We decided to integrate a two-axis attitude control system in order to be able to point the camera, which is positioned in the middle of the baseplate and oriented along the z-axis.

Without an actuator on the z-axis, only stabilisation along the x- and y-axes can be achieved. However, once the z-axis is properly aligned, any rotation of the satellite around it can be addressed through post-processing of the photos.

Including a third motor, such as a flat button-type motor similar to smartphone vibration motors, would enable z-axis stabilisation. However, this would require an additional H-Bridge Motor Driver and modifications to the rotor of the vibration motor in order to make it symmetric thus eliminating the vibration effect. However, the implementation of such modifications would be a challenge, particularly the rotor modifications.

Furthermore, an approximate computation of the satellite's inertia tensor, based on the designed 3D model, indicates that the spacecraft should exhibit asymptotic stability around the major principal axis, which roughly coincides with the normal z-axis due to the unique flat design of the satellite.

To maintain a compact design, we opted for the smallest motors available on the market. The DFRobot 4 x 12 mm DC Coreless Motors were chosen, operating at a supply voltage of 3.7 V with a rated current of 40 mA (Figure 4.17). These motors can achieve a maximum speed of 60.000 rpm. As the vendor does not provide information about the motor inertia, further testing is required to assess their capabilities.

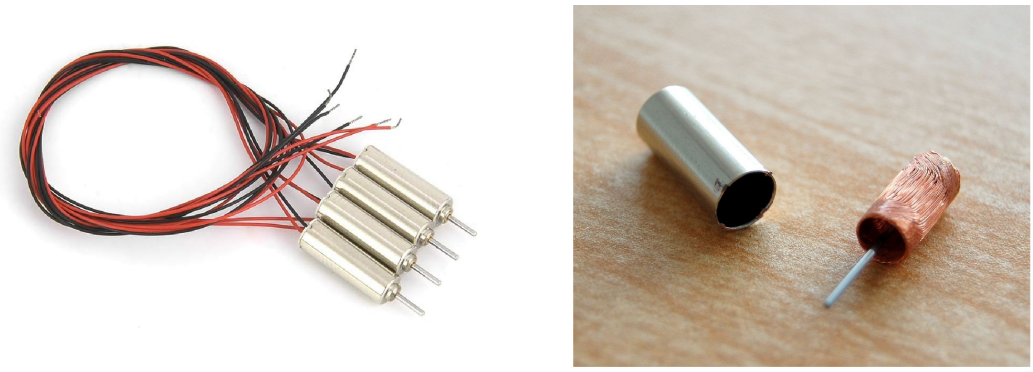

Figure 4.17: DFRobot 4 x 12 mm DC Coreless Micro Motors.

The Motor Driver Module, manufactured by Adafruit (Figure 4.18), embeds the Texas Instrument DRV8833 Motor Driver, which incorporates two full H-bridges. It can drive two DC motors bi-directionally, as required in our case, or it can drive a single stepper motor. The driver can operate with low voltages, ranging from 2.7 V to 10.8 V. The module also includes a built-in current limiter, set to 1 A per channel, which restricts the overall chip current to 2 A (this peak current limit should not be exceeded for an extended duration).

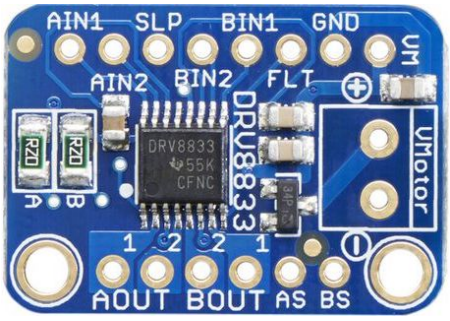

Figure 4.18: Adafruit DRV8833 Motor Driver, including two Full H-Bridges.

Each motor's speed is regulated using a Pulse-Width Modulation (PWM) signal. One PWM signal controls the forward velocity, while another controls

the reverse velocity. Hence, the chip provides two digital inputs per H-bridge (one for each half of the bridge). In total, four different PWM signals are required – two for each motor, one for forward motion and one for reverse. The digital PWM pins works with a logic voltage of 2.7 V or more.

It is worth noting that to enable the device, the nSLEEP (SLP) pin must be driven high. If the nSLEEP pin is driven low, the device enters in low-power sleep mode.

Attitude determination is entitled to the Pimoroni ICM20948 9DoF Motion Sensor, which integrates the ICM-20948 Motion Sensor developed by TDK InvenSense (Figure 4.19). TDK asserts that the ICM20948 is the most power-efficient 9-axis MotionTracking device available, incorporating a 3-axis gyroscope, a 3-axis accelerometer, a 3-axis compass, and a Digital Motion Processor (DMP).

This Pimoroni module utilises the I2C interface and is compatible with both 3.3 V and 5 V voltage supply. It also includes reverse polarity protection.

Figure 4.19: Pimoroni ICM20948 9DoF Motion Sensor.

4.5 Payload

Since the early stages of the LEAF Sat Project, the inclusion of a camera was considered.

However, incorporating a camera typically requires a significant number of GPIOs, which would result in bulky connections if each pin were to be soldered by hand. To address this challenge, we sought out a board with suitable connectors that could accommodate a large number of GPIOs within a small volume.

The Seeed Studio XIAO ESP32S3 Sense proved to be an ideal solution due to its compact form factor of just 21 x 17.5 x 15 mm and the inclusion of the Sense Expansion Board, which facilitates easy connection of the camera and a MicroSD card.

The selected camera is the OV2640, a 2 MP Image Sensor from OmniVision. This camera module is widely used in Do It Yourself (DIY) projects due to its affordability and compatibility with low-end ARM and RISC microcontrollers, such as STM32 and ESP32. The OV2640 CameraChip operates at a low voltage range of 1.7 to 3.3 V and provides a resolution of 1600 x 1200 pixels. It also features an on-chip Image Signal Processor (ISP) that supports auto-exposure, auto-white balance, and JPEG encoding capabilities. These features offload processing power from the microcontrollers and reduce memory usage [80].

The Sense Board is also designed to be compatible with the OV5640 Camera Sensor, an upgraded version of the old but gold OV2640. The OV5640 offers an higher 5 MP resolution. It also retains the on-chip Image Signal Processor (ISP) and JPEG compression capabilities, providing enhanced image quality and reducing the processing load on the microcontroller.

OV2640 camera modules are available with different lenses and cable lengths. The one provided in the XIAO ESP32S3 Sense package has a cable length of 21 mm, which was too short for our specific purpose (Figure 4.20, red arrow). Indeed, the camera lens had to be positioned in the middle of the baseplate, but the microcontroller had to be placed elsewhere in order to maintain a satellite thickness of just 1.2 mm. Therefore, a 75 mm cable (Figure 4.20, blue arrow) was needed to reach the camera connector as can be seen in Figure 4.23.

In terms of miniaturization, there are even smaller sensors available, such as the OV6948 Color CMOS Analog 40 Kpixel (200 x 200) Image Sensor. This sensor holds the Guinness World Record for *"The Smallest Commercially Available Image Sensor"*, measuring just 0.575 x 0.575 mm. Originally developed for small-outer-diameter medical endoscopes and catheters, it could be an intriguing solution for a Satellite-on-Chip Prototype. The sensor utilises OmniVision's OmniBSI+ pixel technology, delivering excellent image quality even in low-light conditions [81]. With a 4-pin interface and analog data output, the sensor enables easy integration and can transmit data up to 4 meters with minimal signal noise.

The OV6948 sensor is integrated into the OVM6948 CameraCubeChip depicted in Figure 4.21, which measures a mere 0.65 x 0.65 mm, with a z-height of just 1.158 mm. It is designed to provide high-quality imaging

Figure 4.20: Various OV2640 Camera Modules with Different Cable Length and Different Lenses.

for disposable devices used in the smallest areas of the anatomy, such as guidewires, catheters, or endoscopes with diameters as small as 1.0 mm. The sensor consumes only 25 mW of power and it can capture images and video at a resolution of 200 x 200 pixels and up to 30 frames per second, with a wide 120-degree field of view [82].

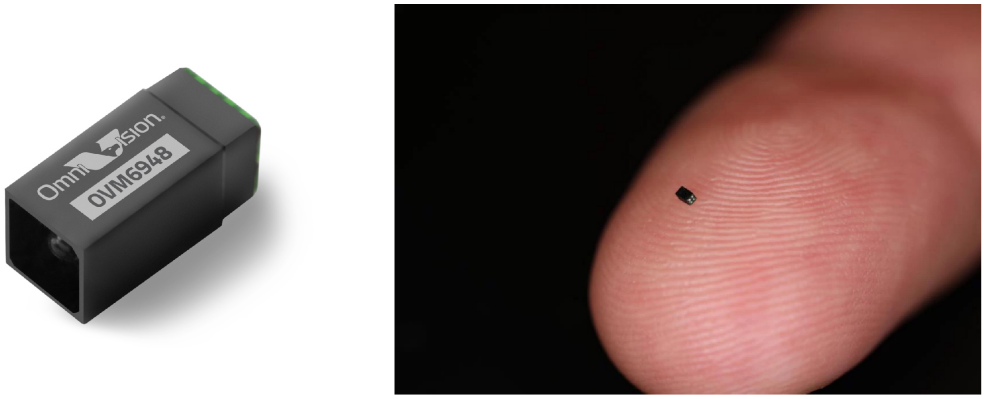

Figure 4.21: The OmniVision OVM6948 CameraCubeChip which integrates the OV6948 CMOS Image Sensor.

OmniVision's CameraCubeChip family includes a wide range of small wafer-level camera modules primarily designed for medical applications. These camera modules features impressively compact form factors, typically measuring just a few millimetres in size [83].

4.6 Final Prototype Considerations

Figure 4.22 depicts the complete 3D model of the LEAF femtoSat designed with Fusion 360. The images do not include the battery, as it would have covered the other components. Additionally, it is worth noting that the depicted OV2640 camera is not the one with a 75 mm cable, and the Sense Expansion Board is not represented, as their integration in the design would have been challenging.

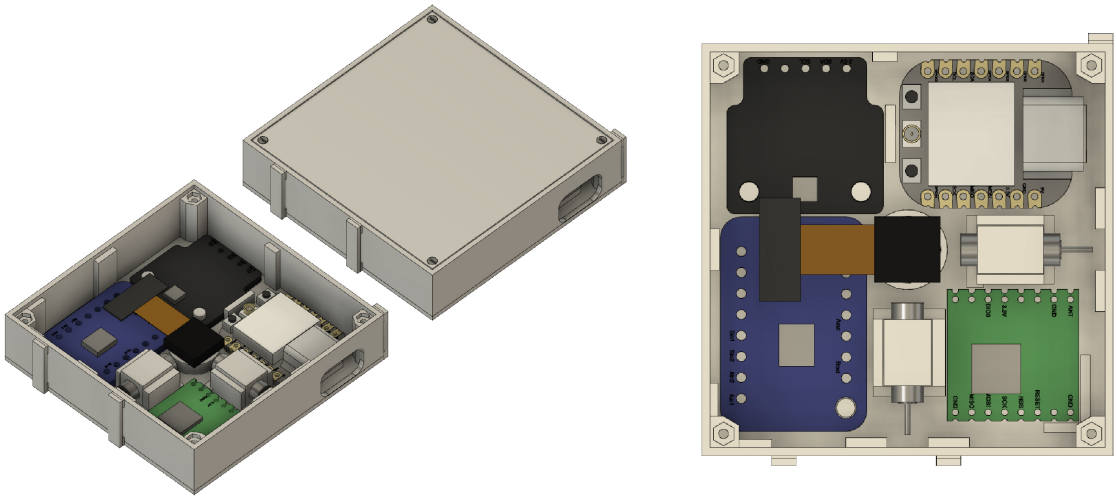

Figure 4.22: LEAF femtoSat 3D Model designed with Fusion 360.

An actual photo of the integrated LEAF Prototype is shown in Figure 4.23. The photo shows two prototypes, both of which include all the components except for the battery and solar panels. The prototype on the left utilises a measuring tape antenna, while the one on the right uses a simple wire antenna. These prototypes are the ones used for the communication test, with one functioning as the Ground Station (the one with the wire antenna) and the other as the on-orbit spacecraft (the one with the measuring tape antenna).

The current supports for the measuring tape antenna do not provide a deployment mechanism. Future developments will include the incorporation of a Dyneema wire to retain the antenna, along with a nichrome wire that can be heated to burn the Dyneema wire and deploy the antenna.

Figure 4.24 presents the complete connection schematic of the LEAF femtoSat.

The final LEAF femtoSat Prototype measures 5 x 5 x 1.2 cm and weighs

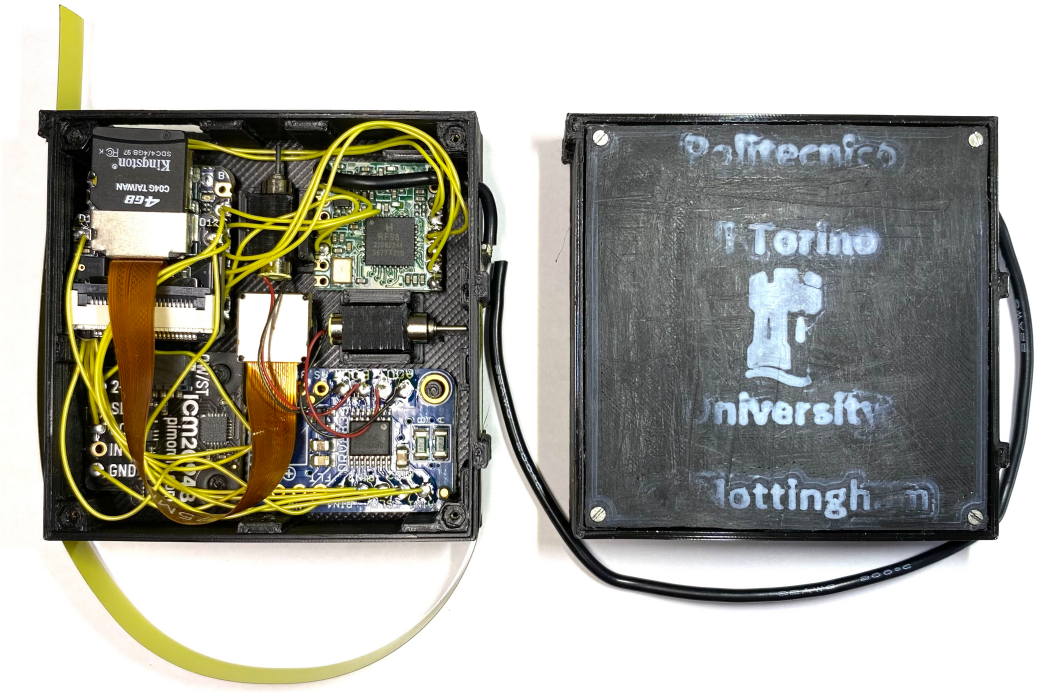

Figure 4.23: Two LEAF Prototypes Integrated, the left one with a Measure Tape Antenna, the right one with a Simple Wire Antenna.

just 21 grams (excluding the battery and solar panels), showcasing the feasibility of femtoSatellites. Furthermore, the LEAF prototype can be considered a lean femtoSatellite, as it has been integrated using only Commercial Off-the-Shelf (COTS) components, designed and integrated within a few weeks, with a total cost of less than 100 euros.

Table 4.2 provides a comprehensive list of all the components that compose the LEAF Prototype, along with their respective costs.

Table 4.3 is a summary table that compares the main characteristics of all the prototypes discussed in Chapter 2.1 and the ones of the LEAF Prototype.

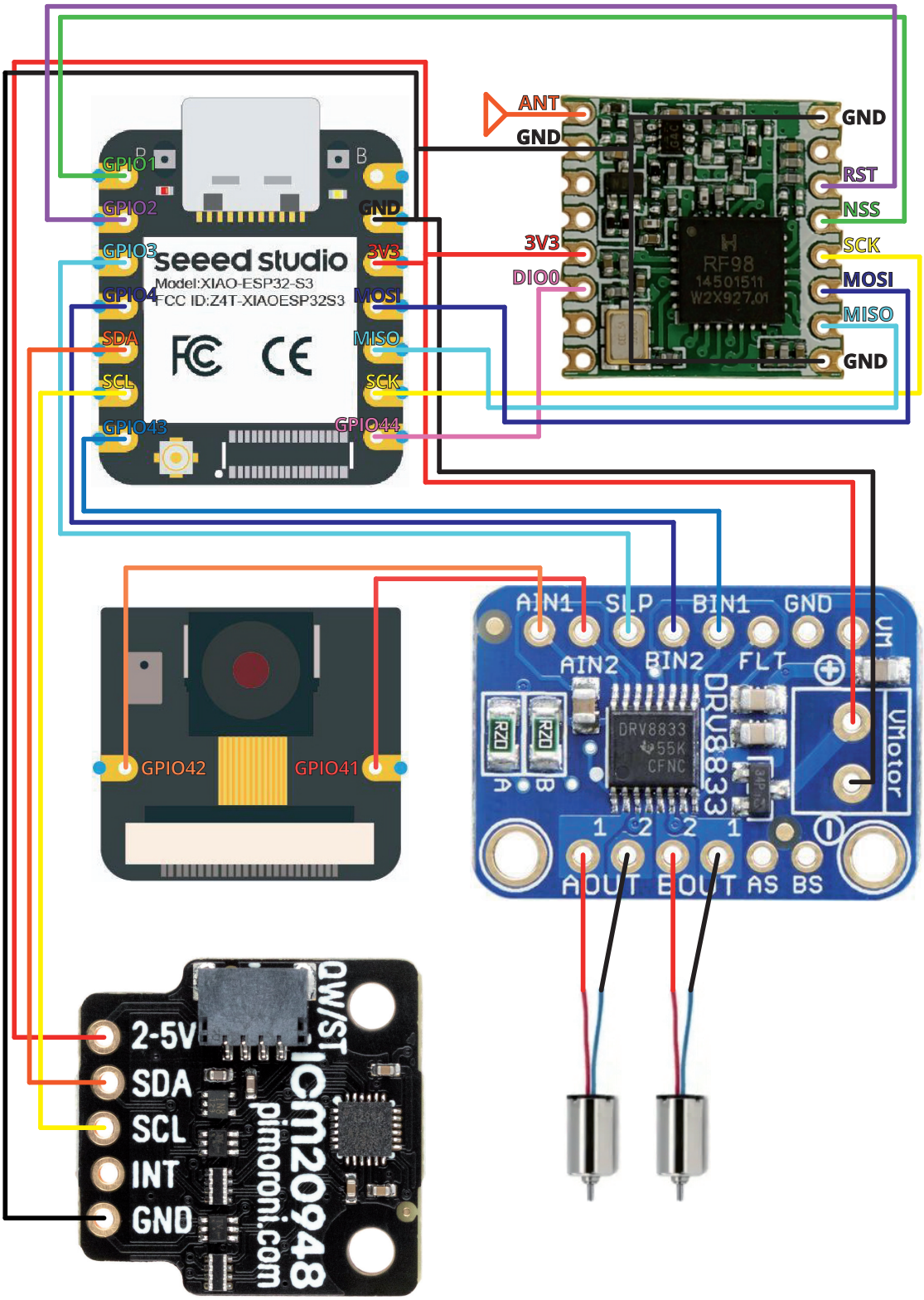

Figure 4.24: Connection Schematic of the LEAF femtoSat Prototype.

Component	Quantity	Unitary Cost [€]	Total Cost [€]
3D Printed Baseplate	1	0.14	0.14
3D Printed Top Plate	1	0.06	0.06
M1 Flat Head Screws 5 mm	4	0.22	0.88
M1 Hex Nuts	4	0.43	1.72
Seeed Studio XIAO ESP32S3 Sense	1	16.04	16.04
HopeRF RFM98W-433S2 (433 MHz) Radio	1	23.22	23.22
Adafruit DRV8833 Motor Driver	1	5.68	5.68
DFRobot DC Coreless Micro Motor (4 x 12 mm)	2	1.38	2.76
Pimoroni ICM20948 9DoF Motion Sensor	1	19.09	19.09
OV2640 Camera (75mm)	1	2.94	2.94
MicroSD Card 32GB	1	6.79	6.79
EEMB 402535 3.7V 320mAh LiPo Battery	1	9.59	9.59
Total Cost			88.91

Table 4.2: List of LEAF femtoSat Components and Costs.

Prototype	Sprite	Monarch	ChipSat	PCBSat	LEAF Satellite
Author	Manchester	Adams and Peck	Barnhart	Barnhart	Luca Bigelli
Integrated/Fabricated	yes	yes	no	yes	yes
Dimensions [cm]	3.5 x 3.5 x 0.25	5 x 5	20 x 20	10 x 10 x 2	5 x 5 x 1.2
Weight [grams]	4	2.5	<10	70	21
Attitude Control	no	2-axis	no	1-axis magnetorquer	2-axis
Attitude Determination	3-axis magnetometer, 3-axis gyroscope	gyroscope, accelerometer, magnetometer, light sensors, GPS	no	Sun Sensor, Fastrax iTrax-03S GPS receiver	ICM20948 9DoF Motion Sensor
Radio Communication	Texas Instrument C1101 433 MHz	25 mW, 915 MHz	2.4 GHz	2.4 GHz ZigBee module MaxStream XBee Pro	2.4 GHz WiFi 433 MHz LoRa
Solar Cells	Triangular Advanced Solar Cells	Alta-devices Solar Cells	yes	Seven Solar Cells	to be integrated
Power Storage	no	no	no	Olympus 645 mAh Li-Ion	320 mAh LiPo, to be integrated
Microprocessor	Texas Instrument MSP430	Texas Instrument CC1310	yes	8-bit Atmel Mega128 AVR	Seeed Studio XIAO ESP32S3 Sense
Payload	no	sensors	CMOS imager	640x480 CMOS Imager	OV2640 Camera
On orbit	4 times	no	no	no	no

Table 4.3: Comparison of Different femtoSat Prototypes.

4.7 Future Developments

The LEAF femtoSat Prototype was successfully designed, developed, integrated, and tested by the author within a relatively short time of just a few weeks. However, it should be noted that the final prototype represents a preliminary version and can be considered a rough prototype with room for various improvements and future developments.

One important improvement to be implemented is the inclusion of the chosen battery. This addition is a straightforward process as it simply involves soldering the battery onto the bottom of the XIAO ESP32S3. During the integration of the prototype, the decision was made to exclude the battery to avoid any potential risks for the onboard computer.

Additionally, the integration of solar panels is another straightforward modification required to complete the satellite. This involves selecting a suitable Schottky diode and connecting the solar panels to the 5V pin of the board. With careful consideration and proper implementation, this integration process should not present significant challenges.

In terms of structure, the prototype currently utilises a 3D printed PLA+ filament structure. While this may not provide high structural stability being printed layer by layer, tests can be conducted to evaluate its performance before considering an aluminium 7075 milled baseplate. Since each LEAF femtoSatellite is designed as a disposable unit, cost reduction through the use of a simple 3D printed structure would not be bad. Introducing an aluminium structure would increase both the weight and the costs of the spacecraft.

To enhance the Attitude and Orbit Determination and Control Subsystem, the inclusion of a GPS in future revisions could help in tracking the units in orbit further mitigating space debris concerns. If a unit can be tracked, also communication can be optimised, in order to properly steer the radio signal towards the satellite.

For attitude control, the inclusion of a specially modified flat vibration motor or other available solutions can be considered to achieve z-axis control, enabling full three-axis control. Additionally, a thorough testing phase of the existing attitude actuators, namely the two DC motors, is necessary to evaluate their performance in regulating spacecraft attitude.

For the communication subsystem, as discussed in the dedicated section, further distance testing should be conducted to assess achievable ranges. Testing other radios, such as the EBYTE E22-400M33S, would also be interesting for performance comparison and the potential to establish direct links with Earth's ground stations.

Another interesting modification would be the inclusion of a deployment mechanism for the measuring tape antenna. The existing supports on the baseplate can be replaced with a nichrome wire that, when heated, burns the Dyneema wire that holds the measuring tape antenna, allowing for its deployment.

The LEAF Project can pursue two main development paths.

One possibility is to maintain the chosen form factor, approximately a quarter of a 1P PocketQube, and modify the structure to enable deployment from standard PocketQube deployers. A purpose-designed PCB would be important for high integration of components, optimising space utilisation, and potentially accommodating a larger battery.

Another option is to further miniaturise the structure, adopting a Satellite-on-Chip design. While not a visionary concept anymore, achieving this would require a thorough expertise in MEMS and SoC technologies.

Regarding the software, each subsystem of the prototype has been individually tested with specific scripts. The development of comprehensive software that simulates a real mission, including a proper attitude control algorithm, is a necessary step.

Branch: a String of LEAF Satellites

Inspired by the concept of the String of ThinSats, a "Branch" of LEAF Satellites can be considered. Each unit within the string could be dedicated to one of the main subsystems. For example, in a string of three LEAFs, one unit could be dedicated to the onboard computer, another to the communication subsystem, and the third to the power storage.

Additionally, following the design suggestion from the ThinSat String, the patches connecting the LEAF units could be utilised to deploy additional solar panels, increasing the available onboard power. Research in flexible solar cells aligns well with this idea.

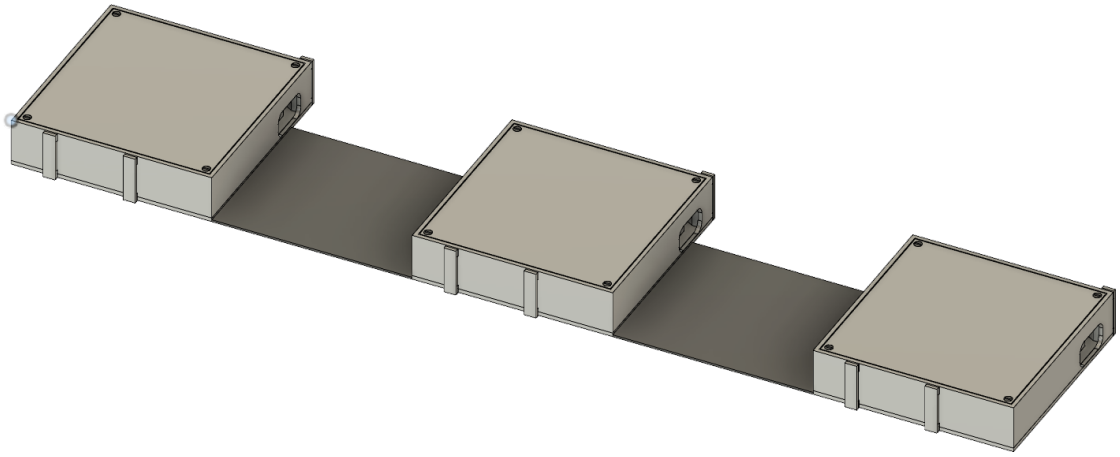

Figure 4.25: The Branch Concept: a String of LEAFs.

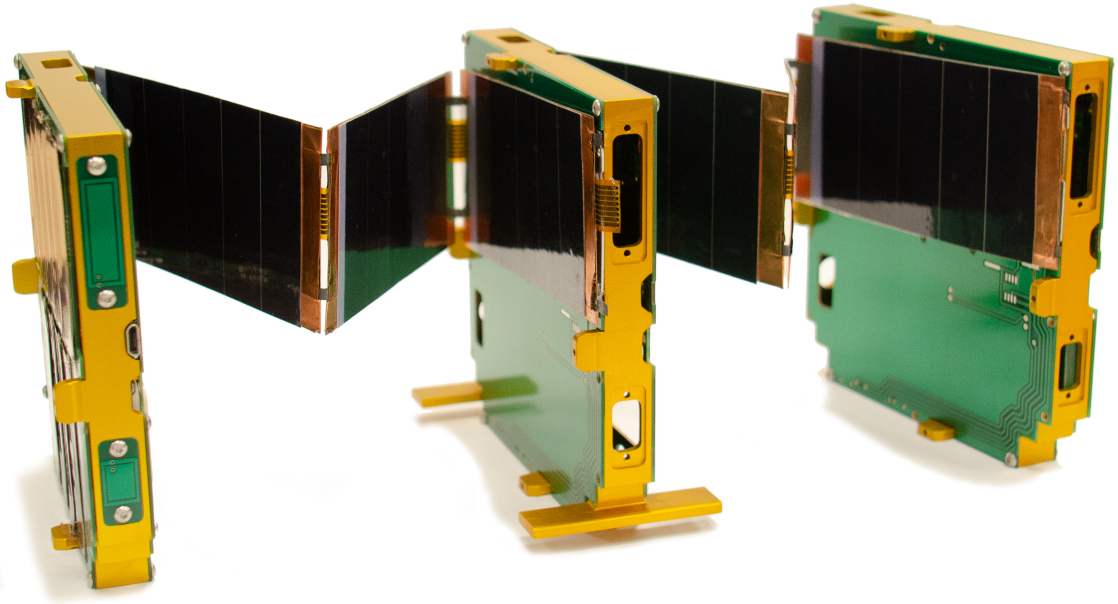

Figure 4.26: The ThinSat String [84].

Chapter 5

Conclusions

The conducted survey demonstrates that the trend towards satellite miniaturization, even down to the femto-class, is no longer a visionary idea.

Thanks to the significant technological advancements of recent decades and the refined fabrication processes available to industries today, appealing Commercial Off-the-Shelf (COTS) solutions enable the integration of very small satellites at costs as low as € 100 per unit, while also making development quick and easy.

Although these components are typically not space qualified and require thorough testing, with minor modifications and improvements, they can be very likely made ready for space missions.

An important aspect highlighted throughout this work is that satellite miniaturization opens up space access to a broader range of entities, including small companies and universities, facilitating their participation in space exploitation and exploration.

As the adoption of small form factor satellites continues to grow, so does the concern for space debris. However, the on-orbit tests of Sprites have demonstrated that if femtoSatellites are deployed in Very Low Earth Orbit (VLEO), below 400 km altitude, they are likely to harmlessly re-enter and burn up in the atmosphere within weeks or months. Currently, powerful radars used by the U.S. Air Force, responsible for cataloging and tracking most space debris to provide early warnings for astronauts and satellite operators, are unable to track very small debris, typically under 10 cm in size.

The design, integration, and testing of the new LEAF femtoSat prototypes further confirm the feasibility of lean femtoSats. These prototypes can be developed within a few weeks of work at an highly competitive cost, mainly due to the use of Commercial Off-the-Shelf Components.

While the LEAF Prototype is at a preliminary stage, leaving room for future developments as discussed in the dedicated session, it has demonstrated full functionality. As a result, the author takes pride in having achieved the initially set goal of integrating an innovative, albeit unconventional, femtoSatellite.

Bibliography

[1] Herbert J. Kramer and Arthur P. Cracknell. «An overview of small satellites in remote sensing». In: *International Journal of Remote Sensing* 29.15 (2008), pp. 4285–4337. DOI: 10.1080/01431160801914952.

[2] R. C. Botelho A. S. and A. Xavier Jr. «A Unified Satellite Taxonomy Proposal Based on Mass and Size». In: *Advances in Aerospace Science and Technology* 4 (Oct. 2019), pp. 57–73. DOI: 10.4236/aast.2019.44005.

[3] M. N. Sweeting. «Why Satellites Are Scaling Down». In: *Space Technology International* 7 (1991), pp. 55–59.

[4] G. Konecny. «Small Satellites - A Tool for Earth Observation?» In: *Proceedings of 20th ISPRS Congress*. Vol. 4. 2004, pp. 580–582.

[5] Federal Aviation Administration (FAA). *The Annual Compendium of Commercial Space Transportation: 2018*. URL: https://www.faa.gov/about/office_org/headquarters_offices/ast/media/2018_ast_compendium.pdf.

[6] Bryce Space and Technology. *Smallsats by the Numbers*. 2020. URL: https://brycetech.com/reports/report-documents/Bryce_Smallsats_2020.pdf.

[7] CA The CubeSat Program Cal Poly - San Luis Obispo. *CubeSat Design Specification*. 2022. URL: https://www.cubesat.org/s/CDS-REV14_1-2022-02-09.pdf.

[8] Ravi A Deepak and Robert J Twiggs. «Thinking out of the box: Space science beyond the CubeSat». In: *Journal of Small Satellites* 1.1 (2012), pp. 3–7.

[9] eoPortal. *CubeSat - Launch 1*. 2012. URL: https://www.eoportal.org/satellite-missions/cubesat-launch-1 (visited on 06/21/2023).

[10] Erik Kulu. *Nanosats Database*. 2012. URL: https://www.nanosats.eu (visited on 06/21/2023).

[11] Alba Orbital, TU Delft, and GAUSS Srl. *The PocketQube Standard, Issue 1*. 2018. URL: http://www.albaorbital.com/pocketqube-standard.

[12] Alba Orbital. *Alba Orbital - Launch*. 2023. URL: http://www.albaorbital.com/launch (visited on 06/22/2023).

[13] GAUSS Srl. *PocketQubes: The Origins*. 2023. URL: https://www.gaussteam.com/services/satellite-design/pocketqubes (visited on 06/22/2023).

[14] Gunter Dirk Krebs. *Gunter's Space Page - Beakersat 1 (Eagle 1, SWE-sat, MagPocketQube) → T-LogoQube*. 2013. URL: https://space.skyrocket.de/doc_sdat/beakersat-1.htm (visited on 06/22/2023).

[15] Gunter Dirk Krebs. *Gunter's Space Page - $50SAT (Eagle 2, MO 76, Morehead-OSCAR 76)*. 2023. URL: https://space.skyrocket.de/doc_sdat/$50sat.htm (visited on 06/22/2023).

[16] Morehead State University. *$50SAT - Eagle2 - Official Website*. 2013. URL: http://www.50dollarsat.info (visited on 06/22/2023).

[17] Gunter Dirk Krebs. *Gunter's Space Page - QubeScout S1*. 2013. URL: https://space.skyrocket.de/doc_sdat/qubescout-s1.htm (visited on 06/22/2023).

[18] Gunter Dirk Krebs. *Gunter's Space Page - Wren*. 2013. URL: https://space.skyrocket.de/doc_sdat/wren.htm (visited on 06/22/2023).

[19] GAUSS Srl. *UniSat-5 Mission*. 2023. URL: https://www.gaussteam.com/satellites/gauss-latest-satellites/unisat-5/ (visited on 06/24/2023).

[20] V. Hunter Adams and Mason Peck. «R-Selected Spacecraft». In: *Journal of Spacecraft and Rockets* 57.1 (2020), pp. 90–98. DOI: 10.2514/1.A34564. URL: https://doi.org/10.2514/1.A34564.

[21] Jacqueline Le Moigne, John Carl Adams, and Sreeja Nag. «A New Taxonomy for Distributed Spacecraft Missions». In: *IEEE Journal of Selected Topics in Applied Earth Observations and Remote Sensing* 13 (2020), pp. 872–883. DOI: 10.1109/JSTARS.2020.2964248.

[22] Sidereus Space Dynamics. *Discover EOS*. URL: https://www.sidereus.space/eos/ (visited on 07/04/2023).

[23] Jacqueline Le Moigne. *Distributed Spacecraft Missions (DSM)*. Presentation. Oct. 8, 2019.

[24] Eduardo Torres-Martinez et al. «A web of sensors: Enabling the earth science vision». In: *Acta Astronautica* 53.4 (2003), pp. 423–428. ISSN: 0094-5765. DOI: https://doi.org/10.1016/S0094-5765(03)00133-4.

[25] Ray A Williamson et al. «The socioeconomic benefits of Earth science and applications research: reducing the risks and costs of natural disasters in the USA». In: *Space Policy* 18.1 (2002), pp. 57–65. ISSN: 0265-9646. DOI: https://doi.org/10.1016/S0265-9646(01)00057-1.

[26] A. Barrett. «Multiple Platform Mission Taxonomy». In: *JPL-CaITech Internal Renort. Section 367.2001* (2001).

[27] David E. Steitz. «NASA Developing Space-Based "Sensor Web" - an Internet for Earth Observing Satellites». In: *NASA Headquarters Press Release* 00.65 (Apr. 25, 2000).

[28] L. Lemmerman et al. «Earth Science Vision: platform technology challenges». In: *IGARSS 2001. Scanning the Present and Resolving the Future. Proceedings. IEEE 2001 International Geoscience and Remote Sensing Symposium*. Vol. 1. 2001, pp. 439–443. DOI: 10.1109/IGARSS.2001.976183.

[29] Guan Le and DeLee Smith. *The Magnetospheric Multiscale Mission*. 2023. URL: https://mms.gsfc.nasa.gov/about_mms.html (visited on 06/23/2023).

[30] The European Space Agency (ESA). *GRACE (Gravity Recovery and Climate Experiment)*. 2023. URL: https://earth.esa.int/eogateway/missions/grace (visited on 06/24/2023).

[31] NASA Jet Propulsion Laboratory. *GRACE-FO Mission*. URL: https://gracefo.jpl.nasa.gov/mission/overview/ (visited on 07/04/2023).

[32] DARPA - Defense Advanced Research Projects Agency. *System F6 (Archived)*. 2023. URL: https://www.darpa.mil/program/system-f6 (visited on 06/24/2023).

[33] Remedy IT. *Aerospace: DARPA System F6 program*. URL: https://www.remedy.nl/portfolio/f6.html (visited on 07/04/2023).

[34] Dr. Jian Guo. *Disruptive Concepts*. URL: https://www.tudelft.nl/en/ae/organisation/departments/space-engineering/space-systems-engineering/research/distributed-space-systems/disruptive-concepts (visited on 07/04/2023).

[35] Zachary Robert Manchester. «Centimeter-scale spacecraft: Design, fabrication, and deployment». PhD thesis. Cornell University, Aug. 2015.

[36] Zachary Manchester. *Some Sprites Return Home After a Long Trip*. July 24, 2014. URL: https://www.kickstarter.com/projects/zacinaction/kicksat-your-personal-spacecraft-in-space/posts/925665 (visited on 06/26/2023).

[37] Lee Billings. *Reaching for the Stars, Breakthrough Sends Smallest-Ever Satellites into Orbit*. July 26, 2017. URL: https://www.scientificamerican.com/article/reaching-for-the-stars-breakthrough-sends-smallest-ever-satellites-into-orbit (visited on 06/26/2023).

[38] European Space Agency (ESA). *eoPortal - KickSat Nanosatellite Mission*. Apr. 9, 2014. URL: https://www.eoportal.org/satellite-missions/kicksat (visited on 06/25/2023).

[39] Zachary Manchester. *KickSat's Current Status*. May 3, 2014. URL: https://www.kickstarter.com/projects/zacinaction/kicksat-your-personal-spacecraft-in-space/posts/831509 (visited on 06/25/2023).

[40] The European Space Agency (ESA). *Venta-1 Nanosatellite*. June 27, 2017. URL: https://www.eoportal.org/satellite-missions/venta-1 (visited on 06/26/2023).

[41] Gunter Dirk Krebs. *Gunter's Space Page - Venta 1*. URL: https://space.skyrocket.de/doc_sdat/venta-1.htm (visited on 06/26/2023).

[42] The European Space Agency (ESA). *Max Valier Sat*. Apr. 27, 2017. URL: https://www.eoportal.org/satellite-missions/max-valier-sat (visited on 06/26/2023).

[43] Gunter Dirk Krebs. *Gunter's Space Page - Max Valier Sat*. URL: https://space.skyrocket.de/doc_sdat/max-valier-sat.htm (visited on 06/26/2023).

[44] Zachary Manchester. *KickSat Will Fly Again!* Feb. 6, 2015. URL: https://www.kickstarter.com/projects/zacinaction/kicksat-your-personal-spacecraft-in-space/posts/1087276 (visited on 06/26/2023).

[45] Gunter Dirk Krebs. *Gunter's Space Page - KickSat 1, 2*. URL: https://space.skyrocket.de/doc_sdat/kicksat-1.htm (visited on 06/26/2023).

[46] Frank Tavares. *What is KickSat-2?* June 3, 2019. URL: https://www.nasa.gov/ames/kicksat (visited on 06/26/2023).

[47] Derek Richardson. *NG-10 Cygnus Ends Post-ISS Mission After Deploying Satellites*. Feb. 25, 2019. URL: https://www.spaceflightinsider.com/missions/iss/ng-10-cygnus-ends-post-iss-mission-after-deploying-satellites (visited on 06/26/2023).

[48] Syl Kacapyr. *Cracker-sized satellites demonstrate new space tech*. June 3, 2019. URL: https://news.cornell.edu/stories/2019/06/cracker-sized-satellites-demonstrate-new-space-tech (visited on 06/26/2023).

[49] Bryan Klofas and Kyle Leveque. «A survey of CubeSat Communication Systems: 2009-2012». In: *10th Annual CubeSat Developers Workshop*. Barcelona, Spain, Apr. 2013.

[50] Muriel Noca et al. «Lessons Learned from the First Swiss Pico-Satellite: SwissCube». In: *AIAA/USU Conference on Small Satellites*. Logan, UT, 2009.

[51] David J. Barnhart, Tanya Vladimirova, and Martin N. Sweeting. «System-on-a-Chip Design of Self-Powered Wireless Sensor Nodes for Hostile Environments». In: *2007 IEEE Aerospace Conference*. 2007, pp. 1–12. DOI: 10.1109/AERO.2007.352640.

[52] Tracie R Perez and Kamesh Subbarao. «A Survey of Current FemtoSatellite Designs, Technologies, and Mission Concepts». In: *Journal of Small Satellites* 5.3 (2016), pp. 467–482.

[53] David J. Barnhart, Tanya Vladimirova, and Martin N. Sweeting. «Very-Small-Satellite Design for Distributed Space Missions». In: *Journal of Spacecraft and Rockets* 44.6 (2007), pp. 1294–1306. DOI: 10.2514/1.28678. URL: https://doi.org/10.2514/1.28678.

[54] David J. Barnhart et al. «A low-cost femtosatellite to enable distributed space missions». In: *Acta Astronautica* 64.11 (2009), pp. 1123–1143. ISSN: 0094-5765. DOI: https://doi.org/10.1016/j.actaastro.2009.01.025. URL: https://www.sciencedirect.com/science/article/pii/S0094576509000198.

[55] Robot Room. *Sandwich Robot PCB*. URL: https://www.robotroom.com/SandwichPCB.html (visited on 07/04/2023).

[56] Fred Y. Hadaegh, Soon-Jo Chung, and Harish M. Manohara. «On Development of 100-Gram-Class Spacecraft for Swarm Applications». In: *IEEE Systems Journal* 10.2 (2016), pp. 673–684. DOI: 10.1109/JSYST.2014.2327972.

[57] Andreas C Fischer et al. «Integrating mems and ics». In: *Microsystems & Nanoengineering* 1.1 (2015), pp. 1–16. DOI: 10.1038/micronano.2015.5.

[58] California NASA Ames Research Center Moffett Field. *State-of-the-Art - Small Spacecraft Technology*. Feb. 2023.

[59] Sven Ruhle. «Tabulated values of the Shockley-Queisser limit for single junction solar cells». In: *Solar Energy* 130 (2016), pp. 139–147. ISSN: 0038-092X. DOI: https://doi.org/10.1016/j.solener.2016.02.015.

[60] M. A. Green. *Third Generation Photovoltaics: Advanced Solar Energy Conversion*. New York, NY: Springer Berlin, Heidelberg, Sept. 5, 2006.

[61] Richard R. King. *Raising the Efficiency Ceiling in Multijunction Solar Cells*. Presentation. Stanford Photonics Research Center Symposium, Sept. 14, 2009.

[62] Eaton Electronics Division. *The major differences between supercapacitors and batteries*. Tech. rep. 2022.

[63] The European Space Agency (ESA). *Onboard Computers and Data Handling*. URL: https://www.esa.int/Enabling_Support/Space_Engineering_Technology/Onboard_Computers_and_Data_Handling/Onboard_Computers_and_Data_Handling (visited on 07/04/2023).

[64] James Richard Wertz and Wiley J Larson. *Space Mission Analysis and Design*. Springer Dordrecht, 1991.

[65] Honglong Chang et al. «Design and Simulation of a MEMS Control Moment Gyroscope for the Sub-Kilogram Spacecraft». In: *Sensors* 10.4 (2010), pp. 4130–4144. ISSN: 1424-8220. DOI: 10.3390/s100404130. URL: https://www.mdpi.com/1424-8220/10/4/4130.

[66] Mark Post et al. «Study for femto satellites using micro Control Moment Gyroscope». In: *2016 IEEE Aerospace Conference*. 2016, pp. 1–8. DOI: 10.1109/AERO.2016.7500721.

[67] T.W. Krygowski et al. «A low-voltage rotary actuator fabricated using a five-level polysilicon surface micromachining technology». In: *International Electron Devices Meeting*. 1999, pp. 697–700. DOI: 10.1109/IEDM.1999.824247.

[68] MEMS and Nanotechnology Exchange (MNX). *MNX Gallery*. URL: https://www.mems-exchange.org/gallery (visited on 07/04/2023).

[69] Science Sandia National Laboratories Microsystems Engineering and Applications (MESA). *MEMS Video & Image Gallery*. URL: https://www.sandia.gov/mesa/mems-video-image-gallery (visited on 07/04/2023).

[70] Ernest J. Garcia and Jeffry J. Sniegowski. «Surface micromachined microengine». In: *Sensors and Actuators A: Physical* 48.3 (1995), pp. 203–214. ISSN: 0924-4247. DOI: https://doi.org/10.1016/0924-4247(95)00999-X.

[71] Dillon O'Reilly, Georg Herdrich, and Darren F. Kavanagh. «Electric Propulsion Methods for Small Satellites: A Review». In: *Aerospace* 8.1 (2021). ISSN: 2226-4310. DOI: 10.3390/aerospace8010022. URL: https://www.mdpi.com/2226-4310/8/1/22.

[72] David Krejci et al. «Emission Characteristics of Passively Fed Electrospray Microthrusters with Propellant Reservoirs». In: *Journal of Spacecraft and Rockets* 54.2 (2017), pp. 447–458. DOI: 10.2514/1.A33531. URL: https://doi.org/10.2514/1.A33531.

[73] Daniel Bock and Martin Tajmar. «Highly miniaturized FEEP propulsion system (NanoFEEP) for attitude and orbit control of CubeSats». In: *Acta Astronautica* 144 (2018), pp. 422–428. ISSN: 0094-5765. DOI: https://doi.org/10.1016/j.actaastro.2018.01.012.

[74] European Space Agency (ESA). *UWE-4 (University Würzburg Experimental satellite-4)*. URL: https://www.eoportal.org/satellite-missions/uwe-4 (visited on 07/04/2023).

[75] Alexander Kramer, Philip Bangert, and Klaus Schilling. «UWE-4: First Electric Propulsion on a 1U CubeSat-In-Orbit Experiments and Characterization». In: *Aerospace* 7.7 (2020). ISSN: 2226-4310. DOI: 10.3390/aerospace7070098. URL: https://www.mdpi.com/2226-4310/7/7/98.

[76] Mengu Cho, Masui Hirokazu, and Filippo Graziani. «Introduction to lean satellite and ISO standard for lean satellite». In: *2015 7th International Conference on Recent Advances in Space Technologies (RAST)*. 2015, pp. 789–792. DOI: 10.1109/RAST.2015.7208447.

[77] Brenda Dingwall et al. «Bringing Space to the Classroom Through STEM Education Providing Extreme Low Earth Orbit Missions Using Thinsats». In: Aug. 2017.

[78] Northrop Grumman. *ThinSat Program Files*. URL: https://news.northropgrumman.com/multimedia/photo/Space/thinsat-program (visited on 07/04/2023).

[79] Shuanglong Xie et al. «Wireless Sensor Network for Satellite Applications: A Survey and Case Study». In: *Unmanned Systems* 02.03 (2014), pp. 261–277. DOI: 10.1142/S2301385014400056.

[80] Arducam. *OV2640 - Specs, Datasheet, Cameras, Features, Alternatives*. URL: https://www.arducam.com/ov2640 (visited on 07/04/2023).

[81] OMNIVISION. *The World's Smallest Commercially Available Image Sensor with Industry-Leading Resolution and Image Quality for Medical Applications*. URL: https://www.ovt.com/products/ov6948 (visited on 07/04/2023).

[82] OMNIVISION. *Miniature Camera Module Provides High-Quality Imaging for Disposable Medical Guidewires, Catheters and Endoscopes*. URL: https://www.ovt.com/products/ovm6948 (visited on 07/04/2023).

[83] OMNIVISION. *CameraCubeChip*. URL: https://www.ovt.com/technologies/cameracubechip (visited on 07/04/2023).

[84] ISS Research. *ThinSats Release*. URL: https://twitter.com/ISS_Research/status/1363175620482596864 (visited on 07/04/2023).